# Satellite-retrieval and modeling

# of glacier mass balance

# Satellietwaarneming en modeleren

# van de massabalans van gletsjers

(met een samenvatting in het Nederlands)

Proefschrift ter verkrijging van de graad van doctor aan de Universiteit Utrecht op gezag van de Rector magnificus, Prof. Dr. W. H. Gispen, ingevolge het besluit van het College voor Promoties in het openbaar te verdedigen op maandag 7 oktober 2002 des ochtends te 10:30 uur.

door

**Martijn Sybren de Ruyter de Wildt**

geboren op 7 september 1971, te Leiderdorp

Promotor: Prof. Dr. J. Oerlemans
Instituut voor Marien en Atmosferisch Onderzoek
Faculteit Natuur- en Sterrenkunde, Universiteit Utrecht
Princetonplein 5
3584 CC Utrecht
The Netherlands

Dit proefschrift werd mogelijk gemaakt met financiële steun van de Stichting Ruimte Onderzoek Nederland (projectnr. EO-030).

# Contents

# Dankwoord

Al als kind vond ik gletsjers en ijstijden interessant. Dat begon toen ik in mijn jeugd in musea op afdelingen rondliep waar landschapsvormen, onze verre voorouders en reeds lang uitgestorven fauna in hun perspectief werden gezet. Na mijn studie geofysica in Utrecht wilde ik me graag met klimaat en/of meteorologie gaan bezighouden, en na enige omzwervingen werd ik gewezen op een vacature voor een promotieonderzoek waarin deze twee onderwerpen (ijs en klimaat) samengingen (bedankt Abir en Jeroen!). Niet veel later zat ik aan de sollicitatietafel met Hans Oerlemans en dankzij hem kon ik aan het onderzoek beginnen. Tijdens mijn onderzoek heb ik veel gehad aan zijn originele ideeën en kennis van glacio-meteorologische processen. Hij was niet terughoudend in het geven van toestemming voor het bezoeken van conferenties, zomerscholen en gletsjers. Ik vond het erg leuk om veel mensen uit andere landen te ontmoeten en mij regelmatig op glad ijs te begeven. De vraag van Hans tijdens mijn sollicitatiegesprek: “Kan je skiën?”, bleek niet geheel overbodig!

Verder ben ik veel dank verschuldigd aan Wouter Greuell, die mij veel heeft geleerd over het bewerken van satellietbeelden en met wie ik veldwerk op de Morteratschgletscher in Zwitserland heb gedaan. Het vele uren achter elkaar op een gletsjer zitten, steeds een half uur wachtend tot de volgende meting gedaan kan worden, geeft je tijd voor bezinning. Sindsdien weet ik dat het graven van afwateringskanaaltjes op smeltende gletsjers een nogal zinloze bezigheid is. Ook mijn kamergenoot Michiel van den Broeke heeft mij veel geholpen door het beantwoorden van vragen en het aandragen van ideeën. Jan de Wolde heeft me geholpen met de data van het Vatnajökull-experiment, en dank zij hem ben ik nog een tweede keer voor mijn werk naar IJsland gegaan. Dankbaar heb ik gebruik gemaakt van de satellietbeelden en de bijbehorende programmatuur die Carleen Reijmer vóór mij al besteld en geschreven had. Alle bovengenoemde personen en alle overige leden van de IJs&Klimaat-groep (Dirk van As, Richard Bintanja, Bruce Denby, Michiel Helsen, Elise Hendriks, Coen Hofsteder, Karsten Kaspers, Lisette Klok, Nicole van Lipzig, Andrew Mackintosh, Martijn Thomassen, Carina van der Veen, Roderik van der Wal en Dan Zwartz) wil ik hartelijk danken voor het becommentariëren van delen van mijn proefschrift. Dat geldt natuurlijk ook voor Angelina Souren van Armadillo Research Services die de hoofdstukken 4 en 5 van mijn *stonecoal english* ontdaan heeft. Ook wil ik Paul Smeets van de VU in Amsterdam bedanken voor het opsturen van de scheefstanden van de Amsterdamse weerstations op Vatnajökull.

Met veel plezier denk ik terug aan alle lunches en vrijdagmiddagborrels met iedereen van het IMAU in het algemeen en van IJs&Klimaat in het bijzonder. Ik hoop alle regelmatige Jan Primus bezoekers ook in de toekomst nog af en toe aldaar te zullen treffen. De laatste twee jaar heb ik tijdens de lunchpauze op dinsdag gezongen bij het koor Voces Intimae. Dat was steeds een welkome (culturele) afwisseling op mijn werk waarvoor ik het hele koor en vooral de dirigent Arnoud Heerings wil bedanken. Zijn repetoirkeuze sprak me erg aan. Als iemand van het IMAU ook graag eens zijn stem wil verheffen, moet hij of zij maar contact opnemen met Yvonne Wouda.

Tot slot wil ik hier mijn ouders en mijn zus bedanken, die mij altijd gesteund hebben en interesse hebben getoond in mijn werk. Het was een toevallige samenloop van omstandigheden dat ik, kort voordat ik bij het IMAU solliciteerde, met mijn vader een rondreis door IJsland maakte. Je zou het een soort onvoorbereid voorbereidend veldwerk kunnen noemen! En als laatste noem ik Lieke, aan wie ik veel te danken heb en met wie ik een nu nog onzekere maar ongetwijfeld fantastische toekomst tegemoet ga.

# Acknowledgements

This thesis could not have been written without the help and advice of several people. I am much obliged to Helgi Björnsson and Oddur Sigurdsson for providing mass balance data. I would like to thank all the people involved in the 1996 Vatnajökull experiment, and especially Friedl Obleitner and Finnur Palsson for providing information about the data. I also thank Vedurstofa Íslands (especially Trausti Jónsson) for supplying meteorological and climatological data. Andrew Mackintosh also helped with some of the meteorological data. I am very grateful to Andrew Brooks and Neil Lonie from the Satellite Receiving Station in Dundee for their technical support, selection of AVHRR images, and patience when I failed to download the images properly. Furthermore, I want to thank Helmut Rott and, once more, Oddur Sigurdsson for useful comments upon chapter 4 and several anonymous reviewers for comments upon chapter 2, 3 and 4. Chapter 5 could not have been written without the kind supply of ERS images by ESA.

# Samenvatting


### Klimaatsverandering en gletsjers

Ongeveer 77% van de zoetwatervoorraad op aarde, overeenkomend met 71 m zeespiegelverandering, is als landijs opgeslagen op het aardoppervlak. De Antarctische ijskap neemt 90% hiervan voor zijn rekening, de Groenlandse ijskap bijna 10%, terwijl de rest (± 0.5%) uit kleine ijskappen en gletsjers bestaat. Nog niet zo lang geleden, tijdens de laatste ijstijd die ongeveer 12.000 jaar geleden eindigde, was er veel meer landijs aanwezig: de zeespiegel lag toen zo'n 120 m lager dan nu. Deze ijstijd eindigde plotseling en de zeespiegel steeg zeer sterk in een paar duizend jaar. Het einde van de laatste ijstijd markeerde het begin van een nieuwe geologisch tijdperk, dat we nu het Holoceen noemen en nog steeds voortduurt. Tijdens het Holoceen is het klimaat op aarde relatief stabiel gebleven met slechts kleine schommelingen. Één van deze schommelingen was de zogenaamde "kleine ijstijd", die ruwweg van de 15$^{e}$ tot het eind van de 19$^{e}$ eeuw duurde en temperaturen kende die gemiddeld 0,5 tot 1°C lager waren dan tegenwoordig. Tijdens deze periode breidden gletsjers over de hele wereld zich uit en rond 1850 hadden velen hun grootste uitbreiding sinds het einde van de laatste ijstijd bereikt of geëvenaard. Hierna begon een terugtrekking die zich tijdens de 20$^{e}$ eeuw versnelde en op het ogenblik zijn veel gletsjers net zo klein als tijdens de warmste fasen van het Holoceen. In de Alpen is het vergletsjerde oppervlak 30 tot 40% kleiner geworden en is het ijsvolume gehalveerd. In de afgelopen 150 jaar zijn veel gletsjers enkele honderden meters tot enkele kilometers korter geworden. Een goed voorbeeld hiervan is de Morteratschgletscher in Zwitserland (afbeelding 1.1), die zich sinds 1870 2 km heeft teruggetrokken en nu zo'n 7 km lang is. De bedding van de grootste uitbreiding in 1850, duidelijk zichtbaar als kale rotsgrond, laat zien dat de gletsjer een aanzienlijk deel van zijn vroegere volume heeft verloren. Eerder werk heeft aangetoond dat de wereldwijde terugtrekking van gletsjers verklaard kan worden door een gemiddelde temperatuurstijging van 0,66°C per eeuw, waaruit blijkt dat gletsjers behoorlijk gevoelig zijn voor klimaatsveranderingen. Merk echter op dat de grote ijskappen van Antarctica en Groenland veel stabieler zijn en veel langzamer op klimaatsveranderingen reageren.

De grote gevoeligheid voor klimaatsverandering betekent dat gletsjerfluctuaties in het verleden ons iets kunnen vertellen over het toenmalige klimaat, en ook dat elke toekomstige klimaatsverandering gletsjers zal beïnvloeden en als zodanig gevolgen zal hebben voor de aarde en voor menselijke activiteiten. Ten eerste beïnvloeden veranderingen in de hoeveelheid landijs het zeeniveau, en de grote ijskappen van Antarctica en Groenland zijn van belang voor het regionale en zelfs het wereldwijde klimaat omdat hun lichte oppervlakken veel zonnestraling terug de ruimte in weerkaatsen. In veel bergachtige gebieden fungeren gletsjers als een buffer door water in de winter op te slaan en in de zomer los te laten. Ze zorgen zo voor een voortdurende stroom(smelt)water, die door boeren en waterkrachtcentrales gebruikt kan worden. Verder trekt de natuurlijke schoonheid van veel gletsjers toeristen aan die de plaatselijke economie stimuleren.

Om de bovengenoemde redenen is het belangrijk te weten wat de huidige staat van gletsjers is en hoe ze op klimaatsveranderingen reageren. Deze vragen kunnen beantwoord worden door ter plekke de lengte en de massabalans (de jaarlijkse verandering in volume) van gletsjers te meten en door gletsjers modelmatig te bestuderen. Helaas zijn directe waarnemingen slechts voor weinig gletsjers beschikbaar, en de meeste waarnemingen overspannen slechts enkele decennia. Dit is een gevolg van het grote aantal gletsjers en de afgelegen ligging en uitgestrektheid van vele hiervan. Er bestaan algemene modellen die de invloed van het klimaat op gletsjers beschrijven, maar voor betrouwbare resultaten moeten deze modellen gekalibreerd worden met ter plekke gemeten data, die slechts in beperkte mate beschikbaar zijn. Dit proefschrift behandeld daarom de volgende twee onderwerpen. De eerste is het opzetten van een gekalibreerd massabalansmodel dat gebruikt kan worden om directe waarnemingen te vervangen en om de gevoeligheid van de massabalans voor klimaatsveranderingen te bestuderen. Het tweede onderwerp is het meten van de massabalans op indirecte wijze, dus zonder enige metingen die ter plekke gedaan zijn. Voor beide doeleinden bestuderen we Vatnajökull, een relatief grote ijskap in IJsland (zie afbeelding 1.3). Voor deze ijskap zijn veel ter plekke gemeten data beschikbaar, wat het mogelijk maakt om een gekalibreerd massabalansmodel samen te stellen en om nieuwe methoden voor de indirecte bepaling van de massabalans te testen.

**Enkele begrippen m.b.t. het verband tussen het klimaat en gletsjers**

De processen die leiden tot de vorming en instandhouding van gletsjers staan weergegeven in afbeelding 1.2. Gletsjers ontstaan wanneer de sneeuw die in de winter valt, niet geheel wegsmelt in de zomer. In dat geval is de specifieke massa balans (B), gedefiniëerd als de jaarlijkse verandering in massa per vierkante meter, positief. B wordt gemeten aan het eind van de zomer en heeft als eenheid meter water equivalent (m w.e.). Sneeuw die de zomer overleeft wordt firn genoemd en heeft een hogere dichtheid en is minder wit dan sneeuw. Als B altijd positief is zal het firndek ieder jaar aangroeien en uiteindelijk onder zijn eigen gewicht tot ijs samengedrukt worden. IJs is een plastische stof en zal onder invloed van de zwaartekracht hellingaf stromen. Op kleinere hoogte is het warmer, waardoor meer afsmelting en minder sneeuwval optreedt. Alle sneeuw die er in de winter valt zal er tijdens de zomer wegsmelten, zodat tijdens een deel van de zomer ijs aan het oppervlak ligt en wegsmelt. In dit geval is B negatief. De grens tussen de gebieden met positieve en negatieve B wordt de evenwichtslijn genoemd. De evenwichtslijn is gelijk aan de sneeuwlijn aan het eind van het smeltseizoen, en ligt dus op de hoogte waar alle wintersneeuw aan het eind van het smeltseizoen precies is weggesmolten.

De hoeveelheid sneeuwval hangt af van de hoeveelheid neerslag en van de temperatuur, maar afsmelting laat zich niet zo eenvoudig beschrijven. Als de oppervlaktetemperatuur onder het vriespunt ligt, zal elke energiestroom van de atmosfeer naar het oppervlak het oppervlak verwarmen. Omdat de temperatuur van sneeuw en ijs het vriespunt niet kan overschrijden, zal elke verdere energietoevoer tot afsmelting leiden. De netto energiestroom bestaat uit verschillende componenten: kortgolvige zonnestraling, langgolvige atmosferische straling en turbulente overdracht van warmte. De zonnestraling wordt

gedeeltelijk weerkaatst en gedeeltelijk geabsorbeerd. De verhouding tussen weerkaatste straling en invallende straling wordt de albedo genoemd. Lichte oppervlakken (bv. sneeuw) hebben dus een hoge albedo en weerkaatsten veel van de zonnestraling, en donkere oppervlakken (bv. vies gletsjerijs) hebben een lage albedo en absorberen veel zonnestraling. De netto kortgolvige energiestroom, en daarmee de albedo, is een belangrijk onderdeel van de energiebalans van het oppervlak. De invallende langgolvige straling, waarvan de intensiteit afhangt van de temperatuur van de atmosfeer, wordt geheel door het oppervlak opgenomen. Het oppervlak zelf zendt ook langgolvige straling uit. De turbulente overdracht van voelbare (of latente) warmte treedt op als er een verschil in temperatuur (of vochtigheid) is tussen het oppervlak en de atmosfeer vlak boven het oppervlak. Er treedt dan een uitwisseling van energie op die afhangt van het verschil in temperatuur (of vochtigheid) en van de snelheid waarmee lucht in contact met het oppervlak gebracht wordt (dus van de windsnelheid vlak boven het oppervlak). De turbulente uitwisseling van warmte koelt de lucht vlak boven het oppervlak af, en deze relatief zware lucht zal hellingaf gaan stromen. Boven smeltende gletsjeroppervlakken is daarom vaak aan hellingafwaartse oppervlaktewind aanwezig (de zogenaamde katabatische wind), die opmerkelijk constant in sterkte en richting is. De katabatische oppervlaktelaag met lage temperaturen en hellingafwaartse winden bepaalt in sterke mate de uitwisseling van energie tussen de vrije atmosfeer en de gletsjer.

**Resultaten en conclusies**

In hoofdstuk 2 wordt een massabalansmodel van Vatnajökull gepresenteerd dat gebaseerd is op het berekenen van de energiebalans van het oppervlak. Ter plekke gemeten data worden gebruikt om de parametrisaties voor de invallende zonnestraling, de invallende atmosferische straling en de albedo van sneeuw te kalibreren. Om de ruimtelijke verdeling van de albedo van ijs te bepalen gebruiken we satellietbeelden. Uit de data blijkt dat de invallende atmosferische straling het best beschreven kan worden als functie van meteorologische variabelen in de vrije atmosfeer net boven de katabatische laag. Op meethoogte (2 m boven het oppervlak) in de katabatische laag zijn temperatuur en vochtigheid anders dan in de vrije atmosfeer, terwijl de katabatische laag boven Vatnajökull vrij dun is en de meeste langgolvige straling van de bovenliggende vrije atmosfeer afkomstig is. De verhouding tussen veranderingen in de 2 m temperatuur en veranderingen in de temperatuur van de vrije atmosfeer is kleiner dan 1, wat gevolgen heeft voor de berekening van de turbulente energieoverdracht. Vaak, en ook in dit onderzoek, wordt de zogenaamde Bulkmethode gebruikt, waarvoor de 2 m temperatuur nodig is. Dit betekent dat de 2 m temperatuur dus expliciet berekend worden, omdat anders de gevoeligheid van de massabalans voor temperatuursveranderingen overschat zou worden. Hier gebruiken we een empirisch verband tussen de 2 m temperatuur en de temperatuur in de vrije atmosfeer. De hoeveelheid neerslag op Vatnajökull is nauwelijks bekend, en daarom gebruiken we deze variabele om het massabalansmodel te kalibreren zodat de massabalansmetingen gereproduceerd worden. Als we het model aandrijven met data van een permanent weerstation dat buiten de invloed van de ijskap staat, reproduceert het model de massa-

balansmetingen redelijk goed. Boven de ijskap zijn grote horizontale gradiënten in neerslag, wat zijn invloed heeft op de gevoeligheid van de massabalans voor temperatuursveranderingen: in het algemeen neemt deze gevoeligheid bij hogere neerslag toe. Lokale klimatologische omstandigheden bepalen de massabalans en zijn gevoeligheid dus in hoge mate. Voor een temperatuurstijging van 1°C en een gelijktijdige neerslagtoename van 5,3%, neemt de specifieke massabalans, geïntegreerd over het oppervlak (de gemiddelde specifieke massabalans, $B_m$) af met 0.56 m w.e.

We onderzoeken de klimaatgevoeligheid van Vatnajökull verder in hoofdstuk 3 door met het fysische model uit hoofdstuk 2 de gevoeligheid van $B_m$ voor maandelijkse variaties in temperatuur en neerslag te bepalen. Het IJslandse klimaat is voornamelijk maritiem (hoge neerslag), hoewel polaire luchtmassa's het gebied vaak beïnvloeden. Als gevolg hiervan is de temperatuursgevoeligheid van de massabalans hoog in de zomer (door de hoge neerslag) en laag in de winter (door de lage temperaturen). Aan de andere kant is de neerslagsgevoeligheid juist laag in de zomer en hoog in de winter. We kunnen de maandelijkse temperatuurs- en neerslagsgevoeligheden gebruiken als een vereenvoudigd massabalansmodel door ze te vermenigvuldigen met maandelijkse afwijkingen in respectievelijk temperatuur en neerslag. Met dit vereenvoudigde model reconstrueren we de massabalans van Vatnajökull sinds 1825, daarbij gebruik makend van maandelijks gemiddelde waarden van temperatuur en neerslag. Hieruit blijkt dat veranderingen in temperatuur en neerslag, zoals die op IJsland voorkomen, beide belangrijk zijn voor de massabalans. Een andere methode om de massabalans in het verleden te reconstrueren is de zogenaamde inverse methode, waarbij berekend wordt hoe groot de massabalansverandering moet zijn geweest om een gemeten lengteverandering te kunnen veroorzaken. Wanneer we voor twee IJslandse gletsjers een massabalansreeks bepalen met het vereenvoudigde massabalansmodel (de voorwaartse methode), blijken deze goed overeen te komen met de resultaten van de inverse methode. Het feit dat de resultaten van twee onafhankelijke methoden goed overeenkomen, geeft beide methoden een hoge betrouwbaarheid. Voor het zuiden van Vatnajökull vinden we dat de gletsjerlengtes na 1900 goed verklaard worden door temperatuurschommelingen alleen, terwijl voor een gletsjer elders in IJsland (Sólheimajökull) veranderingen in neerslag óók belangrijk waren.

In hoofdstuk 4 onderzoeken we of met een satelliet verkregen albedobeelden gebruikt kunnen worden om de massabalans van Vatnajökull te bepalen. Een al eerder gebruikte methode om dit te doen is door met satellietbeelden de hoogte van de evenwichtslijn te bepalen: voor veel gletsjers is deze hoogte rechtevenredig aan $B_m$. Het blijkt echter dat evenwichtslijn van Vatnajökull, te bepalen aan de hand van de massabalansmetingen, niet zichtbaar is op de satellietbeelden als hij zich hoger bevindt dan in het voorafgaande jaar. In dat geval is er namelijk firn aan de oppervlakte aanwezig, en firn heeft vrijwel dezelfde eigenschappen als sneeuw van een paar maanden oud. Bovendien wordt de bepaling van de evenwichtslijn met satellietbeelden verder bemoeilijkt door bewolking en door een soms zeer geleidelijke overgang tussen ijs en sneeuw. We gebruiken daarom een nieuwe methode waarbij we gemiddelde albedo over de gehele ijskap tijdens het hele smeltseizoen bepaald wordt. Dit betekent dat alle beschikbare informatie over het oppervlak gebruikt wordt, en niet alleen de positie van één lijn op één bepaalde dag. Uit de gemiddelde albedo bepalen we de gemiddelde netto potentiële kortgolvige straling, welke van invloed is op de hoeveelheid afsmelting. De gemiddelde netto potentiële

kortgolvige straling hangt ook af van de hoeveelheid winterneerslag: als er veel sneeuw valt duurt het in de zomer langer voordat er ijs, met een lagere albedo, aan de oppervlakte komt. Het blijkt dat de netto potentiële kortgolvige straling, gemiddeld over het oppervlak en over de zomer, rechtevenredig is aan $B_m$. Voor Vatnajökull kan dit lineaire verband worden gebruikt om $B_m$ met een onzekerheid van 0,5 tot 0,8 m w.e. te bepalen.

In hoofdstuk 5 analyseren we een ander soort satellietbeelden, namelijk radarbeelden (Synthetic Aperture Radar oftewel SAR). We vergelijken SAR-beelden van Vatnajökull met massabalansmetingen, modelresultaten uit hoofdstuk 2 en albedobeelden uit hoofdstuk 4. Ten eerste doen we dit om uit te zoeken welke oppervlaktestructuren van gletsjers zichtbaar zijn op SAR-beelden. Een tweede doel is om te bepalen of SAR-beelden gebruikt kunnen worden om de massabalans te achterhalen. Het blijkt dat SAR-beelden en albedobeelden die in de zomer genomen zijn beide de firnlijn (de grens tussen firn en ijs) als een duidelijke grens vastleggen. Op geen van beide beelden nemen we echter de grens tussen sneeuw en firn waar. De evenwichtslijn is daarom niet waar te nemen als hij boven de firnlijn ligt en voor slecht één van negen jaren is hij te identificeren. Anders dan de albedo, vertoont het gemiddelde SAR-signaal geen verband met $B_m$. Voor sommige delen van Vatnajökull vinden we echter wel een verband tussen $B_m$ en de gemiddelde hoogte van de firnlijn tijdens de zomer. Voor andere delen van Vatnajökull is zo'n verband niet vast te stellen, en voor deze delen hebben SAR-beelden dan ook geen nut wat betreft de bepaling van de massabalans.

In hoofdstuk 6 vergelijken we de resultaten uit de hoofdstukken 2, 4 en 5 met elkaar en met directe metingen van de gemiddelde specifieke massabalans. De verschillende resultaten komen vrij goed met elkaar overeen, behalve voor één jaar. Voor dit jaar zijn er weinig satellietbeelden beschikbaar, terwijl het er bovendien op lijkt dat het massabalansmodel voor dit jaar de hoeveelheid neerslag verkeerd berekent. Tot slot beschouwen we de toekomst van het met de satelliet waarnemen van de massabalans in hoofdstuk 7. Nieuwe satellieteninstrumenten, met name altimeters, bieden samen met de methode uit hoofdstuk 4 mogelijkheden om op verschillende, onafhankelijke manieren de massabalans te schatten.

# 1 Introduction

## 1.1 Climate change and glaciers

Land ice contains approximately 77% of the world's fresh water, corresponding to 71 m of global sea-level. The Antarctic ice sheet accounts for 90% of this, the Greenland ice sheet nearly 10%, while the remainder (± 0.5%) is held by much smaller ice caps and glaciers. Not so long ago, during the last ice, much more land ice was present: the sea-level was about 120 m lower than it is today. This ice age ended between 18,000 and 12,000 years ago and sea-level rose dramatically within several thousands of years. The end of the last ice age marked the beginning of a new geological era, which we now call the Holocene and lasts until today. Throughout the Holocene the earth's climate has been relatively stable with only small fluctuations. One of these fluctuations was the so-called "little ice age", which roughly lasted from the 15$^{th}$ till the end of the 19$^{th}$ century and during which global mean temperatures were, on average, 0.5 to 1°C lower than today. During this period many glaciers world-wide advanced and around 1850, many had reached or equaled their largest extension since the end of the last ice age. After that time a retreat set in which accelerated in the 20$^{th}$ century, and nowadays many glaciers are as small as during the warmest phases of the Holocene. In the Alps the glacierized area has decreased with 30 to 40%, while the ice volume decreased with 50%. Typical decreases in length of glaciers vary from a few hundred meters to several kilometers over the last 150 years (e.g. Grove, 1988; Oerlemans, 2001). A good example of this is the Morteratschgletscher in Switzerland (figure 1.1), which receded 2 kilometer since 1870 and is now about 7 km long. Its bed from the 1850 high-stand, still clearly recognizable as bare soil, shows that the glacier has lost a significant part of its former volume. According to Oerlemans (1994) the world-wide glacier retreat can be explained by a global mean temperature increase of 0.66°C per century, which shows that glaciers are quite sensitive to changes in climate. Note, however, that the ice sheets of Antarctica and Greenland are much more stable and react much slower to climate changes.

The large sensitivity to climatic change means that glacier fluctuations in the past can tell us something about the past climate, and also that any future climatic change will affect glaciers and as such will have consequences for the earth-system and human activities. First of all, changes in the volume of land ice affect sea-level, and the large ice sheets of Antarctica and Greenland are important for regional and even global climate because their bright surfaces reflect much solar radiation back into space. In many mountainous areas, glaciers act as a buffer by storing water in the winter and releasing it in the summer. They thus provide a continuous flow of melt water, which can be used by farmers and hydro-power plants. Also, the natural beauty of glaciers attracts many tourists, which supports local economies.

Sea-level is observed to have risen 10 to 20 cm during the 20$^{th}$ century (Houghton et al., 2001). This rise has several causes, which are tabulated in table 1.1. Global tem-

*Figure 1.1. The Morteratschgletscher in south-eastern Switzerland. Photograph taken by the author from a helicopter in July 1998.*

perature influences sea-level mainly through thermal expansion of the water in the oceans and melting of glaciers and ice caps. Though much smaller in volume than the large ice sheets, the small ice caps and glaciers contribute significantly to sea-level on a century time-scale, because they are much more sensitive to climate changes (e.g. Meier, 1984). Antarctica is so cold that no melt takes place, even when it gets warmer. On the other hand, precipitation generally increases in a warmer climate, thus leading to an increase in volume of the Antarctic ice sheet. On Greenland both effects (increased melt and increased precipitation) play a role, resulting in a small positive contribution to global sea-level. Large ice sheets respond very slowly to changes in climate, which is why the ice sheets of Antarctica and Greenland still change due to climatic changes thousands of years ago. This also gave a positive contribution to sea-level rise during the past 100 years. Finally, the terrestrial storage of water (e.g. ground-water, water in lakes) might have changed, but this contribution to sea-level has a large uncertainty. The sum of all contributions is low compared to, but not incompatible with, the observed rise.

For the reasons mentioned above, it is important to know what the current status of glaciers is and how they react to external climatic changes. These questions can be answered by *in situ* observations of length and mass balance (the annual change in volume) of glaciers and by modeling studies. However, observations are only available for a small number of glaciers world wide, and most observations do not span more than a few decades. This is obviously due to the vast number of glaciers and the remoteness and extensiveness of many of these. There are general models that describe the influence of climate upon glaciers (e.g. Oerlemans, 1992), but for accurate results these models need

to be calibrated with *in situ* measured data, which are poorly available. This thesis basically addresses two issues. The first is the construction of a calibrated mass balance model, which can be used to replace direct observations and to study the sensitivity of the mass balance to climate change. The second issue it that of observing the mass balance in an indirect way, so that it is not necessary to actually visit a glacier or ice cap. The object of interest is Vatnajökull, a large ice cap in Iceland. For this ice cap many *in situ* measured data are available (Björnsson et al., 1998a; Oerlemans et al., 1999), which makes it possible to construct a calibrated mass balance model and to use the ice cap as a test case for alternative ways of estimating the mass balance.

| Source | change in sea-level (cm) |
|---|---|
| Thermal expansion | 3 - 7 |
| Glaciers and ice caps | 2 - 4 |
| Antarctica | -2 - 0 |
| Greenland | 0 - 1 |
| Long-term adjustment of Antarctica and Greenland | 0 - 5 |
| Terrestrial storage (1910-1990) | -11 - 4 |

*Table 1.1. Estimated contributions of various sources to global sea-level rise during the 20$^{th}$ century. Data from Houghton et al., 2001.*

## 1.2 Some basic concepts of the relation between glaciers and climate

The processes that lead to the formation of glaciers and influence their extent are depicted in figure 1.2. Glaciers form when the snow that falls in the winter, does not entirely melt away in the summer. In such a case the specific mass balance (B), defined as the annual change in mass per square meter, is positive. B is given in meter water equivalent (m w.e.) and usually measured at the end of the summer. Snow that survives the summer is called firn, which has a higher density and is less bright than snow. When the specific mass balance is always positive, the firn pack will grow thicker each year and eventually be compressed into ice under its own weight. Ice is a plastic material and will flow down-slope under the influence of gravity. At lower elevations temperatures are higher, which increases the amount of melt and decreases the amount of snow fall. All snow that falls there in the winter will melt away in the summer, so that during a part of the summer ice is at the surface and melts away. Now, the specific mass balance is said to be negative. The boundary between the areas of positive and negative specific mass balance is called the equilibrium line. The equilibrium line equals the snow line at the end of the melting season, i.e. it lies at the altitude where all snow of the last winter has exactly melted away at the end of the melting season. A glacier is in balance with the climate when the specific mass balance, integrated over the surface area (the mean specific mass balance, $B_m$), equals zero. This is not necessarily always the case: glaciers adjust to a changed climate by changing their areal extent, for which they need some time.

The specific mass balance depends upon snow fall (accumulation) and melt

(ablation). The amount of snow fall only depends upon precipitation and temperature, but the process of ablation is much more complicated. When the surface temperature is below the freezing point, any energy flux from the atmosphere towards the surface is used for raising the surface temperature. The temperature of snow and ice cannot exceed the melting point and once this temperature is reached, any additional energy flux to the surface will be used for melting. The net energy flux is the sum of several different energy fluxes: those of shortwave radiation, longwave radiation and turbulent exchange of heat and moisture. The shortwave radiation that reaches the surface originates from the sun. Solar radiation has relatively short wave-lengths: mainly between 0.2 and 2 μm with a peak at 0.47 μm, corresponding to visible light and infra-red. The solar radiation that impinges upon the surface (also called the global radiation) is partly reflected and partly absorbed. The ratio of reflected radiation over incoming radiation is called the albedo. Thus, bright surfaces (e.g. snow) have a high albedo and reflect much of the global radiation, and dark surfaces (e.g. dirty glacier ice) have a low albedo and absorb much of the global radiation. The net shortwave radiation flux, and hence the albedo, is an important part of the energy balance.

Not only radiation from the sun reaches the earth's surface, but also radiation from the earth's atmosphere. Because the radiative temperature of the earth's atmosphere is much lower than that of the sun, this radiation has longer wave-lengths (peak at 9.9 μm) than the solar radiation. The incoming longwave radiation, the intensity of which depends upon the temperature of the atmosphere, is entirely absorbed by the surface. The glacier surface itself also emits longwave radiation. A third type of energy flux is the turbulent flux of sensible and latent heat. There is a flux of sensible heat whenever the temperature of the air just above the surface is different from the surface temperature. Then an exchange of energy takes place, which depends upon the temperature difference between air and

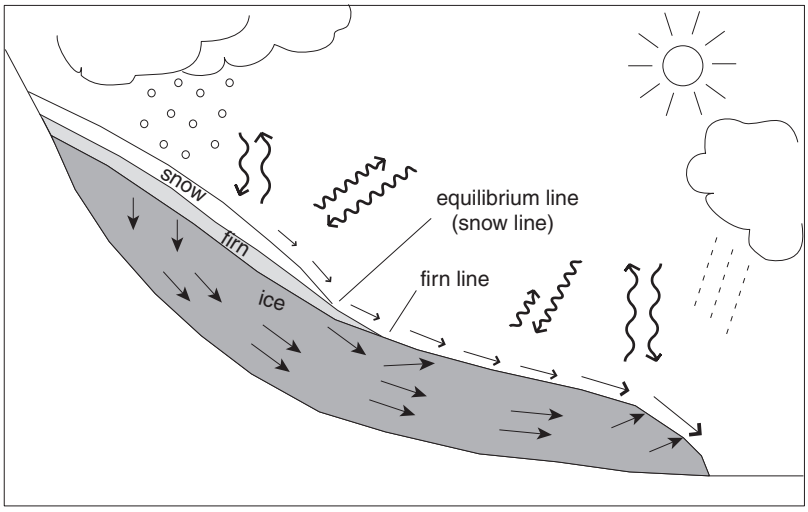


*Figure 1.2. Schematic representation of a glacier at the end of the melting season, displaying the main processes that lead to the formation and maintenance of a glacier.*

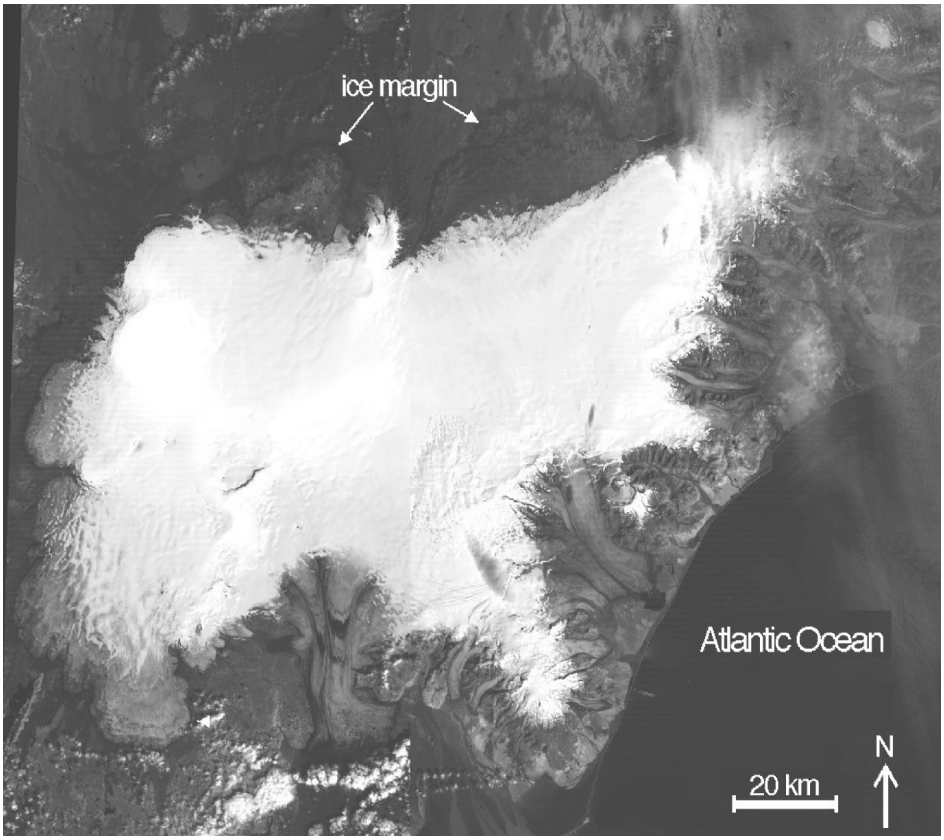


*Figure 1.3. Composite satellite image (Landsat Thematic Mapper, channel 4) of Vatnajökull. Over the north-east and over the south some clouds are visible. Two images, acquired on August 17th, 1995 and on August 19th, 1996 were used to make this composite. Courtesy of Carleen Reijmer.*

surface, and also upon the speed with which air is brought into contact with the surface (the wind speed just above the surface, that is). Latent heat is exchanged when water molecules condensate or sublimate on the glacier surface. The exchange of heat between atmosphere and glacier cools the air just above the surface, and this air will be denser than the surrounding air and flow down the glacier surface under the influence of gravity. Therefore, over melting glacier surfaces often a down-slope surface wind is present (the so-called katabatic wind) which is remarkably constant in strength and direction. The layer of cool air with persistent down-slope winds is called the katabatic surface layer and strongly influences the exchange of energy between free atmosphere and glacier.

The difference in albedo between snow and ice is clearly visible in the composite satellite image of Vatnajökull shown in figure 1.3. The accumulation area is covered with snow and forms the largest part of the ice cap. From the accumulation area many outlet glaciers and a number of large lobes flow down. In the south and south-east the glaciers almost reach the ocean. The outlet glaciers and lobes are largely ice-free, as the images

were taken in the second half of August. Some parts of the ablation areas are darker than others, which is caused by layers of volcanic ash. This so-called tephra is deposited on the ice cap every few decades by one of the near-by active volcanoes. It is transported down-slope to the ablation areas where it melts out and accumulates. Because of this, the ablation areas in the north are hardly discernable from the surrounding land.

## 1.3 Methods for estimating the mean specific mass balance

The mean specific mass balance of a glacier can be estimated with different methods, all of which have their advantages and disadvantages. Here we only discuss some methods which can be used to estimate the mean specific mass balance of ice caps and glaciers. For the ice sheets of Antarctica and Greenland additional methods are available, such as observations of the atmospheric moisture transport towards the ice sheets and atmospheric models that determine the state of the entire atmosphere over the ice sheet.

### *1.3.1 Direct observation*

Glacier mass balance can be directly measured by placing stakes in the snow or in the ice. After some time, the surface height changes due to melt (accumulation), which exposes (buries) a part of the stake. In the accumulation area, snow pit and ice core data can be used to measure the balance by identifying the annual layer. To measure the mean specific mass balance of the whole glacier, representative point measurements from all parts of the glacier are needed. These point measurements are interpolated over the glacier surface to obtain the mean specific mass balance, which inherently introduces uncertainty. Obviously, the accuracy of this method depends upon the number of stake readings.

### *1.3.2 Modeling*

When the meteorological conditions in the vicinity of a glacier are known, models that compute ablation and accumulation from meteorological variables can be used to compute the mass balance. These models can have different degrees of complexity. The most simple ones are merely empirical relations between the important meteorological variables (temperature and precipitation) and the mass balance (e.g. Lliboutry, 1974; Hoinkes and Steinacker, 1975; Günther and Widlewski, 1986). Slightly more complicated models are the so-called positive degree-day models, which calculate surface melt as a function of temperature (e.g. Braithwaite, 1985; Reeh, 1991; Jóhannesson, 1997). The most complex models are the physically based ones (e.g. Oerlemans, 1992; Van de Wal and Oerlemans, 1994). They require the most computing time, but with the current computational power of computers this hardly forms a problem.

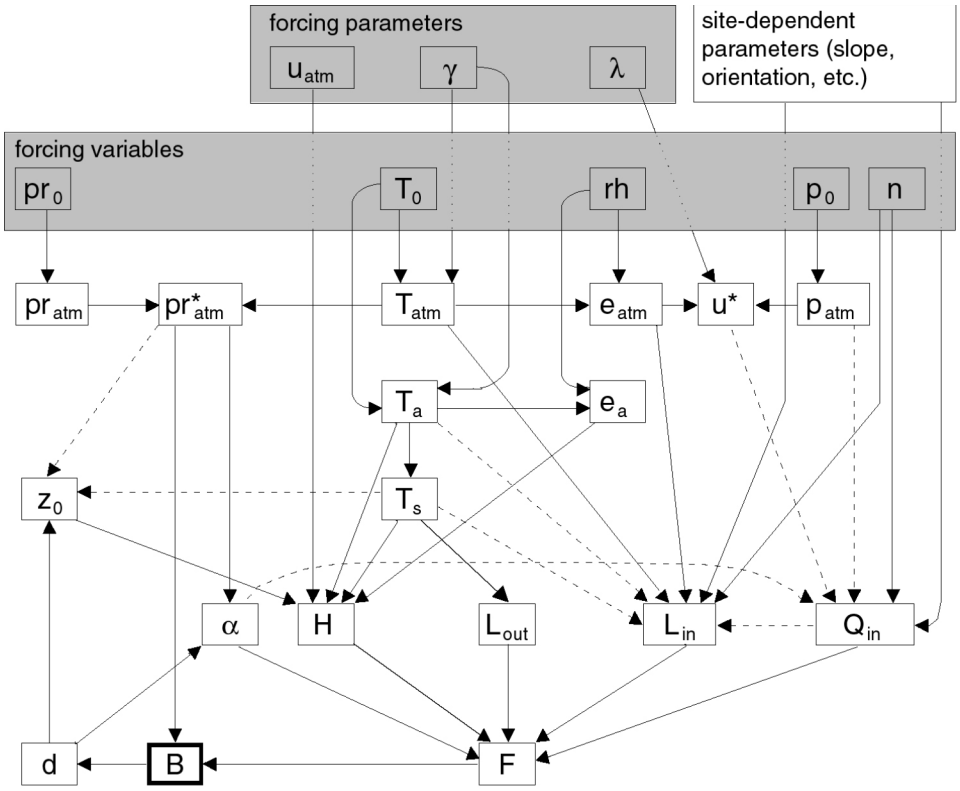


$\gamma$ : atmospheric lapse rate
$\alpha$ : surface albedo
B : mass balance
d : snow depth
rh : relative humidity at reference station
$e_a$ : vapour pressure at screen height
$e_{atm}$ : free atmospheric vapour pressure at altitude of evaluation site
F : total energy flux
H : turbulent fluxes
$L_{in}$ : incoming long wave radiation
$L_{out}$ : outgoing long wave radiation
n : cloudiness
$pr^*_{atm}$ : solid precipitation at location and altitude of evaluation site
$pr_0$ : precipitation at reference station
$pr_{atm}$ : precipitation at location and altitude of evaluation site
$p_0$ : pressure at reference station
$p_{atm}$ : pressure at altitude of evaluation site
$u^*$ : water content in a vertical air column
$Q_{in}$ : global radiation
$T_0$ : temperature at reference station
$T_a$ : 2-m temperature
$T_{atm}$ : free atmospheric temperature at altitude of evaluation site
$T_s$ : surface temperature
$u_{atm}$ : windspeed at altitude of evaluation site
$z_0$ : surface roughness length

*Figure 1.4. Attempt of the author to represent the mass balance model of chapter 2 in a flow diagram. Dashed lines represent weak relations.*

In all of these models uncertainty is introduced when meteorological point measurements from a site in the surroundings of the glacier are extrapolated to the glacier. This is mainly the case for precipitation, which strongly varies with altitude and location in mountainous regions, but can also affect temperature and cloudiness. It is therefore

inevitable that mass balance models need some kind of *in situ* calibration. For example, precipitation over the glacier can be obtained by comparing model results with mass balance observations. Furthermore, the transfer of energy from atmosphere to glacier surface can be quite complex (e.g. figure 1.4) and difficult to parameterize. Often empirical schemes are used that need to be calibrated, which enhances the need for *in situ* data.

### *1.3.3 Remote sensing*

Ice caps and glaciers often lie in remote areas that are difficult to access, and they can have vast surface areas. This makes it difficult and costly to collect *in situ* data at regular time intervals, be it for direct measurements of the mass balance or for meteorological measurements. Satellites have the ability to observe large areas of the earth at regular time intervals, without the need to actually go there, and are therefore interesting tools for studying glaciers. Satellite instruments remotely sense surface quantities: they measure electro-magnetic waves that have traveled through the atmosphere and originate from, or have been reflected at, the earth's surface. König et al. (2001a) give a good overview of the use of remote sensing in glaciology. Here we will only discuss the use of satellite instruments for measuring the mass balance. Table 1.2 displays the satellite instruments that are most often used in glaciology. These instruments have all been operated over the last one or two decades and provide data for enough years to make useful comparisons with mass balance records. Measurements of short wave-lengths (visible and infrared) can be used to retrieve the surface albedo. This is not only of importance for mass balance modeling, but also for identification of surface features like the firn line and the glacier margin. The Thematic Mapper (TM) on board of the Landsat satellites measures these wave-lengths and has a horizontal resolution of 30 m and a temporal resolution of 16 days. This makes it difficult to find cloud-free TM images of Iceland, where the skies are overcast most of the time. In this respect the Advanced Very High Resolution Radiometer (AVHRR) on board of the National Oceanic and Atmospheric Administration (NOAA) satellites is more appropriate. These satellites produce several images of Iceland per day, which makes it easy to capture the sparse cloud-free moments. The AVHRR has a much larger horizontal resolution than the TM (namely 1.1 km or larger), but for a relatively large ice cap like Vatnajökull

| Satellite and instrument | Horizontal resolution (m) | Temporal resolution over Iceland | band | Spectral region | Wave-lengths (μm) |
|---|---|---|---|---|---|
| Landsat TM | 30 | 16 days | 2 | visible (green) | 0.52 - 0.60 |
| | | | 4 | near-infrared | 0.76 – 0.90 |
| NOAA AVHRR | ≥ 1100 | < 1 day | 1 | visible | 0.58 – 0.68 |
| | | | 2 | near-infrared | 0.73 – 1.10 |
| ERS SAR | 30 | a few days | | microwave (C-band) | 55,600 |

*Table 1.2. Features of several satellite sensors that are often used in glaciological studies.*

this is not a problem. Microwaves have much larger wavelengths (a few mm to cm) than visible and infrared electromagnetic waves, and can therefore penetrate clouds and are not dependent upon day-light. There are two types of instruments that measure microwave intensity: active instruments and passive instruments. Synthetic Aperture Radar (SAR) is an active microwave instrument that sends out a signal, and shortly thereafter measures the backscatter from the earth's surface. SAR images from the European Remote sensing Satellites (ERS) are the most commonly used. Passive microwave sensors measure the microwaves that are naturally emitted by the earth's surface.

Østrem (1975) suggested that the often-found linear relation between $B_m$ and the equilibrium line (e.g. Østrem, 1975; Hagen and Liestøl, 1990) can be used to infer $B_m$, provided that the equilibrium line is visible on satellite images. This method depends upon the difference in reflective and backscattering properties between snow and ice (or firn) and has been applied with varying success (e.g. Rott and Markl, 1989; Demuth and Pietroniro, 1999; Hall et al., 2000; König et al., 2001b). Both albedo images and radar backscatter images have been used for this. Microwaves can also be used to estimate individual components of the mass balance. When no melt occurs and only accumulation takes place, the amount of accumulation may be estimated with microwave data (Zwally, 1977), but this method has not been often used. For reliable estimates, the amount of hoar-formation needs to be known (Abdalati and Steffen, 1998). The microwave signal is extremely sensitive to the amount of liquid water in the snow pack and can therefore also be used to map the extend, but not the amount, of surface melt (e.g. Steffen et al., 1993; Mote and Anderson, 1995). For temperate ice caps like Vatnajökull these two methods are of little use because the entire surface, including higher elevations, is melting during most of the summer.

### *1.3.4 Geodetic method*

The mean specific mass balance can also be estimated by comparing successive measurements of surface elevation. The difference in surface elevation, integrated over the glacier surface, then gives the mass change during the period between the two measurements. For this purpose the measurements must have a high precision, which can be achieved with photogrammetry and with airborne radar (or lidar) altimetry. Satellite altimetry also measures surface elevation, but current spaceborne altimeters are not precise enough to assess the mean specific mass balance of glaciers. This may change in the near future, when satellites are launched that carry high-precision altimeters.

## 1.4 Contents of this thesis

In each of the chapters 2 to 5 a different way of obtaining mass balance estimates of Vatnajökull is investigated. In chapter 6 the results from the previous chapters are com-

pared with each other. The contents and conclusions of these chapters are briefly presented in abstracts that precede each chapter. In chapter 2 we present a mass balance model for Vatnajökull that is based upon a calculation of the surface energy balance. *In situ* measured data are used to calibrate parameterizations for the albedo of snow, the global radiation, and the incoming longwave radiation. For the albedo of ice, we use satellite data in addition to the ground albedo measurements. A difference with other mass balance models is the distinction that is made between temperature in the free atmosphere and in the katabatic surface layer. Precipitation over the ice cap is largely unknown, and this variable is therefore used to tune the model to observed mass balance values. The model is used for reconstructing the mean specific mass balance over the last 35 years, using meteorological data from near-by weather stations, and for investigating the sensitivity of different parts of Vatnajökull to climatic changes. The climate sensitivity of Vatnajökull is further investigated in chapter 3 with a simplified mass balance model (Oerlemans and Reichert, 2000). This model is based upon the physical model of chapter 2, but only describes the mass balance in terms of monthly perturbations of temperature and precipitation. With this reduced model we also reconstruct the mass balance of Vatnajökull over the past 175 years, using monthly records of temperature and precipitation over this period. This reconstruction is compared with a mass balance reconstruction deducted from glacier length variations (Klok and Oerlemans, 2002).

In chapter 4 we investigate the usability of satellite albedo images for mass balance retrieval. First we investigate whether the equilibrium line of Vatnajökull can be detected by comparing albedo images with *in situ* mass balance measurements. Then we present a new method for satellite-retrieval of the mass balance, which is based upon the importance of the albedo for the energy balance. In chapter 5 we compare satellite SAR images of Vatnajökull with mass balance observations, modeling results from chapter 2 and albedo images from chapter 4. One aim is to find out what surface features of glaciers are visible on SAR images and to compare SAR images with albedo images. Another aim is to investigate whether SAR images can be used to retrieve the mass balance.

In chapter 6 we compare the results from the chapters 2, 4 and 5 with each other and with the in situ observations of the mean specific mass balance. Finally, in chapter 7, we look at the future of remote sensing of glacier mass balance.

# 2 A calibrated mass balance model for Vatnajökull*

**Abstract**

Vatnajökull (Iceland) is the largest icecap in the world where the energy and mass balance have been studied with good spatial and temporal resolution. In this paper we use these data to analyze the energy balance and to construct a calibrated and spatially distributed mass balance model. The incoming longwave radiation is best modeled as a function of meteorological variables in the free atmosphere just above the relatively thin katabatic layer, instead of those at the 2 m level. The ratio of changes in the 2 m temperature to changes in the free atmospheric temperature (the climate sensitivity) is smaller than 1. Therefore, when the bulk method is used to compute the turbulent fluxes, the 2 m temperature must be explicitly calculated. Otherwise the sensitivity of Vatnajökull to climatic change would be overestimated. When the model is forced with data from a permanent weather station not on the ice cap, it reproduces the observed mass balance reasonably well. Horizontal precipitation gradients over Vatnajökull are large, which results in a strongly varying sensitivity to external temperature changes over the ice cap. Local climatic conditions thus highly determine the mass balance and its sensitivity. For a temperature increase of 1 K and a simultaneous precipitation increase of 5.3%, the mean specific mass balance of Vatnajökull decreases by 0.56 m w.e.

## 2.1 Introduction

Many authors have studied the energy and mass balance of glaciers. In earlier studies single points on a glacier were studied (e.g., Ambach, 1963; Munro and Davies, 1978; Hay and Fitzharris, 1988). However, the mass balance depends strongly on altitude which is why others studied the energy balance along glacier transects (e.g., Braithwaite and Olesen, 1990; Munro, 1990; Greuell et al., 1997). Others have modeled mass balance gradients and sensitivities (e.g., Ambach and Kuhn, 1985; Oerlemans and Fortuin, 1992; Van de Wal and Oerlemans, 1994; Jóhannesson, 1997). Only a few authors have studied the surface of a glacier or ice cap in a three-dimensional way (e.g., Arnold et al., 1996, Oerlemans et al., 1999). Oerlemans et al. (1999) carried out a glacio-meteorological experiment on Vatnajökull (Iceland), which is the first ice cap where the melt process has been observed with good spatial and temporal resolution. In this work we use data from this experiment to analyze the energy balance and present a calibrated mass balance model which is based on a calculation of the surface energy balance. We force this model with

* Based on: De Ruyter de Wildt, M. S., J. Oerlemans and H. Björnsson. A calibrated mass balance model for Vatnajökull, Iceland. *Jökull*, submitted.

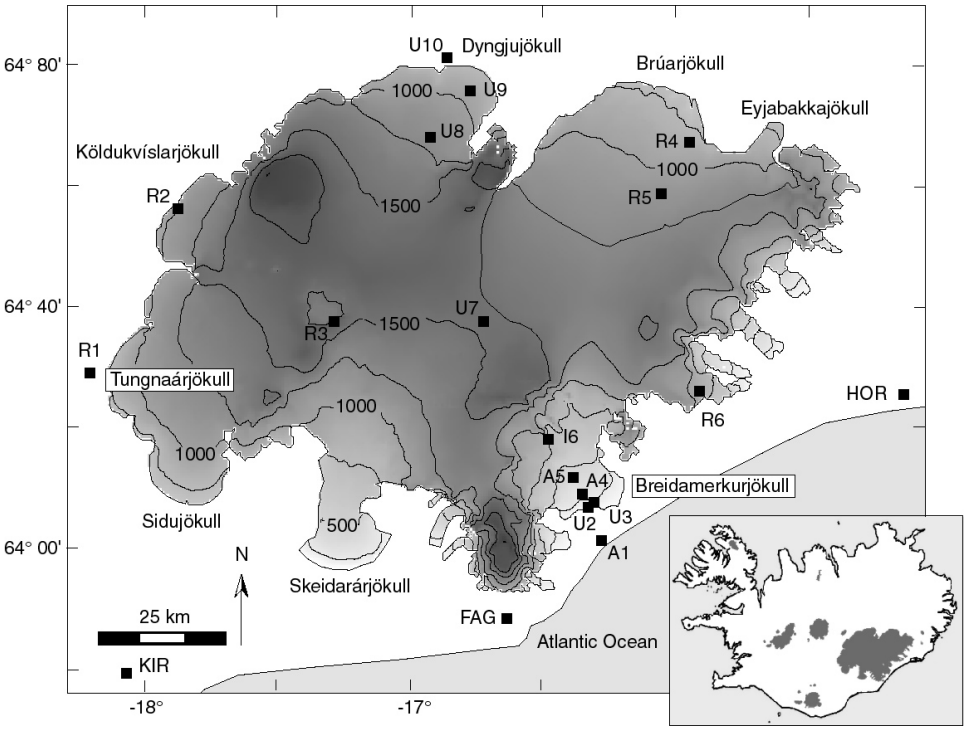


*Figure 2.1. Map of Vatnajökull based on the DEM used by the mass balance model. The horizontal resolution is 500 m and contourlines are shown for each 250 m interval. Indicated are the sixteen weather stations operated during the 1996 experiment and the names of the lobes. The permanent weather stations of Hornafjördur, Fagurshólsmyri and Kirkjubæjarklaustur are indicated with HOR, FAG and KIR, respectively.*

data from meteorological stations that are close to but not on the ice cap. For these stations long meteorological records are available with which we can calculate the mean specific mass balance over the last decades and study the sensitivity of Vatnajökull to external climatic change. Precipitation over Vatnajökull is largely unknown, which is why we use this quantity to tune the model to the mass balance data. The mass balance is evaluated at a number of sites distributed across the ice cap. A Digital Elevation Model (DEM) with a horizontal resolution of 500 m is used to obtain the altitude and other geographical features for these points (figure 2.1). The mean specific mass balance is then calculated with an interpolation scheme that was especially developed for this purpose.

Vatnajökull is located in southeastern Iceland and is one of the largest temperate ice caps in the world (8200 km$^2$ in 1995; see figure 2.1). The altitude ranges from sea-level to 2000 m with 88% of the surface between 700 and 1700 m. It comprises several domes that rest on volcanic caldera's, some large surging-type lobes and many smaller outlet glaciers. Since the end of the nineteenth century it has been the topic of much research, but only in the latest decades have data been gathered in a systematic way. Overviews of previous research are given by Björnsson et al. (1998a) and Williams et al. (1997). The experiment

reported in this paper was carried out in 1996 by research groups from the universities of Iceland, Utrecht (The Netherlands), Innsbruck (Austria) and from the *Vrije Universiteit* of Amsterdam (The Netherlands). Twelve Automatic Weather Stations were placed on the ice cap and four close to it (figure 2.1). All of these were operated from May 22nd till September 1st (Julian day 143-245) and measured, amongst other variables, 2 m temperature, 2 m humidity, 2 m windspeed, pressure and incoming and outgoing shortwave and longwave radiation. Furthermore, close to U2 radiosonde ascents were made twice daily. These produced profiles of temperature, humidity, windspeed and pressure up to an altitude of 10 km. Balloon soundings were made frequently near U3 and near I6 to probe the lowest 500 m of the atmosphere. Cloud observations were made approximately every 3 hours near station U2 and irregularly near station R5. The set-up of the experiment and the data are discussed in more detail in Oerlemans et al. (1999).

## 2.2 Energy balance parameterizations

Surface melt occurs when the energy balance at the surface (F) is larger than zero. F is given by

$$F = (1-\alpha)Q + I_{in} + I_{out} + H_s + H_l \qquad 2.1$$

where $\alpha$ is the surface albedo, Q the global radiation, $I_{in}$ the incoming longwave radiation, $I_{out}$ the outgoing longwave radiation, $H_s$ the turbulent flux of sensible heat and $H_l$ the turbulent flux of latent heat.

### *2.2.1 Global radiation*

Global radiation is computed according to the parameterization given by Greuell et al. (1997) which is based on Meyers and Dale (1983). This parameterization is valid for horizontal surfaces. Most of the surface of Vatnajökull slopes very gently, so we apply a first order approximation to take the surface inclination into account. The surface inclination only influences the direct solar radiation, so we distinguish between direct and diffuse shortwave radiation:

$$Q = Q_0\left[c_1 \cos(\theta_s - \theta_{srf}) + c_2 \cos\theta_s\right] T_r T_g T_w T_{as} T_{cl} F_{ms} F_{rs} F_{ho} \qquad 2.2$$

where $c_1+c_2=1$ and $Q_0$ denotes the solar irradiance at the top of the atmosphere, $\theta_s$ is the solar zenith angle, and $\theta_{srf}$ is the inclination of the surface in the direction of the sun. $\theta_s$ can be easily calculated from standard astronomical theory (e.g., Walraven, 1978). For clear skies $c_1$ is 0.9 and $c_2$ is 0.1 while for entirely overcast skies $c_1$ is 0 and $c_2$ is 1. $T_rT_g$, $T_w$, $T_{as}$ and $T_{cl}$ are transmission coefficients that account for Rayleigh scattering and absorption by

other gases than water vapor, absorption by water vapor, aerosol extinction and absorption by clouds, respectively. The first three coefficients can directly be calculated from meteorological variables. $T_{as}$ and $T_{cl}$ need to be tuned to the data, which is done in appendix 2A. Mean values of $T_r T_g$, $T_w$ and $T_{as}$ lie between 0.90 and 0.93 whereas the mean values of $T_{cl}$ lie between 0.67 (for station U3) and 0.85 (for station R3). The coefficients $F_{ms}$, $F_{rs}$ and $F_{ho}$ account for the amplification through multiple scattering at the surface, amplification through directly reflected radiation at the surface and attenuation by horizon obstruction. These three coefficients can be obtained from the DEM. $F_{rs}$ and $F_{ho}$ are close to 1 for all stations but $F_{ms}$ can be larger (up to 1.05 for station U7). Figure 2.2a displays hourly means of the observed and simulated global radiation for the stations for which cloud observations are available. Although the correlation is high (r=0.92), there is considerable scatter (the residual standard deviation is 96 W/m$^2$). This is probably caused by clouds of different optical thickness (see appendix 2A). Unfortunately we have no observations of optical thickness or cloud type.

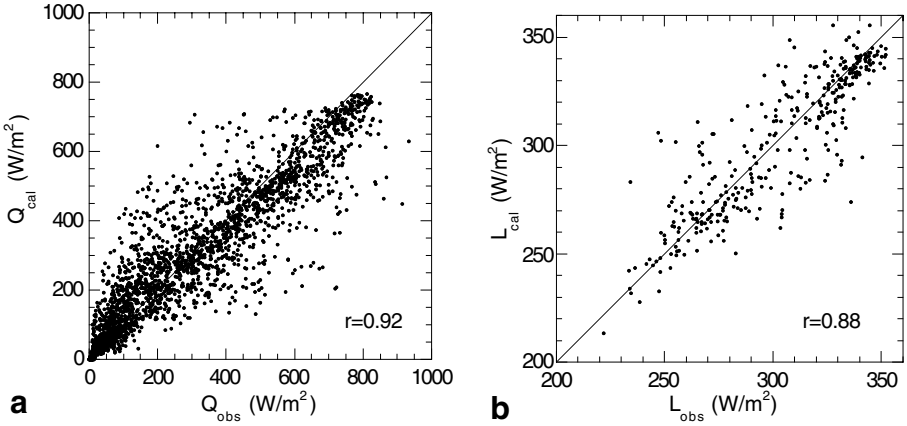


*Figure 2.2. Scatterplots of calculated against observed hourly means of global radiation and of the incoming longwave radiation. Only measurements from stations for which cloud observations are available are shown (A1, U2, A4, A5, I6, R4 and R5). For calculation of the incoming longwave radiation data from the radio soundings are used, which are available only twice a day.*

### *2.2.2 Albedo*

Snow albedo ($\alpha_{sn}$) depends on several climatological and surficial quantities and thus changes in time and space. These quantities are grain size, impurity content, cloudiness, solar inclination, liquid water content and surface roughness (e.g., Warren, 1982). The influence of most of these quantities on $\alpha_{sn}$ is not well understood and some simplifications have to be made when $\alpha_{sn}$ is parameterized. We use a parameterization that is based upon Oerlemans and Knap (1998). It describes the daily albedo as a function of aging of the snow and snowdepth. The parameterization and its calibration to the data are described in

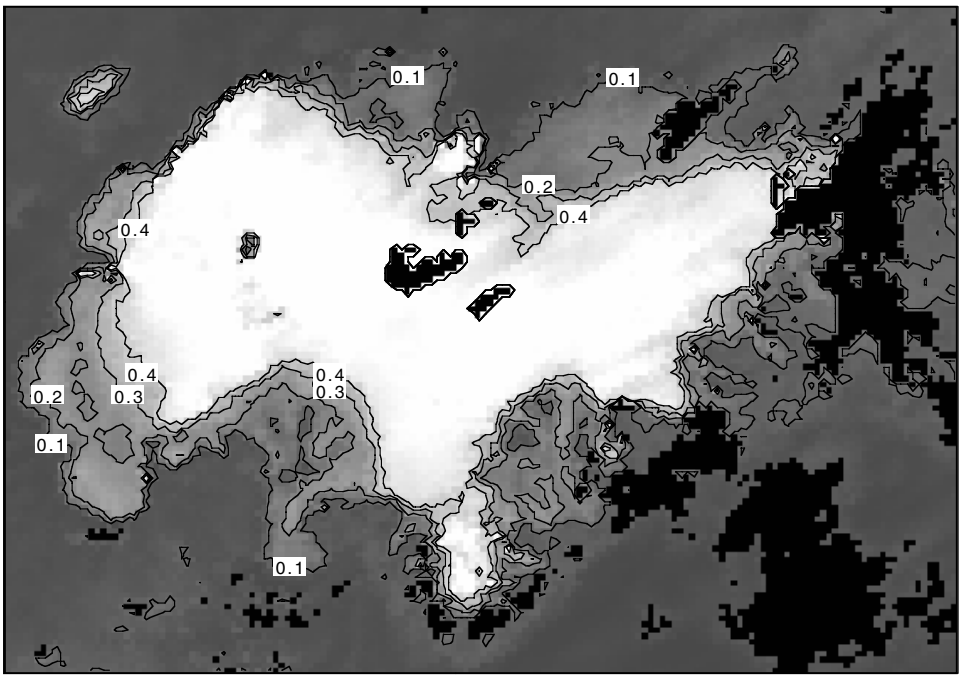


*Figure 2.3. NOAA AVHRR image of Vatnajökull, taken on August 23rd, 1998. It has been processed so that it represents the surface albedo. Contourlines are only shown for albedo values of 0.1, 0.2, 0.3 and 0.4. The black pixels represent clouds.*

appendix 2B.

The ice albedo displays large spatial variations over Vatnajökull which cannot be described with a simple parameterization. In the north and northwest (U8, U9 and R2) the mean ice albedo is very low (<0.10). As has been observed *in situ*, these low values are caused by black volcanic deposits, called tephra (Oerlemans et al., 1999). This tephra is deposited every few decades by one of the active volcanoes in the near surroundings of northwestern Vatnajökull (Larsen et al., 1998). The tephra melts out and accumulates in the ablation zone. To the south and to the east, the ice is cleaner, but the albedo has not been measured on all major outlets and it varies a lot in some areas. For example, the albedo values measured at the stations A4, A5, I6 and R4 are most likely not representative of their surroundings (Reijmer et al., 1999). These findings show that for a relatively large ice body such as Vatnajökull point measurements of the albedo cannot be interpolated over larger parts without further consideration.

With remote sensing techniques the albedo can be successfully determined over vast areas (e.g., Stroeve et al., 1997). We use satellite reflectance images to determine the ice albedo of different parts of Vatnajökull. We do not study the snow albedo in this way, because the snow albedo is more homogeneous on a horizontal scale than the ice albedo. Furthermore, there are too few usable satellite images to resolve changes in snow albedo. This does not hamper the determination of the ice albedo which is more constant in time.

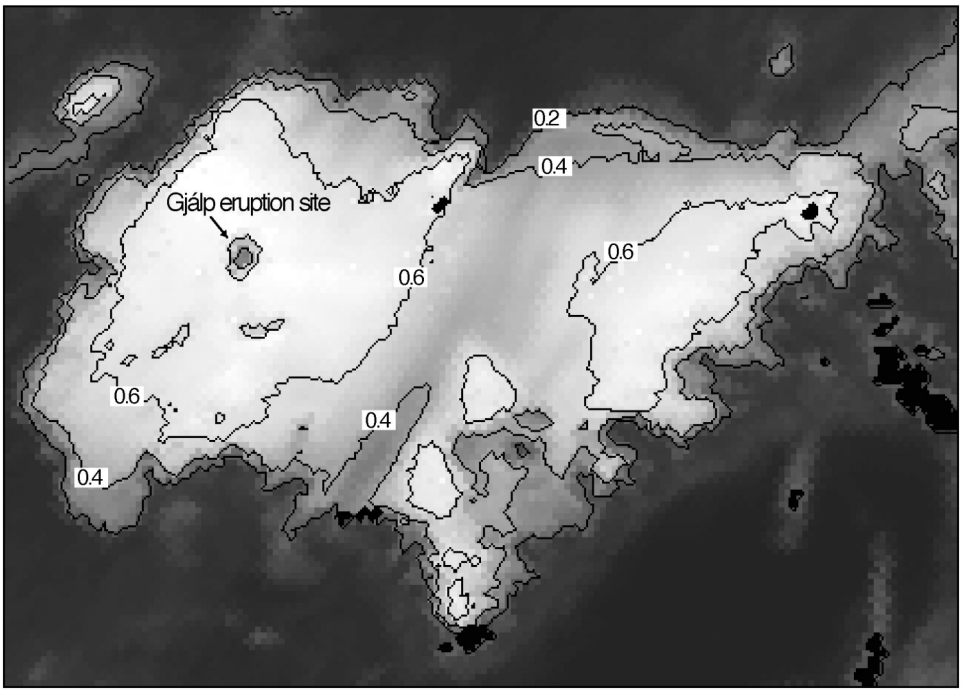


*Figure 2.4. NOAA AVHRR image of Vatnajökull, taken on June 26th, 1997. It has been processed so that it represents the surface albedo. The black pixels represent clouds.*

We use NOAA-AVHRR images (purchased from the Dundee Satellite Receiving Station in the U.K.) which have a resolution of 1.1 km at nadir. It is beyond the scope of this paper to describe the process of retrieving the surface albedo from the images in detail. The retrieval method is described in De Ruyter de Wildt et al. (2002b). The images were taken during the melting seasons (April - September) of several years so that both spatial, seasonal and yearly changes could be observed. On most images the firn line is clearly visible so ice and snow/firn can easily be distinguished. Figure 2.3 shows one of the images. It displays few clouds and much bare ice and shows that Breidamerkurjökull and Skeidarárjökull in the south have broad bands of low albedo and are quite inhomogeneous. Tungnaárjökull and Köldukvíslarjökull in the west are more homogeneous. The same is true for Dyngjujökull in the north but this outlet displays lower albedo values than the other ones (below 0.05 in places). Its neighboring outlet Brúarjökull displays low albedo values in the west and higher values in the east. For each model evaluation site we use the mean ice albedo that was determined for that site from the satellite images.

In November 1996 a volcanic eruption took place underneath Vatnajökull, which had a significant impact upon the ice cap (Gudmundsson et al., 1997). Above the eruption site the ice melted, causing a large flood or *jökulhlaup* south of Skeidarárjökull. The eruption also covered large parts of Vatnajökull with tephra which significantly lowered the albedo, as shown by the AVHRR image in figure 2.4. This image clearly displays a broad band of

low albedo over the central part of the ice cap. The drainage basins in the south-west (e.g. Tungnaárjökull) were not affected, but to the north and north-east (e.g. Dyngjujökull and Brúarjökull) we find an albedo lowering of 0.15 in the accumulation area, relative to other summers of comparable warmth. Even in 1998 some parts displayed a slightly lower albedo. In the model we therefore lower the albedo of snow and firn accordingly during the melting seasons of 1997 and 1998. Upon the albedo of the ablation areas the eruption had no measurable effect, presumably because there the albedo already was relatively low.

### 2.2.3 Longwave radiation

$I_{in}$ stems from the lowest part of the atmospheric boundary layer and from the upper-hemisphere slopes that surround a measurement site. For an exact calculation one needs to know the atmospheric profiles of temperature and humidity, but generally the influence of the vertical profiles can be well described with the temperature and water vapor pressure at screen-height, $T_a$ and $e_a$. We use a slightly altered version of the parameterization given by Greuell et al. (1997) which is based on Konzelmann et al. (1994) and which calculates $I_{in}$ as a function of $T_a$, $e_a$ and cloudiness. However, the katabatic layer over Vatnajökull is generally not very thick (Oerlemans et al., 1999) and $T_a$ and $e_a$ are not representative of that part of the atmosphere that generates $I_{in}$. Near A5, for example, the temperature inversion typically occurs in the lowest 20 to 30 m above the surface. This means that $I_{in}$, even for this station which is situated in the lower part of the ablation area, is only partly influenced by the katabatic layer and is best described as a function of meteorological variables in the free atmosphere (Meesters and Van den Broeke, 1996). When we tune the parameterization to the measurements of $I_{in}$ (appendix 2C), we indeed find that $I_{in}$ is best described as a function of the temperature and the water vapor pressure in the free atmosphere at the same altitude as the measurement site ($T_{atm}$ and $e_{atm}$). Apart from this, when the mass balance model is forced with external data, $T_a$ and $e_a$ need to be computed from the external data, which introduces extra uncertainty. When we compute $I_{in}$ from the cloud observations and from $T_{atm}$ and $e_{atm}$ (measured by the radio soundings), we obtain a correlation coefficient between computed and observed $I_{in}$ of 0.86. The residual standard deviation is 17.6 W/m$^2$ (figure 2.2b).

$I_{out}$ depends on the surface temperature and on the surface emissivity, which both were not measured. However, the emissivity of snow and glacier ice is very close to 1 (Warren, 1982), while we assume the surface temperature to be equal to $T_a$ when $T_a$ is below the freezing point. Otherwise, the surface temperature is set to 0°C.

### 2.2.4 Turbulent fluxes

$H_s$ and $H_l$ are calculated with the bulk transfer method (e.g., Munro, 1990). This method requires values of windspeed, temperature and humidity at the surface and at some height above the surface (usually 2 m) as input. The basis for the bulk method, Monin-Obukhov similarity theory, is not strictly valid when a low level wind maximum is present, as is the

case over sloping and melting glacier surfaces (Munro and Davies, 1978). In spite of this, recent work (Denby and Greuell, 2000) has shown that the bulk method only slightly overestimates $H_s$ and $H_l$. The roughness length for momentum ($z_0$) has been reported to vary considerably in space and time over the ice surface of Breidamerkurjökull, where values between 3 mm and 6 cm were found (Smeets et al., 1999). The large values were caused by ice hummocks up to almost 2 m in height, which developed during the melting season. The smallest values were measured before these hummocks developed and these values are comparable with those for smooth ice surfaces found in the literature (Morris, 1989). Unfortunately, the aforementioned kind of irregularities can hardly be modeled and, moreover, do not arise in all ablation areas of Vatnajökull. We therefore choose an intermediate value of 5 mm for $z_0$ over ice. Denby and Greuell (2000) remarked that the error in the calculated turbulent heat fluxes due to an order of magnitude error in $z_0$ will be roughly 25%. We expect this to be an upper limit for the error present in the calculated turbulent heat fluxes. For snow surfaces, where these problems literally and figuratively do not arise, we use a value of 0.1 mm for dry snow and 2 mm for wet snow. These values are often found for snow surfaces (Morris, 1989). The roughness lengths for heat and moisture are calculated from $z_0$ with the often-used expressions of Andreas (1987).

### *2.2.5 Insulation*

For most weather stations, the sum of observed net radiation and turbulent fluxes (as computed from observed 2 m variables) matches the energy that is required for the melt observed during the experiment (figure 2.5). At sites where tephra covered ice appeared at the surface (I6, U8, U9 and R2) the simulated amount of melt is too high. This is probably caused by insulation of the underlying ice (e.g., Bozhinsky et al., 1986; Kirkbride, 1995), because in the thermal channels of the NOAA satellite these parts of Vatnajökull appear slightly warmer than the rest of the ice cap surface. For the stations I6, U9 and R2 the observed melt corresponds to about 80% of the melt energy that was available when the surface was snow-free. For station U8 there was tephra-covered ice at the surface only during a few days of the 1996 experiment and the effect of insulation is small here. A reduction of melt by 20% is plausible, for this corresponds to a tephra layer of a few cm (e.g., Kirkbride, 1995). We do not attempt to model this effect elaborately, because it concerns only a minor part of the ablation area. Only on Dyngjujökull a significant part of the ablation area is covered by tephra or other debris (figure 2.3). Furthermore, information needed to do so (notably thickness and thermal conductivity of the layer) is not available. We simply reduce the melt by 20% when the albedo is 0.15 or lower.

## 2.3 Reconstruction of the mass balance

We compute the mass balance (B) as the annual sum of ablation and solid precipitation:

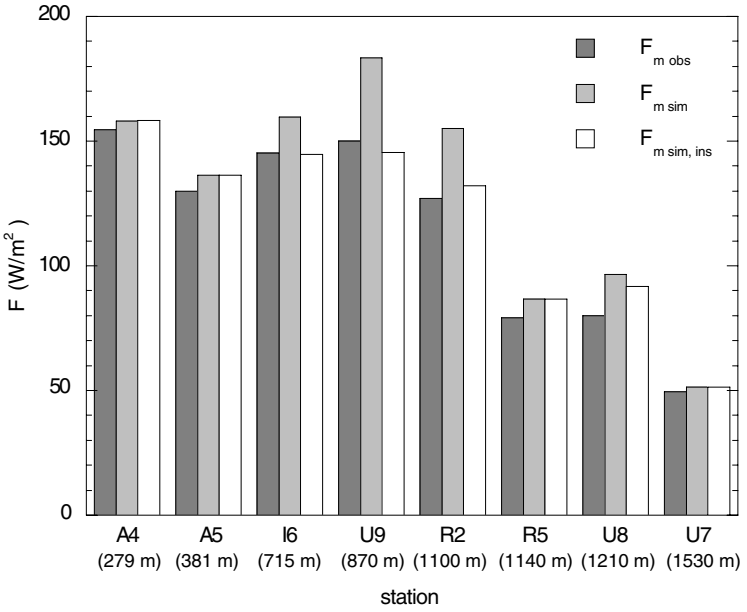


*Figure 2.5. Mean energy used for melting ($F_m$) during the 1996 experiment. Only those stations are shown where the net radiation was measured during the entire experiment. Shown are the values obtained from the observed melt (obs), the simulated values without the effect of insulation (sim) and the simulated values with this effect (sim, ins). The simulated values are obtained from the observed net radiation and the turbulent fluxes calculated from the observed 2 m values of meteorological variables.*

$$B = \int_{year} \left[ \min\left(0; -F / L_m\right) + P + H_l / L_s \right] dt \qquad 2.3$$

where $F/L_m$ is the ablation rate, $L_m$ the latent heat of melting of ice, P the solid precipitation rate and $L_s$ the latent heat of sublimation. The time step that we use is 30 min and we let the balance year start on September 21$^{st}$ (Julian day 265). We neglect the refreezing of meltwater, so meltwater is assumed to run off immediately. During field work in the years 1992-1995, nowhere on the ice cap superimposed ice was found (Björnsson et al., 1998a). Furthermore, the refreezing process is only important when the winter snowpack is cold (e.g., Colbeck, 1975) and the ablation season is short (Greuell and Oerlemans, 1986). Winters in Iceland are relatively mild and the ablation season on Vatnajökull is long. At station U7 (1530 m a.s.l.) the ablation season lasts about 120 days and at station U3 (169 m a.s.l.) about 220 days.

Both the ablation rate and the accumulation rate of an ice body are largely determined by the conditions of the atmosphere that surrounds it. We assume all meteorological variables in the free atmosphere, except precipitation, to be horizontally homogenous around Vatnajökull. This seems justified, for when the height difference is taken into account, the mean temperatures of three stations that lie at very different locations are

nearly the same: 9.3, 9.4 and 9.3°C for A1, U10 and R1, respectively. The tuning of the coefficient for aerosol extinction (appendix 2A) and of the emissivity of clear skies (appendix 2C) also indicate that the free atmosphere was horizontally homogeneous, for all stations display the same results. Because of this assumption the model can be forced with data from a single permanent weather station. We use a permanent weather station outside of the ice cap so that we can reconstruct a long mass balance record and study the sensitivity of Vatnajökull to external climatic changes. There are three such stations close to Vatnajökull: one in Hornafjördur, one in Fagurshólsmyri and one in Kirkjubæjarklaustur (figure 2.1). Hornafjördur is much more influenced by clouds and damp air from the ocean than most of Vatnajökull. The station in Fagurshólsmyri has no long records of humidity, so the station in Kirkjubæjarklaustur (named KIR hereafter) is the most suitable to force the mass balance model. Data that are available from this station and that are used to force the model are daily means of temperature, vapor pressure, pressure and cloudiness from 1965 to 1999. Upon the temperature we impose a daily cycle with an amplitude of 2.2 K, which is the observed mean daily amplitude at the stations A1, U10 and R1. Precipitation in KIR was found to be not particularly well correlated to the observed winter mass balance of northern and western Vatnajökull. The precipitation measured in Fagurshólsmyri proved to be more useful, which is why we force the model with monthly values from this station.

### *2.3.1 Variables in the free atmosphere*

The temperature in the free atmosphere influences $l_{in}$ (see appendix 2C) and the occurrence of solid precipitation. It is calculated from the temperature at KIR ($T_0$) and the atmospheric lapse rate ($\gamma_{atm}$), which is obtained from the radiosonde data (-5.8 K/km). The atmospheric pressure (p) is extrapolated from the pressure measured in KIR ($p_0$) with the same exponential decrease with altitude as was measured by the radiosondes. Vapor pressure in the free atmosphere ($e_{atm}$) is calculated by assuming a constant relative humidity with altitude. The radiosonde data showed that this was, on average, the case.

### *2.3.2 Variables in the katabatic layer*

When melting conditions prevail a cool katabatic surface layer develops in which temperature and wind speed deviate from their values in the free atmosphere. All weather stations on the ice cap, except U7, R3 and R6, display a preferred wind direction (Oerlemans et al., 1999). This means that a large part of the ice cap is subject to a more or less persistent katabatic wind regime which shields the surface from fluctuations in the atmosphere. This is clearly reflected in the sensitivities of 2 m variables to external changes (table 2.1). The sensitivity of $T_a$ to external temperature changes, $dT_a/dT_{atm}$, is smallest for the lowest stations and increases with altitude. It approaches 1 for the stations where a katabatic layer was weak or absent (U7 and R3 high in the accumulation area and R6 on an open spot at the very glacier margin). Neglecting the small sensitivities of the 2 m variables leads to an over-estimation of the sensitivity of the turbulent fluxes to external temperature changes

| Station | Altitude (m) | $dT_a/dT_{atm}$ | | $du_a/dT_{atm}$ ($m\ s^{-1}\ K^{-1}$) |
|---|---|---|---|---|
| | | Obs. | Cal. | Obs. |
| U3 | 165 | 0.32 ± 0.05 | 0.34 ± 0.00 | 0.30 ± 0.08 |
| A4 | 279 | 0.38 ± 0.05 | 0.38 ± 0.01 | 0.18 ± 0.10 |
| A5 | 381 | 0.41 ± 0.05 | 0.43 ± 0.01 | 0.12 ± 0.08 |
| I6 | 715 | 0.62 ± 0.05 | 0.57 ± 0.01 | -0.04 ± 0.09 |
| R6 | 820 | 0.94 ± 0.06 | 0.62 ± 0.01 | 0.17 ± 0.14 |
| R4 | 830 | 0.70 ± 0.07 | 0.62 ± 0.01 | 0.21 ± 0.11 |
| U9 | 870 | 0.74 ± 0.08 | 0.63 ± 0.01 | 0.32 ± 0.09 |
| R2 | 1100 | 0.62 ± 0.07 | 0.73 ± 0.02 | -0.20 ± 0.13 |
| R5 | 1140 | 0.75 ± 0.06 | 0.75 ± 0.02 | 0.05 ± 0.12 |
| U8 | 1210 | 0.78 ± 0.08 | 0.78 ± 0.02 | 0.19 ± 0.12 |
| U7 | 1530 | 0.99 ± 0.08 | 0.91 ± 0.02 | -0.12 ± 0.11 |
| R3 | 1712 | 0.95 ± 0.09 | 0.99 ± 0.03 | -0.02 ± 0.15 |

*Table 2.1. Observed and simulated sensitivities of temperature and windspeed at screen-height. The sensitivities were obtained by fitting a straight line to daily mean values.*

(Greuell and Böhm, 1998).

From a physical point of view, parameterizations of the 2 m variables should be based upon the dynamic equations that describe the turbulent exchange of momentum, heat and moisture. However, the dynamics of the katabatic layer are very complex and external effects such as advection further complicate the situation. On the other hand, when we analyzed the data we found that $T_a$ can be adequately described by empirical relations. Although these relations have no physical basis, they do result in correct sensitivities. $T_a$ decreases linearly with altitude (Oerlemans et al., 1999) and we found that this

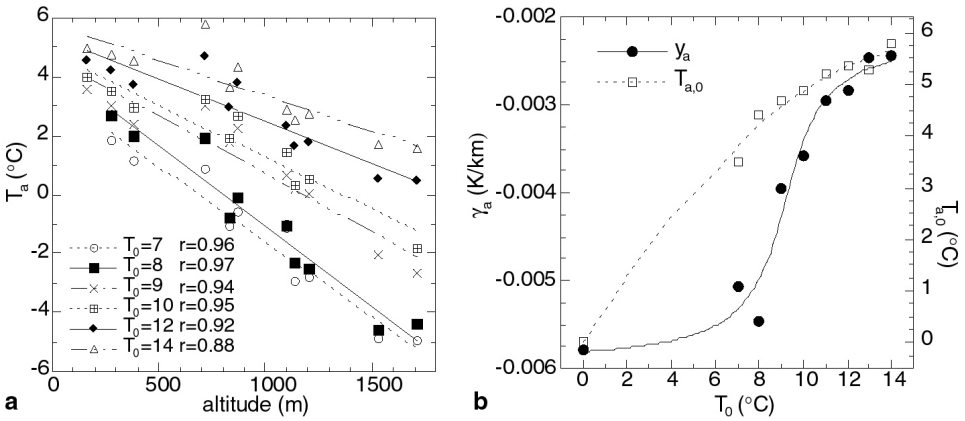


*Figure 2.6a: Average 2 m temperature ($T_a$) as a function of surface altitude, for different values of the temperature in Kirkjubæjarklaustur ($T_0$); b: 2 m lapse rate ($\gamma_a$) and 2 m temperature deviation at sea-level ($T_{a,0}$) as a function of $T_0$, both determined from the linear regressions in plot a. The data points for $T_0$=0°C are boundary conditions.*

decrease changes with $T_0$ (figure 2.6a). We therefore write

$$T_a = T_{a,0} + \gamma_a z \qquad 2.4$$

where $T_{a,0}$ is $T_a$ at sea-level, $\gamma_a$ is the lapse rate of $T_a$ and z is the altitude. The dependence of both coefficients in equation 2.4 upon $T_0$ is shown in figure 2.6b. For low temperatures hardly any katabatic flow exists and $\gamma_a$ nearly equals $\gamma_{atm}$. For higher temperatures, $\gamma_a$ grows less negative and $T_{a,0}$ deviates more from $T_0$. For high values of $T_0$, $\gamma_a$ approaches -2.5 K/km. $\gamma_a$ is best described by an inverse tangent (figure 2.6b):

$$\gamma_a = -0.0041 + 0.0012 \arctan\left[0.77(T_0 - 9.2)\right] \qquad 2.5$$

When we impose the boundary condition that $T_{a,0}$ equals $T_0$ for $T_0$ is 0°C, we can describe the dependence of $T_{a,0}$ upon $T_0$ with (figure 2.6b):

$$T_{a,0} = 0.68\,T_0 - 0.020\,T_0^2 \qquad 2.6$$

So the higher $T_0$, the less negative $\gamma_a$ and the more negative the deviation of $T_a$ from $T_{atm}$. These results are not surprising because the katabatic layer, which reduces $T_a$ and $\gamma_a$, is better developed at higher temperatures. Table 2.2 shows that mean observed and simulated values of $T_a$ correspond reasonably well. The parameterization of $T_a$ produces mean errors between 0 and 1.2 K, but this error is much smaller than the mean difference between $T_{atm}$ and $T_a$. The sensitivities that result from the parameterization correspond well the observed sensitivities (table 2.1).

For the 2 m windspeed ($u_a$) the picture is different. For some stations where the katabatic forcing is strong (U3, A4, U8, U9 and R4), $du_a/dT_{atm}$ is 0.2 to 0.3. However, the uncertainties are large for these stations and even larger for the other stations, which

| Station | Altitude (m) | $dT_a$ (K) | $du_a$ (m/s) |
|---|---|---|---|
| U3 | 165 | 0.12 | -1.57 |
| A4 | 279 | 0.23 | -0.44 |
| A5 | 381 | 0.38 | 0.52 |
| I6 | 715 | 1.17 | 1.15 |
| R6 | 820 | 1.19 | 0.04 |
| R4 | 830 | 0.27 | -1.15 |
| U9 | 870 | 1.13 | -0.38 |
| R2 | 1100 | 0.60 | -1.30 |
| R5 | 1140 | 0.30 | -0.18 |
| U8 | 1210 | 0.10 | -0.29 |
| U7 | 1530 | 0.46 | 0.54 |
| R3 | 1715 | 0.02 | 0.36 |

*Table 2.2. Differences between mean observed and mean simulated daily mean values of 2 m temperature ($dT_a$) and windspeed ($du_a$) during the 1996 experiment.*

display no significant sensitivities. We therefore do not develop a parameterization for $u_a$. Instead we use the mean wind speed in the free atmosphere. Data from the radiosondes show that this quantity increased from 3.3 m/s at sea-level to 7.1 m/s at 2000 m. For U3, R2 and R4 this results in a mean wind speed that is much too low, while for I6 it is much too high (table 2.2). The former three stations lie at the very margin of the ice cap and experience strong katabatic winds. They represent, however, only a very small part of Vatnajökull. I6 is situated near nunataks that probably provide shelter from the wind.

| Station | Altitude (m) | <n> summer 1996 | <n> summer 1966-1996 |
|---|---|---|---|
| U2 | 50 | 0.750 | |
| R5 | 1140 | 0.694 | |
| Hornafjördur | 0 | 0.803 | 0.808 |
| Kirkjubæjarklaustur | 35 | 0.764 | 0.764 |

*Table 2.3. Mean observed cloudiness (<n>) for several locations and periods.*

### *2.3.3 Cloudiness*

Cloudiness was observed every three hours close to U2 in the south and less regularly near R5 in the north. Mean values of cloudiness for these two stations and for the stations in Hornafjördur and KIR are shown in table 2.3. More information about the mean cloudiness can be gained by assuming the cloud observations of station U2 to be valid for all stations and then comparing mean calculated with mean observed global radiation. Figure 2.7 shows that for most stations the correspondence is good. For some stations there are large deviations, which are most likely caused by an erroneous cloud factor. Other factors in equation 2.2 cannot produce such large deviations. For U9, U10, R1, R3 and R6 the calculated values are too high, so for these stations the mean cloudiness and/or the optical thickness must have been higher than at U2. R3 was located near the small subglacial geothermal area of Grimsvötn and was often surrounded by fog. R6 was located near Hornafjördur, where the mean cloudiness was higher than at U2 (table 2.3). For U9, U10 and R1 no other indications of a low cloud factor are available. Note, however, that U10 and R1 were not located on but close to the ice cap.

Forcing the model with a fixed cloudiness would result in considerable errors in the cloud factor $T_{cl}$ due to the non-linear relation between n and $T_{cl}$ (see appendix 2A). It is therefore better to force the model with daily values of cloudiness, and it seems best to use values measured in KIR. This is expected to introduce errors over the lowermost ablation zones in the north, the southeast (not over Breidamerkurjökull) and perhaps in the west.

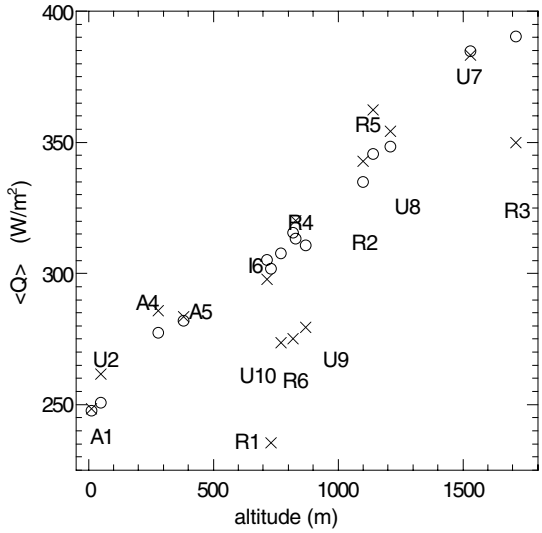


*Figure 2.7. Mean observed (circles) and simulated (crosses) values of the global radiation over Vatnajökull as a function of altitude. In order to minimize errors in the observations, measurements corresponding to high solar zenith angles (>80°) were not used for this comparison.*

### *2.3.4 Precipitation and tuning of the model*

Because the albedo depends upon the number of days since the last snowfall, it is important to simulate the time between subsequent snowfalls correctly. When we assume that precipitation falls every 5$^{th}$ day, and define days with snowfall as days with precipitation and a daily mean temperature below 3°C (in the free atmosphere above the katabatic layer), the mean albedo in the accumulation area is simulated correctly. The amount of precipitation is difficult to simulate. Most precipitation is brought to the ice cap with southerly and easterly winds and because of its size and height Vatnajökull acts as a topographic barrier to these winds. This results in high horizontal precipitation gradients with the highest precipitation near the coast. The exact amount of yearly precipitation is only known at a few locations near the coast and we will have to use it for final tuning. We assume that the precipitation gradients are fixed in time, so:

$$dP = dP_{fag} \frac{P}{P_{fag}} \qquad 2.7$$

where dP is the daily precipitation at a site on the ice cap; $dP_{fag}$ the daily precipitation in Fagurshólsmyri; $P_{fag}$ the mean annual precipitation in Fagurshólsmyri; and P the mean annual precipitation for the site on the ice cap. For all sites where the mass balance has been measured regularly, we calibrate P so that the modeled annual mean B is equal to the

observed annual mean B (over the years 1993 to 1999). The resulting precipitation field must be interpolated to the model evaluation sites, but the measurement sites are irregularly distributed over the ice cap and do not resolve many of the altitudinal gradients. Hence, we make a distinction between horizontal and vertical gradients. Precipitation is often found to double in a certain altitude interval so we write:

$$P = P_0 k^{z/1000} \qquad 2.8$$

where $P_0$ is the mean annual precipitation at a reference altitude and k is a constant (e.g., for a doubling per 1000 m, k has a value of 2). We fit this equation to the winter mass balance data, which are available for the years 1993 to 1999 (Björnsson et al., 1997, 1998a, b, c, 1999; Gudmundsson, 2000; Sigurdsson, 1997). These data were mainly obtained over the northwestern part of Vatnajökull, including most of the accumulation area. For Öraefajökull (the southernmost dome of Vatnajökull) we also use precipitation data from the permanent weather station in Fagurshólsmyri. When we correct the data for the small amounts of ablation and rainfall that occur during the winter season (both corrections are calculated with the mass balance model), we find a values of 2.3 for k. This value approximately corresponds to a doubling of the precipitation each 830 m. At each measurement site, we can now reduce P to its value ($P_0$) at sea-level. The resulting $P_0$ values vary smoothly over the ice cap and we can interpolate them to the model evaluation sites with Kriging interpolation (e.g., Cressie, 1993). This interpolation technique is suitable for smooth interpolation of unevenly distributed data such as the mass balance observations that we use. At each model evaluation site we then calculate P with equation 2.8.

## 2.4 Results

### *2.4.1 Energy balance*

Observed and modeled components of the energy balance are displayed in figure 2.8. All components change with altitude and this is simulated by the model. $Q_{in}$ and $\alpha$ logically increase with altitude, whereas the net longwave radiation and the turbulent fluxes decrease with altitude. For station U9, and to a lesser extent for A4, A5 and I6, the modeled cloud factor is too low and hence the calculated global radiation is too high. Significant differences in the percentage of reflected shortwave radiation are present for A4, A5, and R2. For A4 and A5 this is caused by the ice albedo which is not representative of the surrounding ice. The model uses a more representative value. In the model results the snow disappears too soon at station R2 so the modeled mean albedo is too low. This is a consequence of tuning the model precipitation with mass balance data from several years. Errors in the turbulent heat fluxes mainly result from errors in the calculated meteorological variables at screen-height. Note that for U9 and R2 part of the available energy is not used for melting due to insulation.

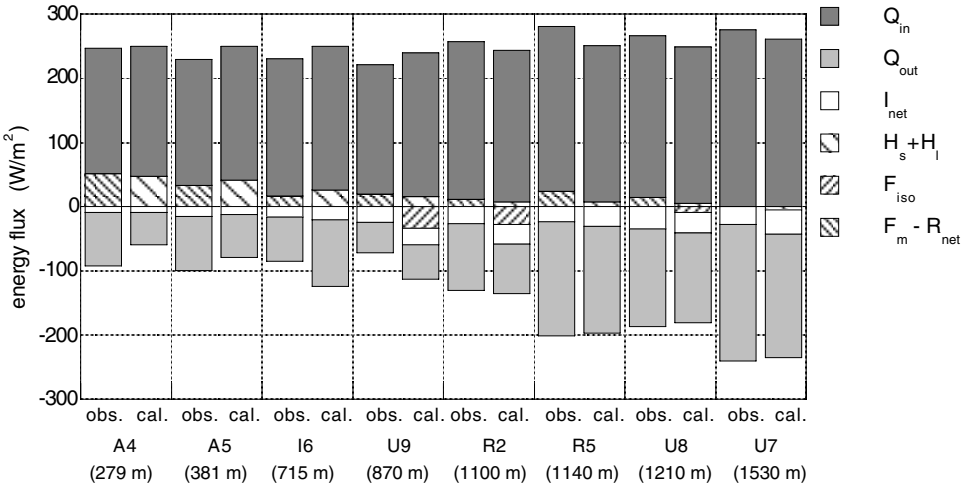


*Figure 2.8. Mean observed (obs.) and calculated (cal.) components of the energy balance during the 1996 experiment. Those stations are shown where all radiation components have been measured. $Q_{out}$ is the reflected shortwave radiation, $I_{net}$ the net longwave radiation , $F_{iso}$ the energy used to heat up the insulating layer, $F_m$ the melt energy and $R_{net}$ the net radiation. Other symbols are explained in the text. $H_s$, $H_l$ and $F_{iso}$ (if applicable) have not been measured directly, but the sum of these three modeled components should be equal to the observed difference between $F_m$ and $R_{net}$.*

### *2.4.2 Mean specific mass balance*

We compute the mean specific mass balance ($B_m$) with an interpolation scheme that has been especially designed for this purpose. With this interpolation scheme vertical gradients are taken into account, even when the evaluation sites do not resolve changes in altitude. For each grid point of the DEM we determine the $n_s$ closest evaluation sites that do not differ more than 500 m in altitude from the grid point. Then, because of the limited height differences, a linear relation between mass balance and altitude can be found for the $n_s$ evaluation points. With this relation the mass balance at the altitude of the gridpoint is calculated. In order to avoid discontinuities in the resulting mass balance field, the contribution of each evaluation point is weighted with the inverse of its distance to the grid point. The algorithm works best when for all parts of the ice cap, the entire altitudinal range is represented by the evaluation points. In order to fulfill this condition we use 128 evaluation points, and with $n_s$=6 good results are obtained. Figure 2.9 shows the annual precipitation and B, interpolated over the whole ice cap and averaged over the period 1965 - 1999. The same figure also shows the 128 evaluation sites. Clearly most precipitation falls in the south and southeast, which is due to predominant southerly to easterly wind direction. Most precipitation falls on top of Öræfajökull, the highest part of Vatnajökull which lies in the south almost 9 m annually. The glacier tongues in the south and southeast also receive

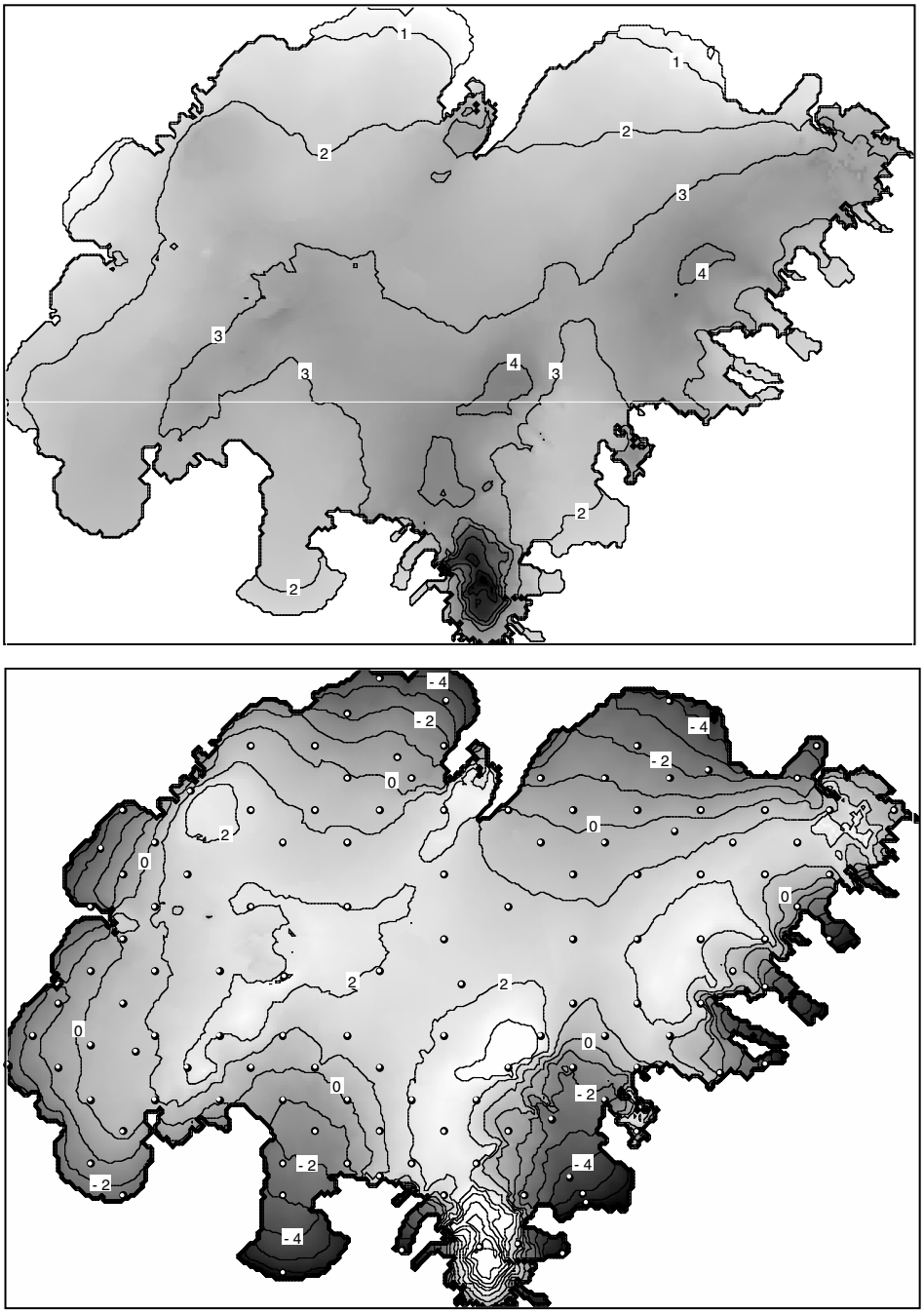


*Figure 2.9. Modeled annual precipitation (top plot) and annual mass balance (bottom plot), averaged over the period 1965 - 1999. Both quantities are given in m w.e. In the bottom plot the locations are shown for which the mass balance is computed.*

more precipitation than the ablation areas in the north and northwest, even though the latter are situated on higher grounds. Consequently, the Equilibrium Line Altitude (ELA) in the south and southeast is lower than in the northwest (figure 2.9). The ELA ranges from about 1000 m at some locations in the south and southeast to over 1400 m on Dyngjujökull and Köldukvíslarjökull in the northwest. The accumulation area ratio of Vatnajökull is found to be 64%.

Figure 2.10 shows the simulated mean specific mass balance of the northwestern drainage basins of Vatnajökull as a function of time. The winter mass balance has slightly increased between 1965 and 2000, whereas the summer mass balance has decreased. As a result the annual mean specific mass balance decreased from slightly positive in the 1970s to near-neutral in the 1990s (changes in glacier surface not taken into account). In general, fluctuations in winter and summer balance are more or less equally large. Interestingly, the most extreme positive and negative annual values both occur in the early 1990s and are both due to summer conditions. In 1991 the summer was exceptionally sunny and warm, whereas in 1992 the summer was cool with considerable snowfall in June and August (Björnsson et al., 1998a). The model reproduces $B_m$ over the years 1993 to 1999 fairly well (we estimate the uncertainty in the measured $B_m$ to be 0.25 m w.e.). The effect of the albedo lowering due to the volcanic eruption of November 1996 is adequately simulated: without the additional lowering of the snow albedo during the summer of 1997, the simulated mass balance would have been considerably too high. Table 2.4 displays correlation coefficients between observed and modeled $B_m$ for all drainage basins where

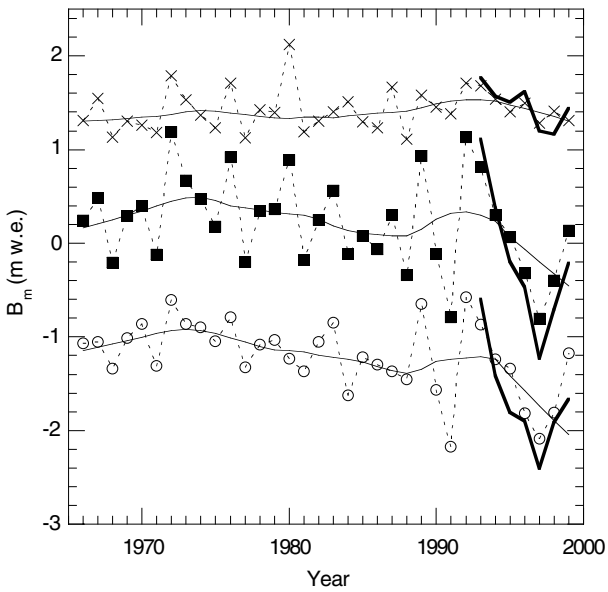


*Figure 2.10. Observed (thick solid lines) and reconstructed (dashed lines) mean specific mass balance for the northwestern part of Vatnajökull (formed by the drainage basins Tungnaárjökull, Köldukvíslarjökull, Dyngjujökull and Brúarjökull). Shown are the winter balance (crosses), the summer balance (open circles) and the annual balance (solid squares). The thin solid lines are smoothed curves.*

| Region | Area (km$^2$) | Winter | Summer | Annual |
|---|---|---|---|---|
| Tungnaárjökull | 491 | 0.86 | 0.81 | 0.93 |
| Köldukvíslarjökull | 330 | 0.65 | 0.89 | 0.98 |
| Dyngjujökull | 1239 | 0.77 | 0.92 | 0.96 |
| western Brúarjökull | 956 | 0.68 | 0.82 | 0.95 |
| eastern Brúarjökull | 780 | 0.65 | 0.90 | 0.97 |
| Eyjabakkajökull | 121 | 0.42 | 0.76 | 0.86 |

*Table 2.4. Correlation coefficients between observed and modeled mean specific mass balance for the drainage basins where the mass balance has been measured.*

the mass balance has been measured. In general the correlations are good, although for the winter mass balance the correlations are low for some drainage basins. This is obviously caused by the distribution of precipitation over Vatnajökull, which varies from year to year, whereas we use a fixed distribution of precipitation. Vatnajökull is sufficiently high and large to act as a topographic barrier, so the distribution of precipitation depends upon the large-scale atmospheric circulation.

## 2.5 The sensitivity of Vatnajökull to climatic change

We compute the sensitivity of $B_m$ to a change in a variable x as (Oerlemans, 1996):

$$C_x = \partial B_m / \partial x = \left[ B_m(x + dx) - B_m(x - dx) \right] / 2dx \qquad 2.9$$

where dx is the change in variable x. We compute the sensitivity to changes in the two most important atmospheric variables, temperature (dT=1K) and precipitation (dP=10%). We perturb these variables over the period 1965 - 1999 and then compute the average change in $B_m$ over this period. Table 2.5 shows $C_T$ and $C_P$ for different parts of Vatnajökull. Most obviously, $C_T$ varies strongly over Vatnajökull (third column). In regions with high precipitation in the south and east $C_T$ is, depending on hypsometry, up to 70% higher than in the drier regions in the northwest. The same relation has been observed for a set of climatologically very different glaciers (Oerlemans and Fortuin, 1992) and our results fit well in this picture: $C_T$ is almost -0.8 m w.e./K for glaciers with high precipitation and about -0.50 m w.e./K for drier glaciers. Thus, the precipitation gradients over Vatnajökull cause the sensitivity to temperature changes to vary considerably over the ice cap. Differences in precipitation also result in differences in $C_P$, but this sensitivity varies less over Vatnajökull.

Under the influence of increasing concentrations of greenhouse gases in the atmosphere, an annual temperature increase of about 0.3 K per decade is expected for Iceland in the next decades (Houghton et al., 1996). For Vatnajökull an external temperature increase of 1 K implies a decrease of $B_m$ with 0.71 m w.e. When we add an increase in precipitation of 5.3% for a warming of 1 K (Huybrechts et al., 1991), the decrease is smaller but still 0.56 m w.e.

| Region | Area ($km^2$) | $P_m$ (m) | $C_T$ (m w.e./K) | $C_P$ (m w.e. /10%) |
|---|---|---|---|---|
| Sidujökull | 514 | 2.7 | -0.76 | 0.31 |
| Tungnaárjökull | 491 | 2.0 | -0.77 | 0.30 |
| Köldukvíslarjökull | 330 | 1.7 | -0.50 | 0.28 |
| Dyngjujökull | 1239 | 2.0 | -0.49 | 0.28 |
| western Brúarjökull | 956 | 2.3 | -0.62 | 0.29 |
| eastern Brúarjökull | 780 | 2.5 | -0.73 | 0.30 |
| Eyjabakkajökull | 121 | 2.4 | -0.74 | 0.27 |
| Fláajökull | 173 | 3.3 | -0.73 | 0.32 |
| eastern Breidamerkurjökull | 631 | 3.0 | -0.69 | 0.32 |
| western Breidamerkurjökull | 384 | 3.1 | -0.80 | 0.35 |
| eastern Skeidarárjökull | 1002 | 3.1 | -0.61 | 0.34 |
| western Skeidarárjökull | 434 | 2.8 | -0.75 | 0.31 |
| Vatnajökull | 8198 | 2.6 | -0.65 | 0.31 |

*Table 2.5. Static sensitivities of the mean specific mass balance of various parts of Vatnajökull to changes in free atmospheric temperature and precipitation. All quantities are given as the mean during the period 1965 to 1999.*

## 2.6 Discussion and conclusions

We have presented a mass balance model for Vatnajökull which has been calibrated with an extensive data set. This made it possible to study differences between the free atmosphere and the katabatic layer. The calibration of the parameterization for $I_{in}$ demonstrated that over Vatnajökull, $I_{in}$ is better described as a function of $T_{atm}$ and $e_{atm}$ than as a function of $T_a$ and $e_a$. This is a consequence of the moderate size of Vatnajökull, which allows advection of relatively warm air over the ice cap. This air strongly determines $I_{in}$, as the katabatic layer is not very thick. Nevertheless, the katabatic layer is well enough developed for $T_a$ to deviate significantly from $T_{atm}$. The model presented in this paper uses the bulk method to compute the turbulent fluxes, which requires temperature, humidity and windspeed at the 2 m level. This means that it is important to make a distinction between these variables in the free atmosphere and in the katabatic surface layer. Most importantly, $T_a$ differs from $T_{atm}$, such that the sensitivity $dT_a/dT_{atm}$ is smaller than 1 (see table 2.1). If $T_a$ were not explicitly calculated but simply set equal to $T_{atm}$ ($dT_a/dT_{atm}=1$), using the bulk method would result in a value of $C_T$ that is too high. The over-estimation of $C_T$ in such a case is large: about 70%, which is much larger than Greuell and Böhm (1998) found for the Pasterze in the Austrian Alps (22%). Other mass balance models that are based upon a calculation of the energy balance often use a simplification of the bulk method (e.g. Oerlemans, 1992, Van de Wal and Oerlemans, 1994):

$$H_s = C(T - T_s) \qquad 2.10$$

where C is the transfer coefficient, T is the air temperature and $T_s$ is the surface temperature. These models use the temperature in the free atmosphere ($T_{atm}$) for T in equation 2.10 and do not require $T_a$. For $C=H_s/(T_{atm} - T_s)$ we find values of 3.5-5 $Wm^{-2}K^{-1}$, which is somewhat lower than the values used by Oerlemans (1992) (7 $Wm^{-2}K^{-1}$). Other authors (e.g. Kuhn, 1989; Braithwaite, 1995) calculate C from 2 m variables and obtain values between 6 and 31 $Wm^{-2}K^{-1}$. These values compare well with the values that we find for $H_s/(T_a - T_s)$ and that are two to three times as high as $H_s/(T_{atm} - T_s)$ (i.e. 9-13 $Wm^{-2}K^{-1}$). So when $T_a$ is explicitly calculated in the mass balance model, the bulk method can be used, but when only $T_{atm}$ is available and is equation 2.10 is used, a correct transfer coefficient equal to $H_s/(T_{atm} - T_s)$ should be applied.

Another difference with some other models (e.g. Oerlemans, 1992) is the dependence of snow albedo upon the age of surface snow. The age of the snow depends upon on the occurrence of snow fall, and for Vatnajökull the occurrence of summer snow fall in the accumulation area is strongly related to temperature. Modeling the albedo of snow as a function of snow age will therefore increase $C_T$ with respect to a model with constant snow albedo. When we use a constant mean value of 0.72 for the albedo of snow, we find that $C_T$ is roughly 25% lower. This difference is of the same order of magnitude as, but opposite to, the error induced by a transfer coefficient that is too high. The combined error in $C_T$ may therefore well be close to zero.

With the model we studied the sensitivity of the mean specific mass balance of Vatnajökull to external climatic changes. There is no good network of meteorological stations around Vatnajökull and we had to force the model with data from weather stations on one side of Vatnajökull. This introduces errors in cloudiness and precipitation, which are not well known over Vatnajökull. Especially the distribution of precipitation may vary from year to year, dependent on the predominant wind direction. In spite of this, the mean specific mass balance over seven years could be simulated reasonably well. The fact that Vatnajökull shapes its own precipitation gradients results in strongly varying sensitivities to temperature changes over the ice cap. In the south and southeast, where the climate is more maritime, $C_T$ is higher than in the drier northwest. The variation of $C_T$ over Vatnajökull stresses the importance of an optimization procedure as that described in this work. Even for much smaller ice caps or glaciers, the precipitation can vary considerably irrespective of altitude, and this strongly affects the sensitivity to climate change.

**Appendix 2A: Parameterization for the global radiation**

The parameterization of the global radiation contains two factors that need to be tuned to the data: the factor for aerosol extinction $T_{as}$ and the cloudfactor $T_{cl}$. $T_{as}$ is given by

$$T_{as} = k^m \qquad 2.11$$

where m is the optical air mass and k is a constant whose value is determined by fitting equation 2.2 to the observed data for clear skies. Then, $T_{cl}$ is 1 and k is the only unknown in the parameterization. The cloud observations from U2 and R5 are used to determine when the sky was cloud-free for A1 - I6, and for R4 - R5, respectively. For other stations where global radiation has been measured (U7, U8, U9, U10 and R2) low values of $I_{in}$ can be used to identify clear skies (Bintanja and Van den Broeke, 1996). This method yields good results for station U2 and we apply it to the other stations when $I_{in}$ was low for at least several hours. The parameterization is fitted to hourly values of global radiation (Q), pressure (p), surface albedo ($\alpha$) and precipitable water in a vertical column of atmosphere (u). The last quantity is obtained from the radiosondes launched twice a day near station U2. In doing so, it is assumed that the atmospheric profiles above U2 are also valid over the rest of Vatnajökull. For all stations we find mean values of k between 0.919 and 0.968. There is no dependence on altitude or location, which justifies the assumption of a horizontally homogenous atmosphere over Vatnajökull. The mean value of all data is 0.936,

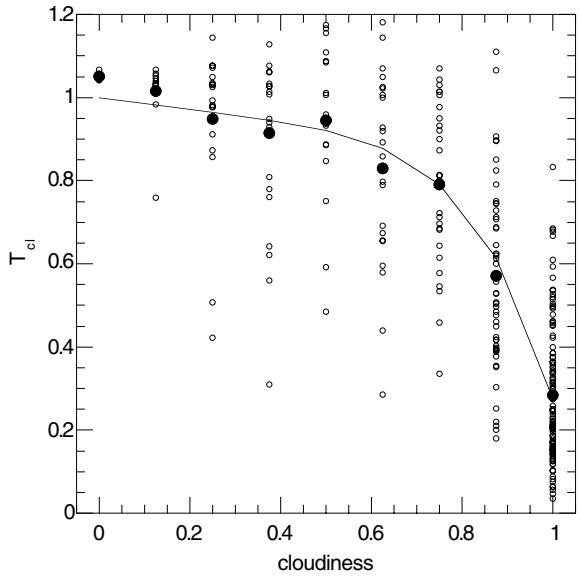


*Figure 2.11. The transmission coefficient for clouds as a function of cloudiness for station A1. Open circles are hourly means, solid circles are mean values per octa. The simulated transmission coefficient is given by the solid line.*

which compares well with the value used by Gueymard (1993) (0.94) and is slightly smaller than the value found by Greuell et al. (1997) (0.96).

Now that the coefficient for aerosol extinction is known, an expression for the cloud factor ($T_{cl}$) can be determined. This is only possible when direct observations of cloudiness are available (that is, for the stations A1 - I6 and R4 - R5). Values of $T_{cl}$ are computed from $T_{cl} = Q_{obs}/Q_{cs}$, where $Q_{obs}$ is the observed global radiation and $Q_{cs}$ is the computed clear-sky global radiation. In order to minimize errors in the observations, measurements corresponding to high solar zenith angles (>80°) were not used for this comparison. $T_{cl}$ depends on cloudiness and on the distribution of cloud types with altitude. We found that the dependence of $T_{cl}$ on altitude decreases with solar elevation, which is most likely caused by the decreasing optical depth of clouds. We therefore do not use the radio soundings (which were only used at noon and at mid-night) to determine $T_{cl}$ but calculate u from the vapor pressure measured at A1 (Smith, 1966). For all stations on Vatnajökull we observe a linear decrease of $T_{cl}$ with n for n smaller than 5/8, and a much stronger decrease of $T_{cl}$ with n for higher values of n (figure 2.11). Hence, we assume the relation between $T_{cl}$ and n to be of the form

$$T_{cl} = 1 - a\,n - b\,n^m \qquad 2.12$$

where a, b and m are constants and m is an integer. When we fit this equation to the data of each station separately we find a near-linear decrease of b with altitude. Oerlemans et al. (1999) suggested that the strong altitudinal gradient is caused by the frequent occurrence of low-level clouds with large optical thickness. There are no systematic observations of cloud type available and we can only use the altitude to describe this effect. We therefore change equation 2.12 into

$$T_{cl} = 1 - a\,n - \left(b_1 - b_2\,z\right) n^m \qquad 2.13$$

When we fit equation 2.13 to the data of all stations we find optimal values of 0.14 for a, 0.59 for $b_1$, 0.00029 for $b_2$ and 6 for m. The residual standard deviation in $T_{cl}$ for the individual observations (0.20) is quite high because the optical thickness of clouds can vary considerably. For the mean values of $T_{cl}$ per octa, equation 2.13 is much more accurate with a residual standard deviation of 0.04.

**Appendix 2B: Parameterization for the albedo**

The albedo of snow is given by:

$$\alpha'_{sn} = \alpha_f + \left(\alpha_{frsn} - \alpha_f\right)\exp\left(\frac{dn_{sn} - dn}{t^*}\right) \qquad 2.14$$

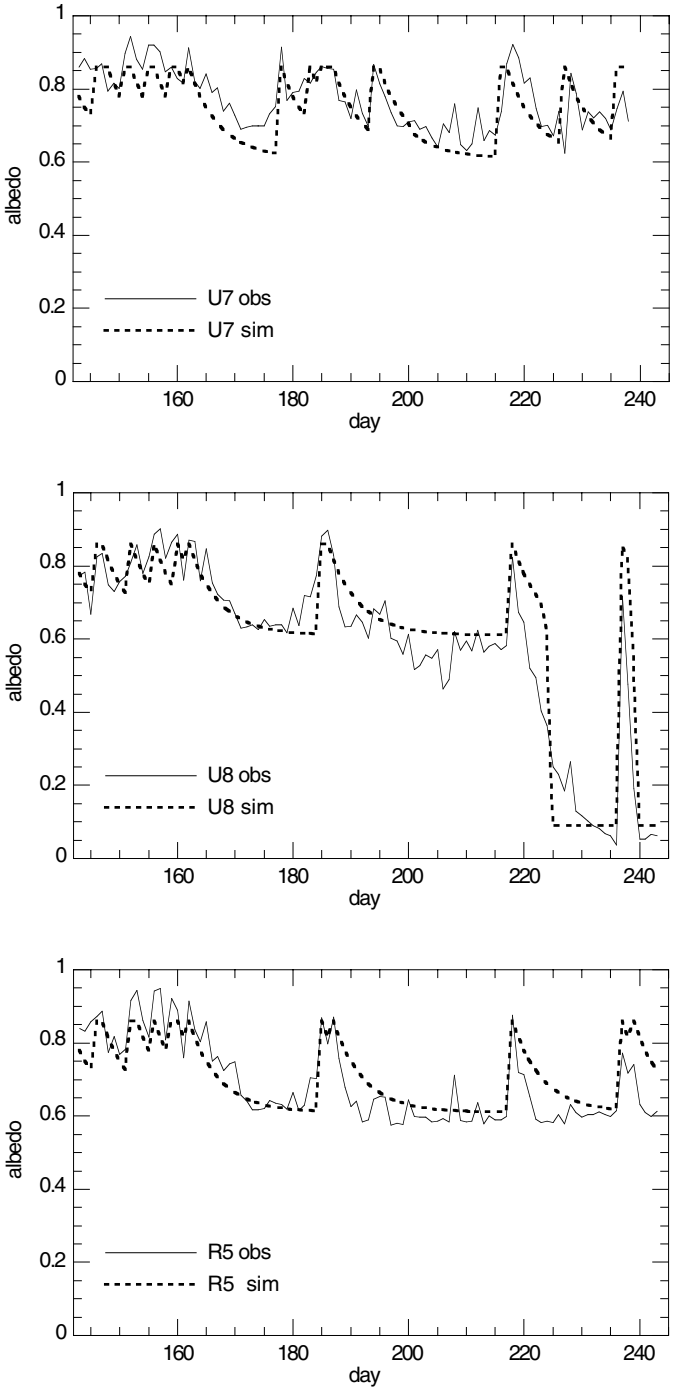


*Figure 2.12. Observed (obs) and simulated (sim) albedo as a function of time for three representative automatic weather stations.*

where $\alpha_f$ is the firn albedo, $\alpha_{frsn}$ the albedo of freshly fallen snow, dn the present day number, $dn_{sn}$ the number of the day on which the last snow fell and t* a constant that describes the speed of albedo change. The age of the snow ($dn_{sn}$-dn) primarily describes the effect of changing grain size and may include impurity content and the development of surface roughness on a small scale. Equation 2.14 contains three parameters ($\alpha_{frsn}$, $\alpha_f$ and t*) that depend on local conditions and need to be tuned to the data on albedo and surface melt. Data from the stations I6, U7, U8, R2, R4 and R5 can be used for tuning equation 2.14. Because albedo data can contain large errors when the sun is very low we use the daily albedo, which is defined as the ratio of daily amount of incoming solar radiation to daily amount of reflected solar radiation. We also use daily snowfall data. When we tune equation 2.14 by minimizing the root-mean-square difference between observed and simulated albedos, we find $\alpha_{frsn}$=0.86, $\alpha_f$=0.61 and t*=5.2 days while the r.m.s. error is 0.061. Figure 2.12 displays the observed and simulated albedos for the stations U7, U8 and R5.

When the snow disappears, a transition from $\alpha_{sn}$ to the ice albedo ($\alpha_{ice}$) occurs. Following Oerlemans and Knap (1998) we have

$$\alpha = \alpha_{sn} + \left(\alpha_{ice} - \alpha_{sn}\right)\exp\left(-d/d^*\right) \qquad 2.15$$

where d is the snow depth and d* a scaling constant. When we tuned this equation to the snow depth data (only available for stations U8 and U9) we found large values for d* (8 and 15 cm, respectively). A reason might be that the radiation sensors that we used receive 90% of the reflected radiation from a circle with a radius of 4.5 m. And because the snow line often is not sharp but consists
of patches of snow and ice, ice patches may have influenced the recorded albedo when there was still snow directly underneath the sensors. The dark tephra that covers the ice at U8 and U9 possibly strengthens this effect. We therefore use the value of Oerlemans and Knap (1998), 3.2 cm.

**Appendix 2C: Parameterization for the incoming longwave radiation**

The incoming longwave radiation is given by:

$$I_{in} = \left[\varepsilon_{cs}\left(1-n^p\right) + \varepsilon_{oc} n^p\right] f_s \sigma T_{atm}^4 + L_{sl} \qquad 2.16$$

where $\varepsilon_{cs}$ is the emissivity of a clear sky, n the cloudiness, p a constant (only integers are allowed), $\varepsilon_{oc}$ the emissivity of clouds, $\sigma$ the Stefan-Bolzmann constant, $L_{sl}$ the longwave radiation received from the surrounding upper-hemisphere slopes and $f_s$ a constant that is estimated from the DEM for each measurement site. The emissivity of a clear sky is written as

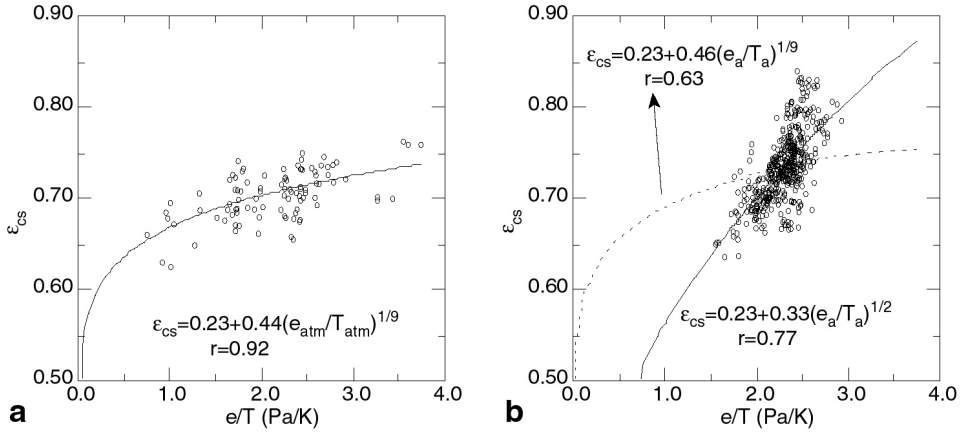


*Figure 2.13. Clear-sky emissivity as a function of e/T. In plot a , e and T of the free atmosphere are used, which are available twice for each day. In plot b, hourly values of e and T at screen-height (2 m) are used. In both plots fits of equation 2.17 to the data are shown (solid lines), and in plot b a fit of equation 2.17 with a theoretical acceptable value of 9 for m is also shown (dotted line).*

$$\varepsilon_{cs} = 0.23 + b\left(e_{atm} / T_{atm}\right)^{1/m} \qquad 2.17$$

where b and m are constants. The integer m is theoretically expected to be not smaller than 7 (Konzelmann et al., 1994). For all stations $T_{atm}$ and $e_{atm}$ are obtained from the radio soundings that were made twice a day near station U2. By doing so we assume that the atmospheric profiles above U2 are also valid for the rest of Vatnajökull. Clouds are detected in the same way as described in appendix 2A. The parameterization contains four constants (b, m, $\varepsilon_{oc}$ and p) that need to be tuned to the data. First, b and m are determined by fitting the parameterization to the clear-sky (n=0) measurements of $I_{in}$. We use the hourly mean values of $I_{in}$ that are closest in time to the radio soundings. For all stations we find comparable values of b and m, with mean values of 0.438 and 9, respectively (figure 2.13a). This shows that the assumption of a horizontally homogeneous atmosphere is correct. The residual standard deviation for $\varepsilon_{cs}$ is 0.022. The value of b compares well with those found by Konzelmann et al. (1994), 0.443, and by Greuell et al. (1997), 0.475 and 0.407.

The value of m is, as theoretically expected, larger than 7. Konzelmann et al. (1994), who used $T_a$ and $e_a$ and not $T_{atm}$ and $e_{atm}$ in their calculations, found a value of 8 for a location near the equilibrium line of the Greenland icesheet. There, $T_a$ and $e_a$ obviously describe the state of that part of the boundary-layer that generates $I_{in}$. The Greenland ice sheet is so large that advection of relatively warm air from ice free areas does not affect $I_{in}$. Greuell et al. (1997) also used $T_a$ and $e_a$ and found that a value of 8for m is suitable for a site high in the accumulation area of the Pasterze (Austria). On the tongue of that glacier, however, it was not and they noted that this was presumably caused by the shallow katabatic layer over the tongue. We find the same for Vatnajökull when $T_a$ and $e_a$ are used in the equations 2.16 and 2.17 in stead of $T_{atm}$ and $e_{atm}$ (figure 2.13b). We then find a value

of 2 for m (with a residual standard deviation for $\varepsilon_{cs}$ of 0.028), which is not acceptable from a theoretical point of view (Konzelmann et al., 1994). However, in this case a more realistic value of 9 correspond less well to the data (residual standard deviation for $\varepsilon_{cs}$ is 0.035). This means that the katabatic layer over Vatnajökull is generally not thick enough to influence $I_{in}$ and that relatively warm air above the katabatic layer plays a larger role.

When an expression for $\varepsilon_{cs}$ is available, $\varepsilon_{oc}$ can be determined by fitting the parameterization to data that were measured when the sky was entirely overcast (n=1). Values found for $\varepsilon_{oc}$ are displayed in table 2.6. There appears to be no variation with altitude and the mean value of 0.952 is used henceforth. This value is in line with those found by Konzelmann et al. (1994), 0.952, and by Greuell et al. (1997), 0.976. Next, p is determined from the data for which 0<n<1 (for n=0 and n=1, p has no influence). For all stations the same value is found, namely 3, except for R5 where it has a value of 4. For this station, however, only few data are available. We therefore use a value of 3 throughout.

| Station | n=1 | | 0<n<1 | |
|---|---|---|---|---|
| | data | <$\varepsilon_{oc}$> | data | <p> |
| U2 | 28 | 0.958 | 46 | 3 |
| A4 | 28 | 0.951 | 49 | 3 |
| A5 | 27 | 0.945 | 48 | 3 |
| I6 | 28 | 0.955 | 49 | 3 |
| R5 | 3 | 0.937 | 10 | 4 |
| All five stations | 114 | 0.952 | 192 | 3 |
| Greenland | | 0.952 | | 4 |
| Pasterze | | 0.976 | | 2 |

*Table 2.6. Values of $\varepsilon_{oc}$ and p for several sites on Vatnajökull and from other studies. Greenland data are from Konzelmann et al. (1994), Pasterze data from Greuell et al. (1997).*

# 3 Reconstruction of the mean specific mass balance of Vatnajökull with a Seasonal Sensitivity Characteristic*

**Abstract**

We present a Seasonal Sensitivity Characteristic (SSC) of Vatnajökull (Iceland), which consists of the sensitivity of the mean specific mass balance to monthly perturbations in temperature and precipitation. The climate in Iceland is predominantly maritime (high precipitation) although often polar air mass influence the area. This results in temperature sensitivities that are high in summer and nearly zero during the winter months. In contrast, precipitation sensitivities are high in winter and low in summer. We use the SSC of Vatnajökull as a reduced mass balance model, with which we reconstruct the mass balance of Vatnajökull since 1825. The reduced model shows that changes in temperature and precipitation like the ones observed both have a significant impact upon the mass balance. The reconstructed mass balance records for two Icelandic glaciers correlate very well with mass balance records that are extracted from length records with a linear inverse model. This places confidence in both the reduced (forward) mass balance model and in the inverse model, although the forward method produces larger mass balance variations than the inverse method. For the south of Vatnajökull we find that after 1900, the length record is well explained by temperature variations alone, while another Icelandic glacier (Sólheimajökull) was also influenced by precipitation variations.

## 3.1 Introduction

The record of glacier length variations is interesting for two reasons. Inverse modeling of glacier length can provide information about climatic variations in the past (e.g. Nye, 1965; Smith and Budd, 1979; Oerlemans, 1997) and, if climatic records are available, it can help us to understand and predict the response of glaciers and ice caps to climatic change. Glacier fluctuations depend upon the mass balance, but the first regular mass balance measurements were only started in the 1940s and 1950s (e.g. Hoinkes and Steinacker,

* Based on: De Ruyter de Wildt, M. S., E. J. Klok and J. Oerlemans. Reconstruction of the mean specific mass balance of Vatnajökull with a Seasonal Sensitivity Characteristic. *Geografiska Annaler*, in press.

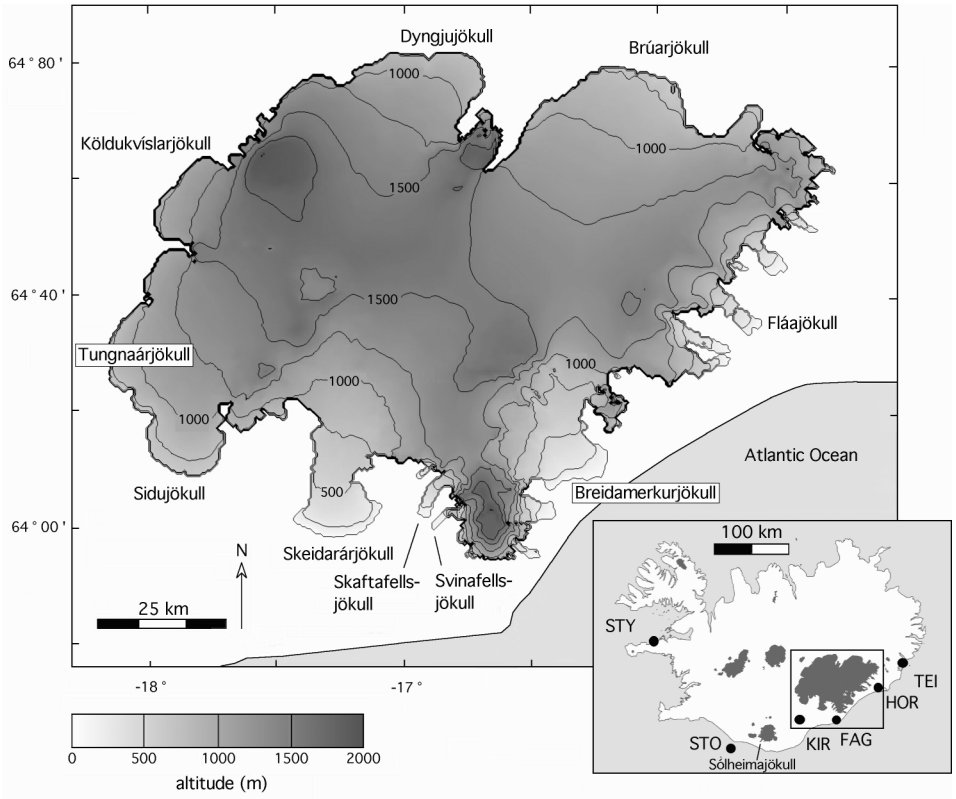


*Figure 3.1. Map of Vatnajökull. Indicated are height-contours for each 250 m interval, the major drainage basins and some smaller outlet glaciers. The small map of Iceland shows the location of Vatnajökull and the weather stations in Kirkjubæjarklaustur (KIR), Fagurhólsmyri (FAG), Hornafjördur (HOR), Stykkishólmur (STY), Stórhöfdi (STO) and Teigarhorn (TEI).*

1975; Holmlund et al., 1996). Many authors have therefore searched for empirical relations between mass balance and meteorological variables for specific glaciers (e.g. Lliboutry, 1974; Hoinkes and Steinacker, 1975; Günther and Widlewski, 1986; Greuell, 1992) in order to extrapolate the mass balance record into the past. Others took a theoretical approach and employed models to reconstruct mass balance records (e.g. Oerlemans, 1992; Schmeits and Oerlemans, 1997).

In this paper, we study the sensitivity to climate change and reconstruct the mass balance of Vatnajökull (Iceland). With a surface area of 8200 km$^2$, Vatnajökull is one of the world's largest temperate ice caps. It consists of a large and flat accumulation area, several large lobate outlet glaciers, most of which exhibit surging behavior, and many smaller valley glaciers (figure 3.1). Since the end of the 19$^{th}$ century it has been the subject of many glaciological studies (Williams et al. (1997) and Björnsson et al. (1998a) give overviews of previous work). However, only since 1992 has the mass balance been systematically and continuously monitored (Björnsson et al., 1998a), while the sensitivity of the mass balance

of Vatnajökull to climate change has not been studied. Only recently a mass balance model of Vatnajökull has been constructed which was used for some sensitivity experiments (De Ruyter de Wildt et al., 2002a). In this paper we study the sensitivity of the mass balance of Vatnajökull more specifically. We present a Seasonal Sensitivity Characteristic (SSC) of Vatnajökull, which consists of the sensitivities of the mean specific mass balance of a glacier to monthly temperature and precipitation perturbations. It can be used as a simplified but accurate mass balance model by multiplying it with monthly perturbations in temperature and precipitation (Oerlemans and Reichert, 2000, O-R hereafter). With this reduced model, the mass balance is easily reconstructed from long meteorological records, which often consist of monthly values. We use the SSC to reconstruct the mass balance variations of Vatnajökull over the past 180 years, which includes the end of the little ice age, and discuss the relation between the reconstructed mass balance record and length changes of some outlet glaciers. The length changes are related to mass balance changes with a linear response model, which has been successfully applied to various glaciers around the world (Klok and Oerlemans, 2002).

### 3.2 Seasonal Sensitivity Characteristic

The surface mass balance of a glacier is influenced by several meteorological variables, but most of all by temperature and precipitation. Empirical relations between the mean specific mass balance ($B_m$) and these meteorological variables are generally linear, but different authors often use different predictors (e.g. temperature in a certain month, precipitation in the winter months or sum of positive degree days). In order to obtain more structure in the relation between mass balance and climate, O-R defined a Seasonal Sensitivity Characteristic (SSC). The SSC is a 2 by 12 matrix that contains the sensitivity of $B_m$ to monthly perturbations in temperature (T) and (P). These sensitivities, $C_{T,k}$ and $C_{P,k}$, are defined as:

$$C_{T,k} = \frac{\partial B_m}{\partial T_k} = \frac{B_m(T_{ref,k} + \Delta T) - B_m(T_{ref,k} - \Delta T)}{2\ \Delta T} \qquad 3.1$$

and

$$C_{P,k} = \frac{\partial B_m}{\partial P_k} = \frac{B_m(P_{ref,k} + \Delta P) - B_m(P_{ref,k} - \Delta P)}{2\ \Delta P} \qquad 3.2$$

where k is the month and the perturbations $\Delta T$ and $\Delta P$ are 1 K and 10%, respectively. $C_{T,k}$ and $C_{P,k}$ can be obtained by computing $B_m$ from a run of a mass balance model during which T and P are perturbed in month k. With these definitions, $B_m$ is easily computed from monthly perturbations in T and P:

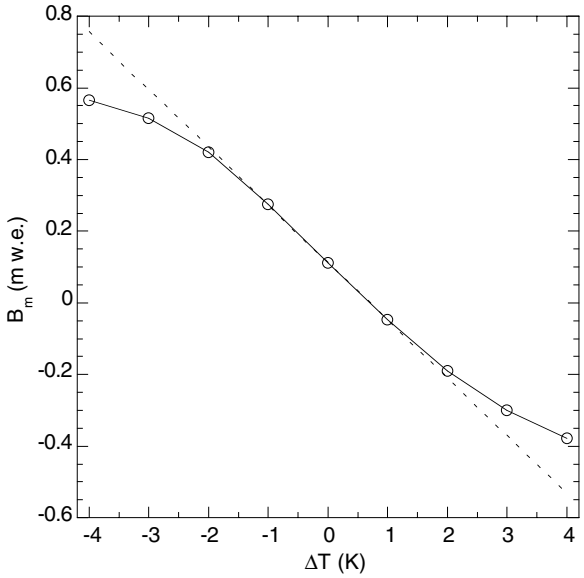


*Figure 3.2. Change in mean specific mass balance of the north-western part of Vatnajökull (the drainage basins of Tungnaárjökull, Köldukvíslarjökull, Dyngjujökull and Brúarjökull) as a function of July temperature perturbation. The dashed line defines* $C_{T,7}$ *, derived from* $B_m(T_{ref,7}+1K)$ *and* $B_m(T_{ref,7}-1K)$.

$$B_m = B_{m,ref} + \sum_{k=1}^{12}\left[C_{T,k}(T_k - T_{ref,k}) + C_{P,k}(P_k - P_{ref,k})/P_{ref,k}\right] \qquad 3.3$$

where $B_{m,ref}$ is the mean specific mass balance when T and P are not perturbed (i.e. the mean specific mass balance for the average climate). Apart from temperature and precipitation perturbations we also considered perturbations in cloudiness, but these appeared hardly to influence the mean specific mass balance. Equation 3.3 can be considered as a linearisation of a more general expression that also contains higher-order terms. These higher order terms represent non-linear effects and cross-terms (a monthly perturbation in one year influences the mass balance in a later year). O-R found that higher-order terms and cross-terms are not very important for Nigardsbreen in Norway. Figure 3.2 shows for temperature deviations between -2 K and +2 K the assumption of linearity is correct for Vatnajökull. For lower temperatures $\partial B_m/\partial T$ grows increasingly smaller and eventually becomes zero, because then no melt occurs at all (for example, this is the current situation for much of Antarctica). For very high temperatures $\partial B_m/\partial T$ also goes to zero, because then all precipitation falls as rain, even when it gets slightly colder. For deviations in July temperature between -2 K and +2 K the error resulting from using equation 3.1 is negligible. Temperature deviations that are larger than 2 K can of course occur, but not very often: the standard deviation for July temperatures in Kirkjubæjarklaustur is 0.6 K. For January precipitation, $\partial B_m/\partial P$ is linear for precipitation perturbations between -80% and 80%. The

effect of cross-terms is more difficult to quantify and will be discussed below.

To construct an SSC for Vatnajökull we use the mass balance model of De Ruyter de Wildt et al. (2002a), which was especially constructed for Vatnajökull. It describes the energy fluxes between atmosphere and glacier, which are tuned with *in situ* measured data (Oerlemans et al., 1999), in a detailed way. The most important model specifications are:

- Temperature in the katabatic surface layer is related, but not equal, to temperature in the free atmosphere just above the surface layer (in the surface layer temperature is mostly lower and temperature variations are smaller than in the free atmosphere).
- Incoming longwave radiation is a function of temperature in the free atmosphere, a result of the relatively thin katabatic layer over Vatnajökull.
- Sensible heat flux is a function of temperature in the katabatic layer.
- Snow albedo depends upon the number of days since the last snowfall
- Ice albedo depends upon location and varies from very low in the northwest, 0.10 due to volcanic ash layers, to 0.30 at some locations in the south and southeast.
- Sub-surface processes like refreezing of meltwater are neglected and whenever the surface energy flux is positive, the surface is assumed to be at the melting point ("zero-degree assumption"). For a temperate ice cap like Vatnajökull this is a reasonable assumption.
- Free-air temperature and vapor pressure are assumed to be always horizontally (but not vertically) homogeneous over the ice cap. Measurements of temperature and of incoming radiation, which depends upon atmospheric temperature and humidity, showed that this is mostly the case (De Ruyter de Wildt et al., 2002a). Because synoptic weather stations are only located to the south and south-east of Vatnajökull (figure 3.1), cloudiness and relative variations in precipitation are also assumed to be horizontally homogeneous. Hence, the energy balance over the entire ice cap can be obtained from the available meteorological data.
- The mean spatial distribution of precipitation over Vatnajökull is not well known, which is why we use this variable to calibrate the model to observations of the mass balance (Björnsson et al., 1997, 1998a, b, c, 1999). These observations were mainly made over the central and north-western parts of the icecap (i.e. the drainage basins of Tungnaárjökull, Köldukvíslarjökull, Dyngjujökull and Brúarjökull). In the south and southeast precipitation data from synoptic weather stations are available to prescribe a spatial distribution.

Daily values of temperature, vapor pressure and cloudiness measured in Kirkjubæjarklaustur (figure 3.1) since 1965, are used to drive the model (De Ruyter de Wildt et al., 2002a). However, care must be taken in using precipitation records to drive the model, because the spatial distribution of this quantity varies from year to year. It was found that the observed mass balance is best simulated when the model is driven with the precipitation from Fagurhólsmyri (figure 3.1). Observed and modeled values of $B_m$ for the northern and western drainage basins are shown in figure 3.3.

The SSC is obtained by imposing temperature perturbations of 1K and precipitation perturbations of 10%, which is done separately for each month. Note that temperature is perturbed at unperturbed precipitation, and vice versa, so any natural correlations of T and

P are not included. Each time, the model is run from 1965 to 1999 and the sensitivities are then averaged over the years. We reconstruct $B_m$ with the resulting SSC and equation 3.3, using monthly temperature from Kirkjubæjarklaustur and monthly precipitation from Fagurhólsmyri. The results compare well with $B_m$ from the full model (figure 3.3). In the first year (1966) there is a large difference in $B_m$ because in the full model, a snow cover that is in balance with the climate has yet to be formed. Furthermore, in 1997 summer melt was significantly enhanced by ash that was deposited on the icecap after a volcanic eruption in November 1996 (H. Björnsson, personal communication, and De Ruyter de Wildt et al., 2002a). This significantly lowered the albedo, which is accounted for in the full mass balance model but not in the reduced model. The good correlation (r=0.97 for all years except 1966 and 1997) and confirms the conclusion of O-R that higher order terms are not very important.

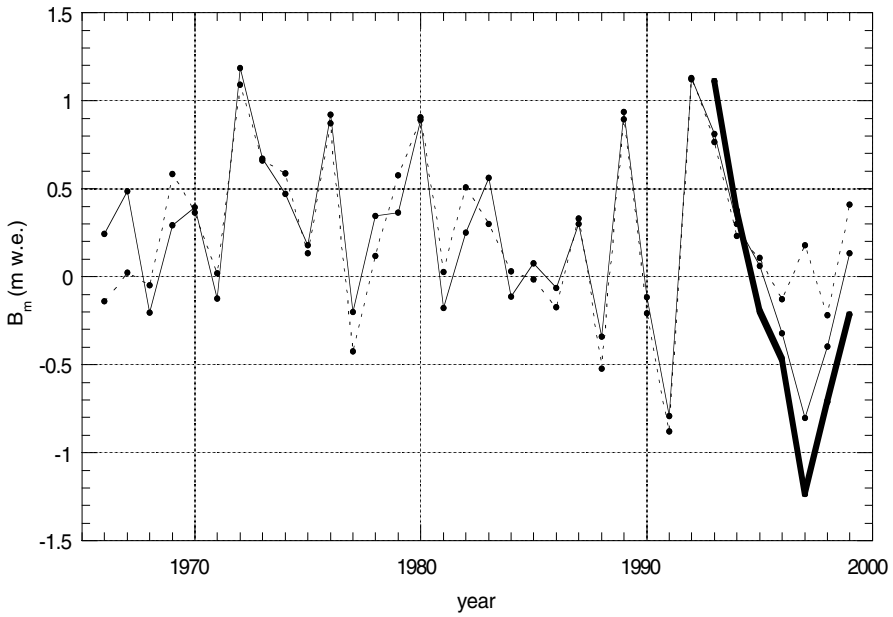


*Figure 3.3. Observed mean specific mass balance ($B_{m,obs}$), reconstructed mean specific mass balance from the full mass balance model ($B_{m,mod}$) and reconstructed mean specific mass balance from the reduced model ($B_{m,red}$). All are given for the area where the mass balance has been measured regularly, i.e. the drainage basins of Tungnaárjökull, Köldukvíslarjökull, Dyngjujökull and Brúarjökull.*

### 3.3 The SSC of Vatnajökull and some of its drainage basins

Figure 3.4 shows the SSC for some drainage basins of Vatnajökull and for the whole of Vatnajökull. For comparison it also shows the SSC for two other glaciers, namely Hintereisferner in Austria and White Glacier in the Canadian Arctic (O-R). For all parts of Vatnajö-

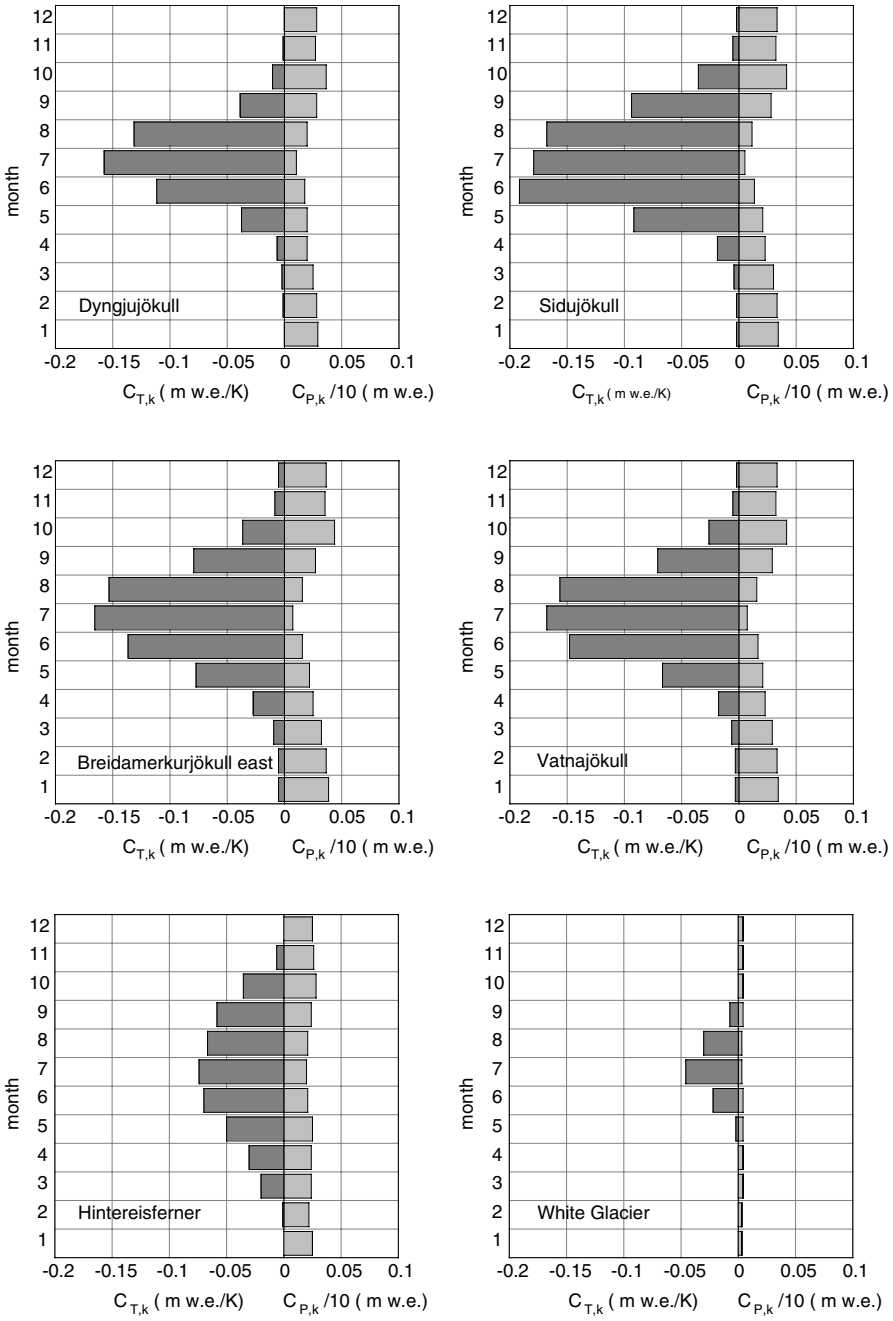


*Figure 3.4. SSC's for the drainage basins Dyngjujökull, Sidujökull and Breidamerkurjökull, and for the whole of Vatnajökull, for Hintereisferner (Austria) and for White Glacier (Canadian Arctic). The plots for Hintereisferner and White Glacier are from Oerlemans and Reichert (2000).*

kull, changes in precipitation are most important in winter. There are two reasons for this: first, in the summer much precipitation falls as rain, and second, precipitation is higher in the winter months than in the summer months (table 3.1). Temperature sensitivity is nearly zero from November-March, and temperature changes influence the mass balance most in the three summer months June-August. This is typical for glaciers in a moderately wet or even dry climate (O-R). During the months November-March Iceland is influenced by polar air masses and mean temperatures at sea-level are close to the freezing-point (table 3.1). During this period nearly all precipitation falls as snow and very little melting occurs, so temperature changes hardly affect the mass balance. Compared to other glaciers, Vatnajökull has a large difference between summer and winter values of $C_T$. The consequences of these findings for $B_m$ are illustrated by figure 3.5 which shows the influence of monthly deviations in temperature and precipitation upon $B_m$. The mass balance year 1990/1991 was warm in most months, but only in the summer months (May-September) this influenced the mass balance. Especially in June and July the contribution to $B_m$ was strongly negative, leading to the second most negative annual mass balance of the last decades. Precipitation deviations were important for $B_m$ in all seasons and also produced a negative net contribution to $B_m$. During the mass balance year 1991/1992, temperatures also influenced $B_m$ only in the summer months, but now in a positive way. Contributions of precipitation deviations were mainly positive and primarily contributed to $B_m$ in September and in the winter.

Because of its size and height, Vatnajökull acts as a topographic barrier to the prevailing southerly and easterly winds, which causes the precipitation to decrease towards the northwest. Table 3.1 shows that, despite the higher mean elevations, mean annual precipitation in the northwest (e.g. Köldukvíslarjökull) is much lower than in the south and southeast (e.g. Fláajökull). The highest precipitation is found for Svinafellsjökull. This relatively small glacier flows down from Öræfajökull, the highest summit and wettest place in Iceland. At 1820 m, close to the top, annual precipitation is almost 8 m (Gudmundsson, 2000). Note that in the south and south east, where precipitation is highest, the glaciers

| Month | Temperature (°C) | Precipitation (m) |
|---|---|---|
| 1 | -0.4 | 0.150 |
| 2 | -0.4 | 0.144 |
| 3 | 0.5 | 0.128 |
| 4 | 3.0 | 0.102 |
| 5 | 6.5 | 0.106 |
| 6 | 9.4 | 0.115 |
| 7 | 11.3 | 0.102 |
| 8 | 10.6 | 0.153 |
| 9 | 7.4 | 0.145 |
| 10 | 4.8 | 0.166 |
| 11 | 1.2 | 0.142 |
| 12 | -0.3 | 0.148 |

*Table 3.1. Mean monthly reference temperature and precipitation. Temperature is from Kirkjubæjarklaustur and precipitation is from Fagurhólsmyri. Both columns give mean values for the period 1965-1999.*

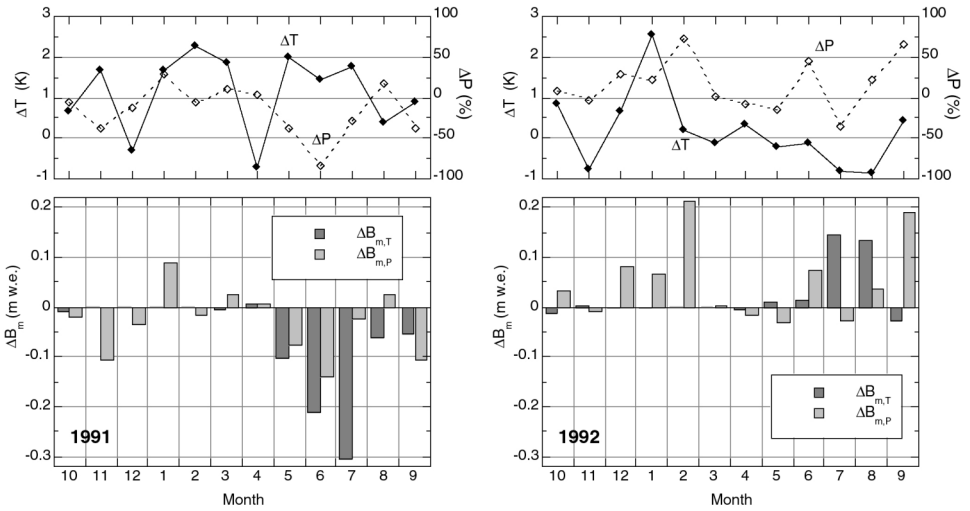


*Figure 3.5. Monthly temperature deviation (dT), monthly precipitation deviation (dP) and their respective contributions to the annual mean specific mass balance for the mass balance years 1990/1991 (left) and 1991/1992 (right). The mass balance deviations are shown for the north-western part of Vatnajökull, i.e. the drainage basins of Tungnaárjökull, Köldukvíslarjökull, Dyngjujökull and Brúarjökull.*

reach the lowest elevations. In the north and west the land surface and hence the glacier termini are higher.

Dyngjujökull lies in the northwest of Vatnajökull where precipitation is lowest. The influence of temperature variations upon the mass balance through the amount of summer snowfall is therefore relatively small for this drainage basin. Consequently, Dyngjujökull displays the lowest summer-time temperature sensitivities (although these are still high compared on a world-scale; figure 3.4). In the winter the amount of precipitation does not influence $C_T$ because then nearly all precipitation falls as snow. For Dyngjujökull, which has a high overall elevation, this implies a zero-sensitivity to temperature perturbations in the winter months. Figure *3.6*a shows that for this drainage basin, the altitudinal distribution of the annual values of $C_T$ has a maximum near the equilibrium line altitude (ELA, obtained from the full mass balance model). This is due to the albedo-feedback: as soon as ice appears at the surface, melt is strongly enhanced, and near the ELA it depends upon the temperature whether ice emerges. The ice albedo in the ablation area is very low (about 0.1) due to volcanic ash at the ice surface, which contrasts strongly to the albedo of snow. The ice of Sidujökull and Breidamerkurjökull is much cleaner and has higher albedos (about 0.25), which implies that the contrast with the albedo of snow is much less. Because of this there is no maximum in $C_T$ for these two drainage basins (figure *3.6*b and c). Note that due to the higher precipitation, $C_T$ is higher for the lowest parts of these two drainage basins than it is for the lowest part of Dyngjujökull. At elevations above the ELA ice never appears at the surface and the altitudinal distribution of $C_T$ is mainly controlled by temperature.

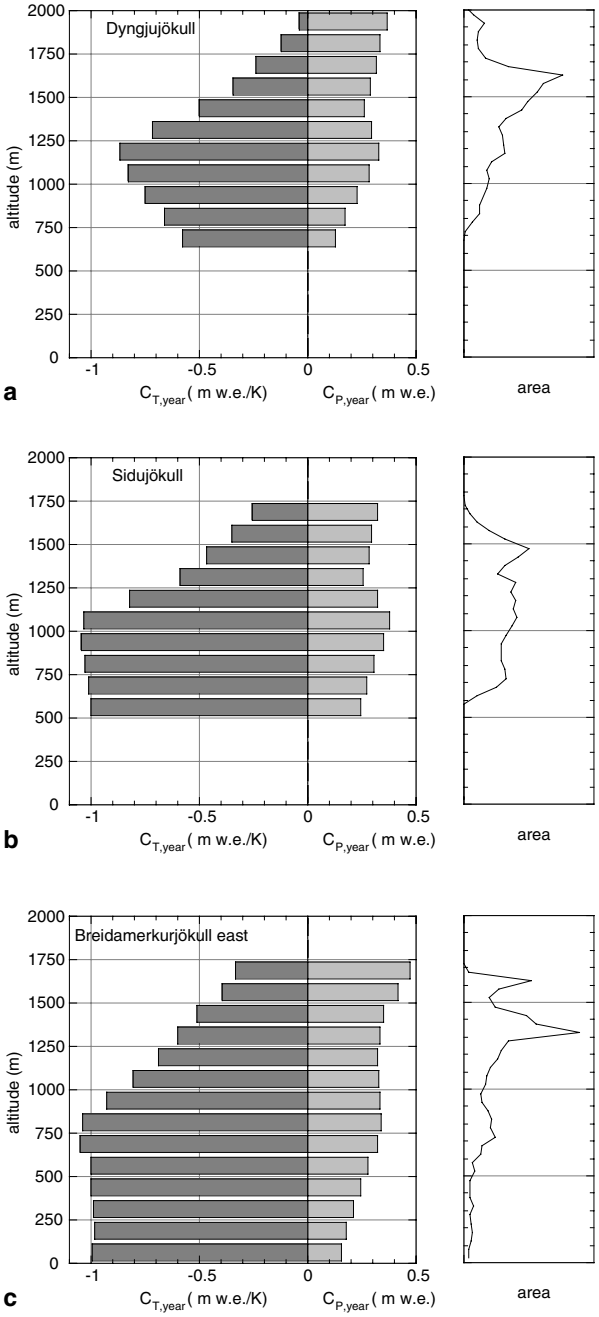


*Figure 3.6. Annual sensitivity of the mean specific mass balance to a temperature increase of 1K and to a precipitation increase of 10%, as a function of altitude. Shown are average sensitivities per 125 m interval. Sensitivities are shown for Dyngjujökull (a), for Sidujökull (b) and for Breidamerkurjökull (c). For each drainage basin the normalized hypsometry is also shown.*

Sidujökull displays very high temperature sensitivities in the summer months (figure 3.4), which is due to its hypsometry. The lower part of the drainage basin, where $C_T$ is highest, constitutes the largest part of the drainage basin (figure *3.6*b). Breidamerkurjökull displays similar high values of $C_T$ in its ablation area, but here the ablation area is relatively smaller (figure 3.6c). Breidamerkurjökull therefore has lower summer values of $C_T$ than Sidujökull (figure 3.4). On the other hand, Breidamerkurjökull extents to lower altitudes than Dyngjujökull and Sidujökull, and even in the winter it is slightly sensitive to temperature changes.

### 3.4 Meteorological data

The longest temperature record in Iceland goes back to 1823 and was measured in Stykkishólmur, approximately 300 km from Kirkjubæjarklaustur (figure 3.1). Another instrumental record was started in 1873 in Teigarhorn (figure 3.1). The large distances should not pose a problem, as temperature variations are fairly uniform over Iceland (Einarsson, 1991). The records from Stykkishólmur (figure 3.7a) and Teigarhorn (figure 3.7b), are not exactly the same (r=0.93 for mean winter (October-April) temperatures and r=0.78 for mean summer (May-September) temperatures), but they do display the same trends. Vatnajökull lies between these two stations, so we use the average of the two records (figure 3.7c) to force the reduced mass balance model.

Precipitation variations are not as uniform over Iceland as temperature variations (Jóhannesson and Sigurdsson, 1998). As an example we show the longest precipitation records, which were measured in Stykkishólmur since 1857 (figure 3.8a) and in Stórhöfdi since 1890 (figure 3.8b). Figure 3.8c displays the data from Kirkjubæjarklaustur. Note that the three plots have different vertical scales. The records display large decadal-scale variations but these are different for the three sites. Monthly precipitation from Stykkishólmur and Stórhöfdi correlates only weakly with the data from Kirkjubæjarklaustur (r=0.65 and r=0.49) while yearly data are not correlated at all over the 34-year period (1966-1999). A possible explanation for the differences in precipitation is the orography, including the large ice caps, causing the distribution of precipitation to depend strongly upon the predominant atmospheric circulation in a specific year. So in contrast to temperature variations, precipitation variations are not uniform over Iceland, which makes it difficult to find appropriate long-term precipitation records that can be used for mass balance reconstruction.

### 3.5 Mass balance reconstruction 1823-present

The relative importance of temperature and precipitation perturbations can be visualized by applying equation 3.3 with either $C_{T,k}=0$ or $C_{P,k}=0$, respectively. The results are shown in figure 3.9 (note that $B_m = B_{m,w} + B_{m,s}$). Also note that the ice cap responds to changes in

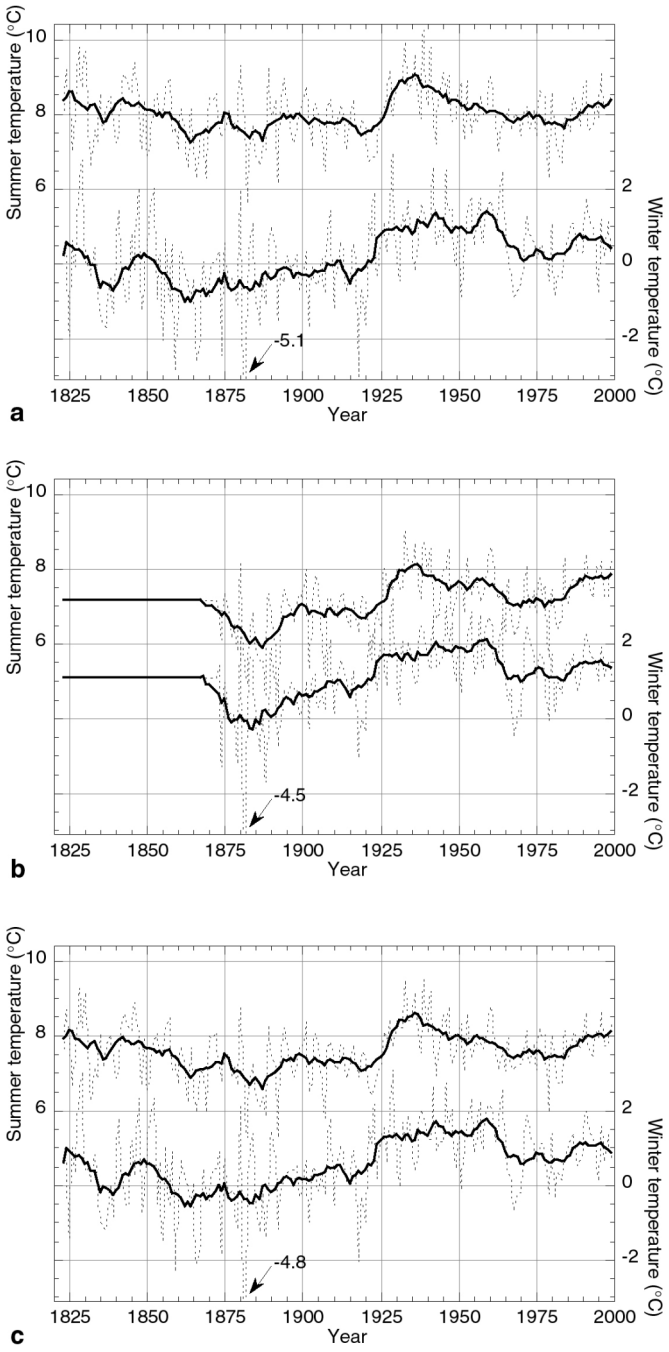


*Figure 3.7. Winter (October-April) and summer (May-September) temperature in Stykkishólmur (a), in Teigarhorn (b) and averaged over both places (c). The average temperature before 1873 is extrapolated from the Stykkishólmur data with the linear relation between the data from Stykkishólmur and from Teigarhorn. The thick solid lines indicate 11-year running means.*

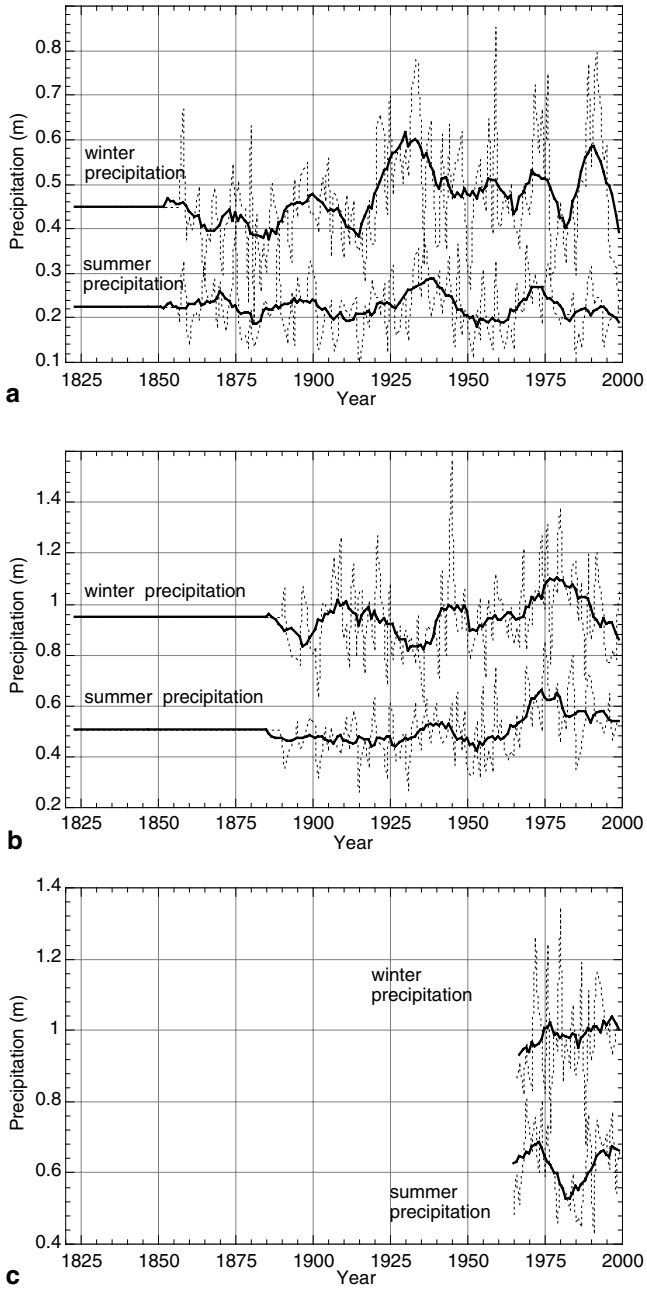


*Figure 3.8. Winter (October-April) and summer (May-September) precipitation in Stykkishólmur (a), in Stórhöfdi (b) and averaged in Fagurhólsmyri and in (c). The thick solid lines indicate 11-year running means. Note the different vertical scales.*

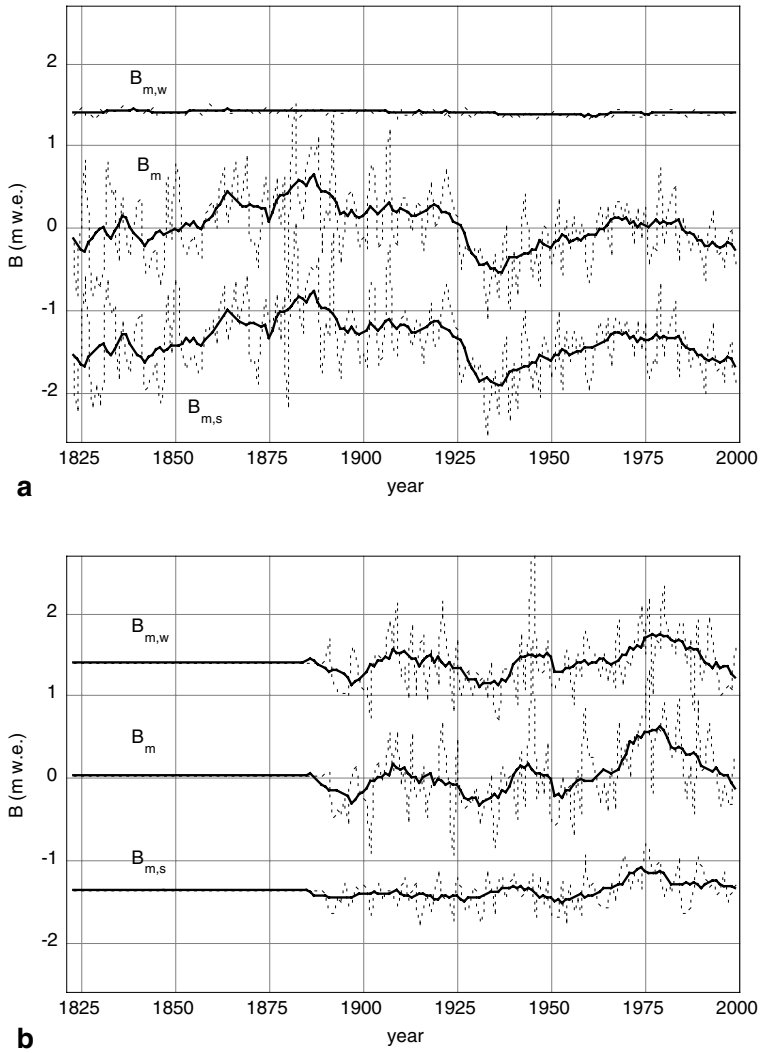


*Figure 3.9. Mean specific mass balance of Vatnajökull, reconstructed with the reduced mass balance model. The reduced model was forced only with monthly temperatures from Stykkishólmur and Teigarhorn (a) and only with monthly precipitation from Stórhöfdi (b). Shown are the winter (October-April) mass balance ($B_{m,w}$), the summer (May-September) mass balance ($B_{m,s}$) and the annual mass balance ($B_m$). The thick solid lines indicate 11-year running means.*

mean specific mass balance by changing its areal extent in such a way that the mean specific mass balance returns to zero. Consequently, equation 3.3 does not give the actual mean specific mass balance but rather changes in mass balance that result from changes in climate. Not surprisingly, temperature fluctuations only affect the mass balance in the summer months (figure 3.9a). The curve for the annual $B_m$ in this figure therefore nearly equals the curve for the summer $B_m$ and these curves closely mirror the summer tempera-

ture (figure 3.9a). There are large interannual variations, but variability on a decadal time scale is much smaller. In the 1920s there is a strong increase (about 1.5 K) in summer temperature resulting to a drop of about 0.9 m w.e. in summer and annual $B_m$. This transition marks the end of the little ice age in Iceland. Many other places near the Arctic fringe experienced a similar strong warming when compared to more temperate locations, owing to the northward displacement of continuing snow and ice cover (Lamb, 1995). Later the Icelandic summers became gradually cooler. The results for the 1990s correspond to observations of positive values of $B_m$ in the early 1990s and negative values in the late 1990s (Björnsson et al., 1997, 1998a, b, c, 1999).

Precipitation changes were different at different sites (figure 3.8), which is why it is less straightforward to reconstruct the influence of precipitation. For example, the record from Stykkishólmur displays a strong increase in precipitation in the 1920s, but the record from Stórhöfdi displays a decrease during the same period. Figure 3.9b shows that when precipitation values from Stórhöfdi (where mean precipitation is nearly the same as in Kirkjubæjarklaustur) are used, the resulting mass balance changes are of the same order of magnitude as those resulting from temperature changes (note that the annual curve in figure 3.9b closely resembles the winter precipitation record in figure 3.8b). However, there is no way of telling which location (Stykkishólmur, Stórhöfdi, or any other) is more appropriate.

### *3.5.1 Relation between mass balance and terminus position*

It may therefore be useful to see if glacier length records contain any additional information about the past climate. Just as many glaciers world-wide (e.g. Grove, 1988), many Icelandic glaciers reached their largest extend in historical times in the middle of the 19$^{th}$ century, after which they strongly retreated (Thorarinsson, 1943). The non-surging outlet glaciers of Vatnajökull receded very slowly after 1850 and advanced slightly in the 1880s, but since 1890 they too retreated strongly (figure 3.10). This agrees with the summer temperature record which displays a decrease between 1875 and 1885 and an increase between 1885 and 1895 (figure 3.7a). Sigurdsson and Jónsson (1995) found a similar small lag of five to ten years between the step-like warming around 1925 and the onset of rapid retreat throughout Iceland in the 1930s (compare figure 3.10 with figure 3.9a). Their conclusion was that since 1930, changes in length of non-surging Icelandic glaciers are mainly correlated to temperature changes.

The length of a glacier mainly depends upon two processes. Mass is removed from the glacier front by melting, so the frontal position reacts quickly to temperature changes. Mass gain at the front is mainly due to mass flow from higher elevations, while accumulation at the front is less important. Figure *3.6* shows that in the lower ablation area, precipitation changes are much less important than temperature changes. This is the case for the relatively dry drainage basin Dyngjujökull which is situated at higher elevations (figure *3.6*a), for Sidujökull which has a lower elevation but receives more precipitation (figure *3.6*b) and also for Breidamerkurjökull which also receives much precipitation and almost reaches sea level (figure *3.6*c). Mass flow towards the front depends with a time lag upon mass build-up at higher elevations. At higher elevations, both temperature and

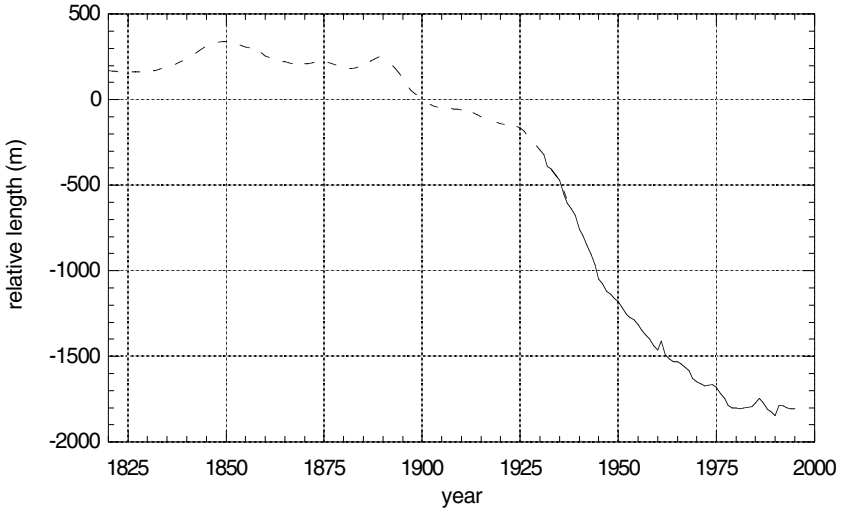


*Figure 3.10. Average length change of eight southern and southeastern outlet glaciers of Vatnajökull, relative to the situation in 1900. Changes before 1933 (dashed line) are taken from Thorarinsson (1943) and changes since 1933 (solid line) are compiled after data from Sigurdsson (1998).*

precipitation changes influence the mass balance: more precipitation falls as snow, while there is still considerable melting. So variations in precipitation have a delayed effect upon the frontal position, while temperature changes have both a direct effect and a delayed effect. Consequently, glacier advances and retreats reflect temperature changes at present and both precipitation and temperature changes in the past. Mass balance changes at higher elevations are averaged out during the transfer of mass from higher elevations towards the glacier terminus, which only reacts in a smoothed way.

These processes can be modeled using numerical flow line models, and hence the mass balance history of a glacier can be extracted from the glacier length record by means of inverse modeling (e.g. Nye, 1965; Smith and Budd, 1979; Oerlemans, 1997). For Iceland a considerable amount of glacier length data is available (e.g. Sigurdsson, 1998), but it is beyond the scope of this paper to construct numerical flow-line models for one or more outlet glaciers of Vatnajökull. In a less elaborate way, glacier length can be related to mass balance changes with a simple analytical model (Klok and Oerlemans, 2002; Oerlemans, 2001). Here we give a very brief description of this model; for more information the reader is referred to Klok and Oerlemans (2002). For a given length record, the mass balance record can be obtained with the following linear response equation:

$$\frac{dL'(t)}{dt} = -\frac{c\,\beta_E\,B_m'(t) + L'(t)}{t_{rL}} \qquad 3.4$$

where L'(t) is the length with respect to a reference length, $B_m'(t)$ the mass balance with respect to a reference mass balance, c a constant that describes how glacier length is

related to ELA, $\beta_E$ the mass balance gradient at the ELA and $t_{rL}$ the length response time. For a particular glacier, the constants c and $t_{rL}$ can be estimated from several glaciological quantities (surface slope at the snout, minimum elevation, maximum elevation, glacier length, glacier area, glacier width, mass balance gradient and melt rate at the glacier front). Klok and Oerlemans (2002) found that this model performs well for many glaciers, but they note that it is only valid when the slope and width of the tongue do not vary much with distance and when the length fluctuations are relatively small. Also, the lag between forcing and terminus response that is often found is not taken into account, so the extracted $B_m$' may lag the actual forcing. A great advantage of using equation 3.4 over a direct correlation between glacier length and mass balance is that the response time is taken into account. With this model, Klok and Oerlemans (2002) reconstructed the mass balance record of, amongst others, two Icelandic glaciers: Svinafellsjökull and Sólheimajökull. Svinafellsjökull is an outlet glacier on the south side of Vatnajökull and Sólheimajökull is an outlet of another Icelandic ice cap, Myrdálsjökull (figure 3.1). For both glaciers L' and $B_m$' are shown in figure 3.12. L' is linearly interpolated between data points and then smoothed with a Gaussian filter so that the time derivative of L' has no discontinuities. Both length records display a retreat since the second half of the nineteenth century, although the retreat is larger for Sólheimajökull (i.e. Sólheimajökull has a larger c). Also, Sólheimajökull advanced after 1970 while the length of Svinafellsjökull hardly changed. The extracted mass balance records $B_m$' of the two glaciers also display considerable differences. Before 1930 these may be due to gaps in the length record, but after that differences in meteorological forcing are the most likely cause.

Figure 3.12 also shows mass balance records that were obtained with the reduced

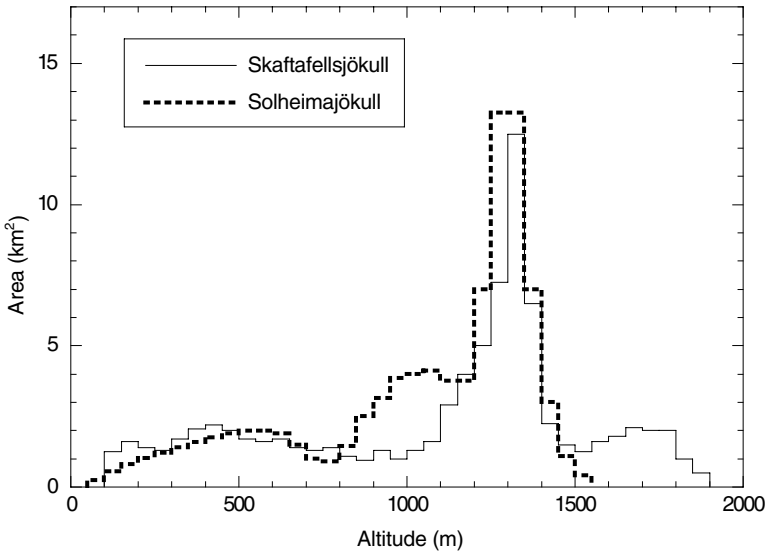


*Figure 3.11. Hypsometry of Skaftafellsjökull (obtained from the DEM) and Solheimajökull (Mackintosh, 2000).*

mass balance model (for a good comparison these were smoothed with the same Gaussian filter as the length records). For Svinafellsjökull we used the full mass balance model to determine an SSC. We only used temperature data (from Stykkishólmur) to force the reduced model, because there is no long-term precipitation record from a location near by. The resulting mass balance record ($B_m^T$) correlates very well with $B_m$' after 1900 (r=0.96 for annual values), which means that since 1900 precipitation variations were not substantial enough to influence glacier lengths on the southern side of Vatnajökull. Furthermore, there is no time lag between the two records, which indicates that Svinafellsjökull generally starts to react almost instantly to climatic changes. For Sólheimajökull we use the SSC of an outlet glacier of Vatnajökull with similar characteristics, namely Skaftafellsjökull. Mean annual precipitation over the two glaciers is roughly the same: glacial runoff measurements indicate a mean annual precipitation of about 4 to 6 m over Sólheimajökull (Lawler et al., 1996), while we find a value of 4 m for Skaftafellsjökull. This correspondence can be explained by the similar proximity to the sea and aspect of the two glaciers (figure 3.1). Also, the hypsometries of the two glaciers resemble each other (figure 3.11), so the two glaciers most probably have similar SSC's. For Sólheimajökull we use temperature data from Stykkishólmur and precipitation data from Stórhöfdi, which lies close to Sólheimajökull. Now, the correlation between the resulting mass balance record ($B_m^{T,P}$) and $B_m$' is even better for the period after 1900 (r=0.99), and $B_m$' lags $B_m^{T,P}$ with 5 years. For both glaciers we can furthermore observe that $B_m^{T,P}$ has higher amplitudes than $B_m$'. This may be due to the smoothing that takes places during the transportation of mass towards the front. Alternatively, the $C_{T,i}$ or the $C_{P,i}$ in equation 3.3 are too high, c in equation 3.4 is too high or $t_{rL}$ in equation 3.4 is too low.

### 3.6 Discussion and conclusions

The situation of Vatnajökull in the North-Atlantic Ocean highly determines its sensitivity to climatic changes. This is well reflected in its Seasonal Sensitivity Characteristic, which gives the sensitivity to temperature and precipitation perturbations in each month of the year. Precipitation is abundant all year round, which makes Vatnajökull a typical maritime ice cap. Temperature sensitivity is high in the summer months while precipitation sensitivity is high in the winter months but low in the summer months. On the other hand, polar air masses influence Iceland from November until March and during these months Vatnajökull is hardly sensitive to temperature changes. In this respect Vatnajökull resembles many drier glaciers. Consequently, Vatnajökull has relatively well defined accumulation (October-April) and ablation (May-September) seasons, and the mass balance of Vatnajökull correlates well to summer temperature and winter precipitation only.

The SSC can be used as a reduced mass balance model to simply and effectively reconstruct the mass balance of Vatnajökull. This confirms the results of O-R, who reconstructed the mass balance of Nigardsbreen in Norway. Since meteorological measurements began in Iceland, there have been considerable decadal-scale changes in both temperature and precipitation, although temperature changes were more persistent and uniform over Iceland. The reduced mass balance model indicates that changes in

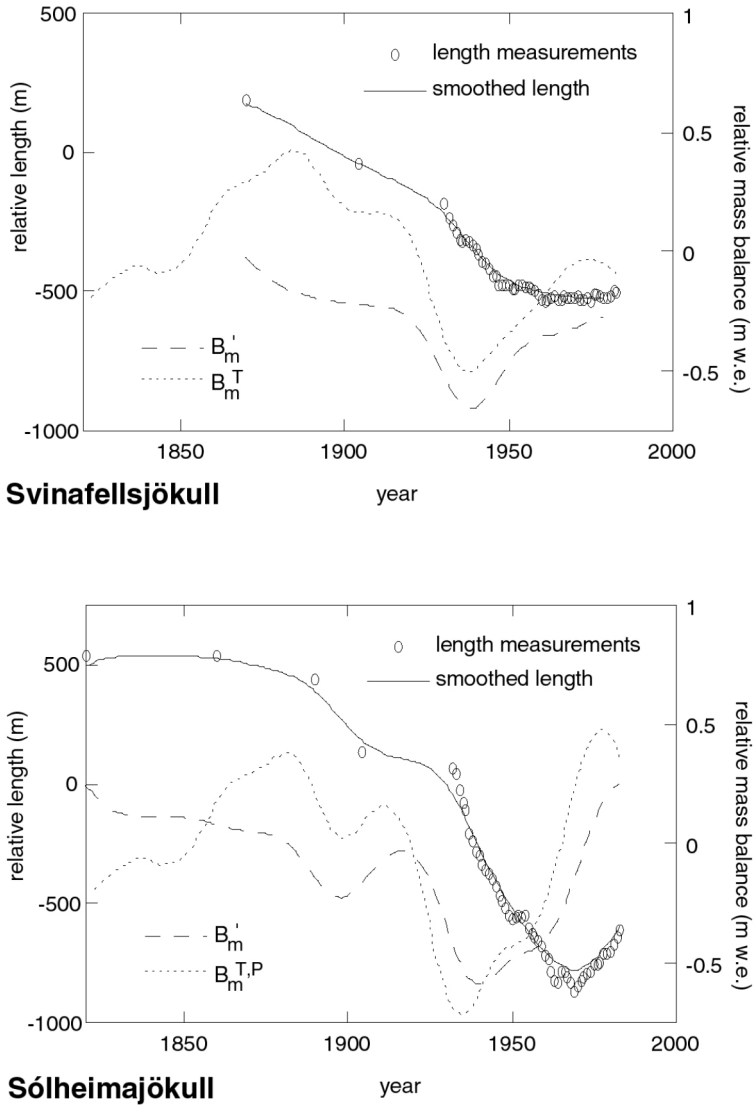


*Figure 3.12. Length fluctuations and changes in mean specific mass balance of Svinafellsjökull and Sólheimajökull. Open circles are point measurements of glacier length. These are first linearly interpolated and then Gaussian filtered in order to obtain a smooth length record. Changes in mean specific mass balance are derived from the historic length changes (*$B_m'$*) and from temperature and precipitation records (*$B_m^T$ *and* $B_m^{T,P}$*).*

temperature and precipitation like the ones observed both have a significant impact upon the mass balance. It seems therefore likely that the different precipitation variations over Iceland result in different mass balance variations for glaciers in different parts in Iceland. Besides temperature and precipitation records, the length record of glaciers is the only

other data source that contains information about the mass balance. By means of inverse modeling the mass balance history can be extracted from these length changes. For two Icelandic glaciers, the resulting mass balance record correlates very well with the mass balance record that we find with the reduced mass balance model (i.e. with forward modeling). This places confidence upon both methods, although the reduced mass balance model indicates larger changes in mass balance than the inverse model. The values of $C_T$ that are used for the reduced mass balance model strongly depend upon the amount of precipitation, and the horizontal distribution of this quantity is not well known over the south of Vatnajökull. Somewhat lower precipitation would lower $C_T$. On the other hand, the glacier characteristics that are needed for the inverse model are estimated from topographical maps and may contain slight errors.

For Svinafellsjökull we find that only temperature perturbations are needed to match the observed length record after 1900, indicating that in the 20$^{th}$ century precipitation variations were not permanent enough to influence glacier length. The same is probably true for all outlet glaciers on the southern side of Vatnajökull, which display a more or less similar length record. The length record of Sólheimajökull is influenced by both temperature and precipitation variations. Increased precipitation largely caused the advance of this glacier after 1965 and the same is probably true for the advance of Seljavallajökull (Sigurdsson, 1998) which lies close to Sólheimajökull. Most other Icelandic glaciers did not advance or only very slightly (Sigurdsson, 1998), so the advance of these two glaciers is probably induced by a local increase in precipitation, which adds to the more general and clearer signature of temperature change.

# 4 A method for monitoring glacier mass balance using satellite albedo measurements: application to Vatnajökull*

**Abstract**

We compare satellite albedo images of Vatnajökull (Iceland) with mass balance measurements for the years 1991-1999. We find that the equilibrium line is mostly not visible when it is located above its position of the previous year(s). Equilibrium line detection is further hindered by clouds and a gradual transition between ice and firn or snow. Consequently, firn line elevation at the end of the melting season is not particularly useful for estimation of the annual mass balance. Instead, we propose to study the mean albedo of the entire ice cap throughout the melting season so that all available information about the surface albedo is taken into account. The mean net potential global radiation, which can be estimated from the mean surface albedo alone, both depends on and influences summer melt. It also depends on winter precipitation and, integrated over the melting season, is found to relate linearly to the mean specific mass balance $B_m$ (r between 0.87 and 0.94 for different outlets of Vatnajökull). $B_m$ can be estimated quantitatively when this relation is known and qualitatively when it is not. The uncertainty in the satellite-derived value of $B_m$ is 0.5 to 0.8 m w.e., which for Vatnajökull corresponds to about 27% of the interannual variability of $B_m$.

## 4.1 Introduction

In recent years there has been significant interest in the state of the cryosphere, because of its sensitivity to climate change. Changes in the cryosphere influence sea level and local climate and are good indicators of climate change. Large parts of the cryosphere, however, lie in remote areas. In only a few places have quantities such as mass balance and terminus location been measured with sufficient temporal and spatial resolution. Satellite remote sensing is a valuable tool for overcoming this problem: it can be used to observe large parts of the cryosphere on a regular basis without the need to actually go there. Decadal-scale changes in the extent of glaciers and ice caps have been monitored with Landsat reflectance images (e.g. Hall et al., 1992; Hastenrath and Greischar, 1997;

* Based on: De Ruyter de Wildt, M. S., J. Oerlemans and H. Björnsson. A method for monitoring glacier mass balance using satellite albedo measurements: application to Vatnajökull (Iceland). *J. Glaciol.*, in press, 2002b.

Williams et al., 1997). It is less straight-forward, on the other hand, to detect yearly variations in mass balance components. Satellite passive microwave sensors can possibly detect the amount of accumulation (Zwally, 1977), although only over regions with dry snow and with little accumulation, and the amount of hoar formation also needs to be known (Abdalati and Steffen, 1998). As a consequence, this method has not been used in practice yet. Microwave data can also reveal the boundary between dry and wet snow, which is why they have also been used to measure the spatial extent (but not the amount) of surface melt (e.g. Steffen et al., 1993; Mote and Anderson, 1995).

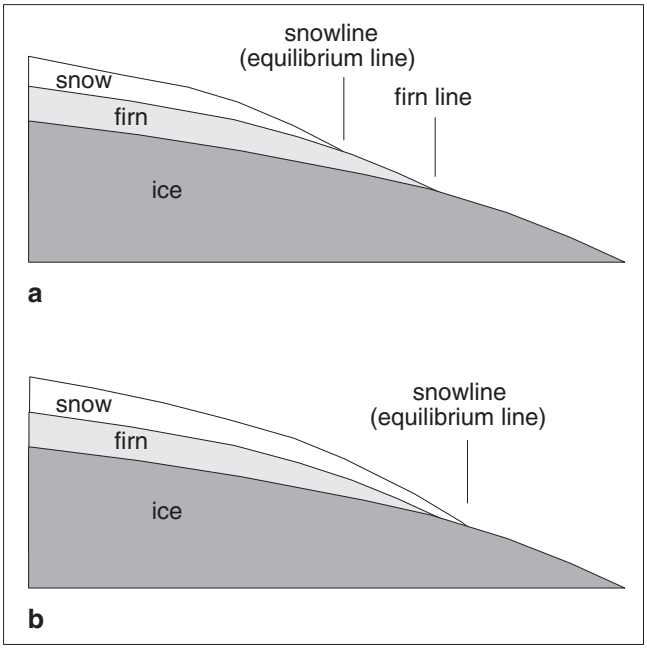


*Figure 4.1. Glacier facies classification for the end of the melting season, based on the age of the material. Superimposed ice is not shown, because in Iceland it is only found sporadically. When the mass balance is (much more) negative than in previous years, firn is exposed and the equilibrium line lies above the firn line (a, after Brown et al., 1999). In the opposite case, when snow covers all firn, only the equilibrium line and not the firn line is visible (b).*

A quantity often found to relate linearly to the mean specific mass balance ($B_m$) is the Equilibrium Line Altitude (ELA) (e.g. Østrem, 1975; Hagen and Liestøl, 1990). According to Østrem (1975), this relation can be used to determine $B_m$ from satellite images that are taken close to the end of the melting season, provided that the boundary between snow and firn (i.e. the equilibrium line) can be detected. Note that we define firn as all snow that is at least one year old, to distinguish it from snow that fell in the mass balance year under consideration. This method has been applied by several authors (e.g. Pelto, 1987; Kulkarni, 1992) although only a few actually validated the satellite-derived mass balance with ground

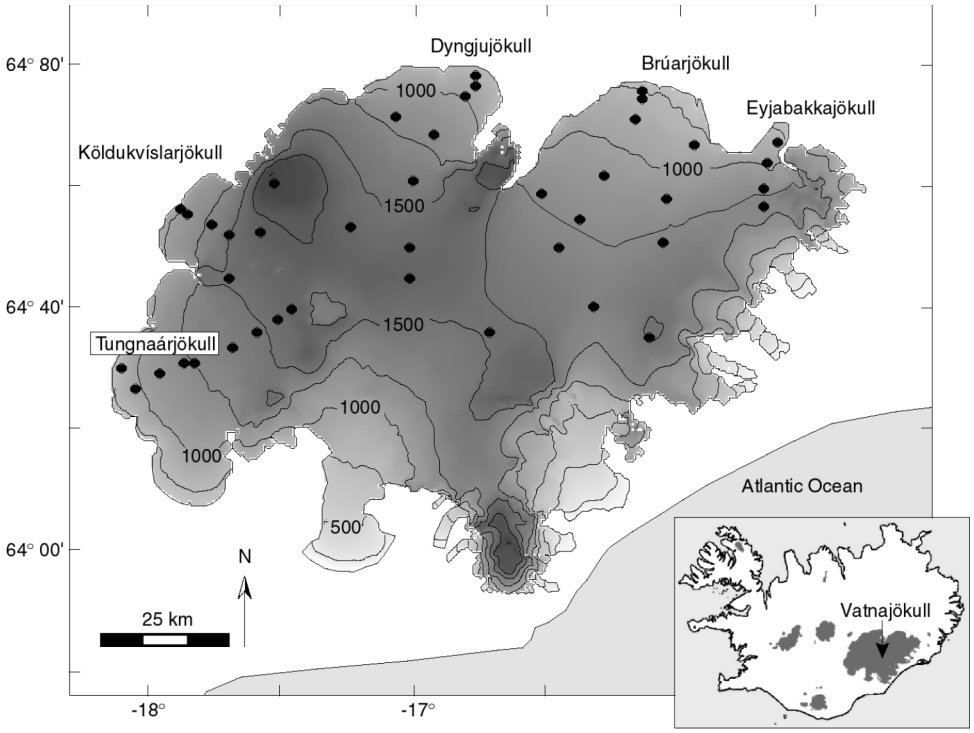


*Figure 4.2. Map of Vatnajökull, based on the DEM used for image processing. The DEM has a horizontal resolution of 500 m. Height-contours are shown for each 250-m interval. Indicated are the outlets where the mass balance has been regularly measured. The black circles indicate sites where the mass balance has been measured.*

measurements (e.g. Rott and Markl, 1989; Demuth and Pietroniro, 1999). There are several reasons for this. First of all, continuous mass balance records that can be coupled to satellite-derived glacier properties exist for only a few glaciers. Furthermore, satellite reflectance images often clearly show the boundary between ice and firn or snow (e.g. Williams, 1987; Reijmer et al., 1999), but snowfall near the end of the melting season can suddenly lower the snow line and hence obscure the equilibrium line. When superimposed ice is present, the equilibrium line lies below the snow line. Apart from this, clouds often limit the availability of reflectance images. Clouds do not pose a problem when radar images are used. The transient snow line is detectable on radar images (e.g. Rott and Mätzler, 1987; Adam et al., 1997; Smith et al., 1997; Brown et al., 1999), but in these studies it has not been related to the ELA or to $B_m$. Although these studies show that the firn line at the end of the melting season can be detected, this does not automatically mean that $B_m$ can be inferred. The snow line, corresponding to the equilibrium line, is clearly visible when no firn is exposed (figure 4.1a). In the other case, the equilibrium line lies above the firn line (figure 4.1b) and may not be detectable due to small albedo differences between firn and snow of a few weeks or months old. This has been observed by Rott and

Markl (1989) and more recently by Hall et al. (2000) and König et al. (2001b).

Demuth and Pietroniro (1999) used the known relation between the ELA and $B_m$ for Peyto Glacier (Canada) to determine $B_m$ from the satellite-derived snow line position. However, they did this for one year which displayed a lower ELA than previous years. Furthermore, they noted that digital elevation model (DEM) and satellite image resolution can limit the detection of changes in ELA. Rott and Markl (1989) used images from a year with positive $B_m$ and from a year with negative $B_m$. They could delineate the snow line in the year with negative $B_m$ on Hintereisferner (Austria), but not on neighboring Kesselwandferner. Another study in which satellite observations are quantitatively coupled to mass balance observations is from Greuell and Knap (2000). For a period of eight years, these authors find a correlation between the satellite-derived slush line position and $B_m$ for the Greenland ice sheet, but the applicability of this relation is limited because of an upper boundary which the slush line cannot exceed.

In this paper, we use mass balance data and satellite images from several years to analyze the relation between the firn line and the equilibrium line. We also describe a new method to infer $B_m$ from satellite images, which only requires satellite imagery. This means that it can be applied to any ice cap or glacier. An important aspect of the method is that the whole surface of a drainage basin during the melting season is studied, and not only a specific transition between glacier facies for a specific day. This takes all available information about the surface albedo into account. As a test case we study Vatnajökull in Iceland. For this ice cap there are mass balance measurements available, with which the satellite images can be compared quantitatively. Vatnajökull is one of the largest temperate ice masses in the world (8200 $km^2$ in 1995) and consists of several domes, large lobes and valley glaciers (figure 4.2). Owing to the position of Iceland in the middle of the North Atlantic storm track, the skies are overcast most of the time and albedo retrieval is often not possible. This means, however, that if we can use satellite albedo images to retrieve $B_m$ here, cloudiness will probably not be a problem for ice masses that are less frequently covered by clouds. Because of the size of Vatnajökull, AVHRR images from the NOAA satellites, which have a resolution of 1.1 km at nadir, can be used. These images are not expensive and have the advantage of being available for several times per day, so obtaining good time series is feasible. Both *in situ* data and satellite data are from the years 1991 to 1999 inclusive.

## 4.2 *In situ* mass balance data

The mass balance of Vatnajökull has been measured with sufficient spatial resolution since 1992 (Björnsson et al., 1997, 1998a, b, c, 1999; Sigurdsson, 1997; O. Sigurdsson, personal communication, 2001). For one drainage basin (Eyjabakkajökull) data from 1991 are available. The data have mainly been obtained over the drainage basins of Eyjabakkajökull, Brúarjökull, Dyngjujökull, Köldukvíslarjökull and Tungnaárjökull (figure 4.2). Most measurements were taken at the end of September or the beginning of October. On each outlet, the mass balance has been measured along one or two profiles which capture the altitudinal variation. Figure 4.3 displays the mass balance gradient for some drainage basins. It

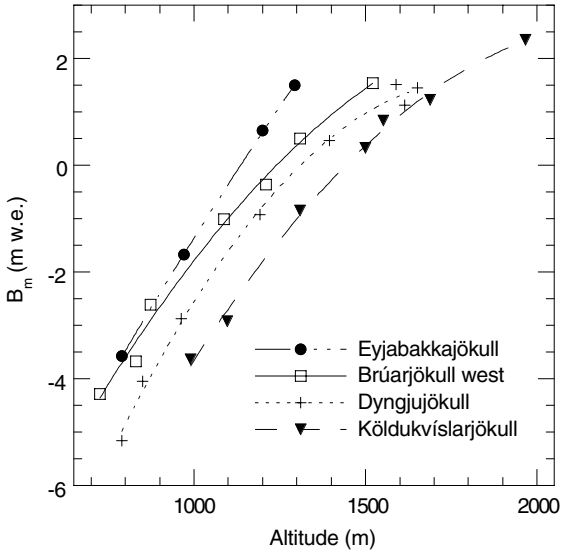


*Figure 4.3. Average mass balance gradient along the flow lines of four representative drainage basins of Vatnajökull. Each point represents a measurement site. The curve fits are 2$^{nd}$-order polynomials.*

shows that the amount of annual precipitation influences the mean ELA: the ELA varies from about 1050 m (Eyjabakkajökull) to about 1440 m (Köldukvíslarjökull). Eyjabakkajökull lies closest to the coast and receives most precipitation, while Köldukvíslarjökull has a less maritime and drier climate. Because most of Vatnajökull is quite flat, the profiles can be used together with a few additional measurement sites to describe the lateral variation. The mean specific balances of the areas are obtained by interpolation between the measurement sites. For this interpolation, we developed an algorithm that takes vertical gradients into account. A DEM is needed for this feature to work. For each grid point of the DEM (displayed in figure 4.2), the algorithm determines the n closest measurement sites within 500 m in altitude from the grid point. Then, because of the limited height differences, a linear relation between mass balance and altitude is found for the n measurement sites, with which the mass balance at the grid point can be calculated. To smooth discontinuities in the resulting mass balance field, the contribution of each measurement site is weighted with the inverse of its distance to the grid point. The resulting values of $B_m$ are not very sensitive to the value of n. We therefore use a value of 6, which is the lowest value that gives smooth mass balance fields. The resulting mean specific mass balances are displayed in table 4.1. The data clearly include years with a highly positive $B_m$ (1992, 1993) and years with a highly negative $B_m$ (1997,1998).

| year | western Brúarjökull | eastern Brúarjökull | Eyjabakka-jökull | Dyngju-jökull | Köldukvís-larjökull | Tungnaár-jökull | all |
|---|---|---|---|---|---|---|---|
| 1991 | | | -0.90 | | | | |
| 1992 | | | | | 0.81 | 0.35 | |
| 1993 | 1.32 | 0.89 | 0.69 | 1.58 | | 0.23 | 1.16 |
| 1994 | 0.55 | | 0.42 | 0.36 | 0.03 | -0.11 | 0.31 |
| 1995 | 0.22 | | -0.48 | 0.04 | -0.64 | | -0.31 |
| 1996 | -0.04 | -0.76 | -0.88 | -0.21 | -0.68 | | -0.54 |
| 1997 | -1.04 | -1.79 | -1.88 | -0.85 | -1.07 | -2.18 | -1.30 |
| 1998 | -0.46 | -0.94 | -1.57 | -0.53 | -0.80 | -1.53 | -0.77 |
| 1999 | -0.09 | -0.56 | -0.72 | | -0.58 | -0.99 | -0.26 |
| mean | 0.07±0.28 | -0.63±0.43 | -0.66±0.31 | 0.07±0.35 | -0.42±0.24 | -0.71±0.42 | -0.24±0.30 |

*Table 4.1. Mean specific mass balances (in m w.e.) as obtained by interpolation for different drainage basins of Vatnajökull. The weighted mean for the whole northwestern part of Vatnajökull (all) is shown when the mass balance was measured over the largest part of this area. The last line displays the means and the standard deviation of each time series.*

### 4.3 Satellite images: processing

AVHRR images were purchased from the Satellite Receiving Station at the University of Dundee (Scotland). We selected 107 images taken from April until September that display few clouds over the ice cap (9 - 15 images per year). Images from the years 1991 to 1994 were taken from the NOAA-11 satellite. Afterwards, the NOAA-14 satellite provided the images. The images cover the melting seasons of most years reasonably well. For 1993, which had a cold summer with high cloudiness, we found the fewest images (9), and only two images that had been taken before July 15$^{th}$. Most images display clouds, so on a certain image some drainage basins may be largely covered by clouds. Nearly all images were taken close to solar noon so that solar irradiance was large. The solar zenith angle ranged between 40° and 66° on all images except for one image at the very beginning of the melting season. The satellite images need to be processed in order to retrieve the surface albedo. The retrieval method is based on the method of Reijmer et al. (1999), although there are a few differences. The processing steps are described below and include cloud masking, geolocation, calibration, atmospheric correction, narrow-to-broadband conversion, correction for anisotropy of the reflected radiation and correction for surface inclination.

#### *4.3.1 Cloud masking*

Developing fully automated techniques for cloud masking over snow surfaces is difficult, because clouds can have the same thermal and visible characteristics as snow. There are automated techniques that detect textural characteristics of clouds (Ebert, 1987), but these could not be applied to Vatnajökull because they classify some of the glacier's surface as

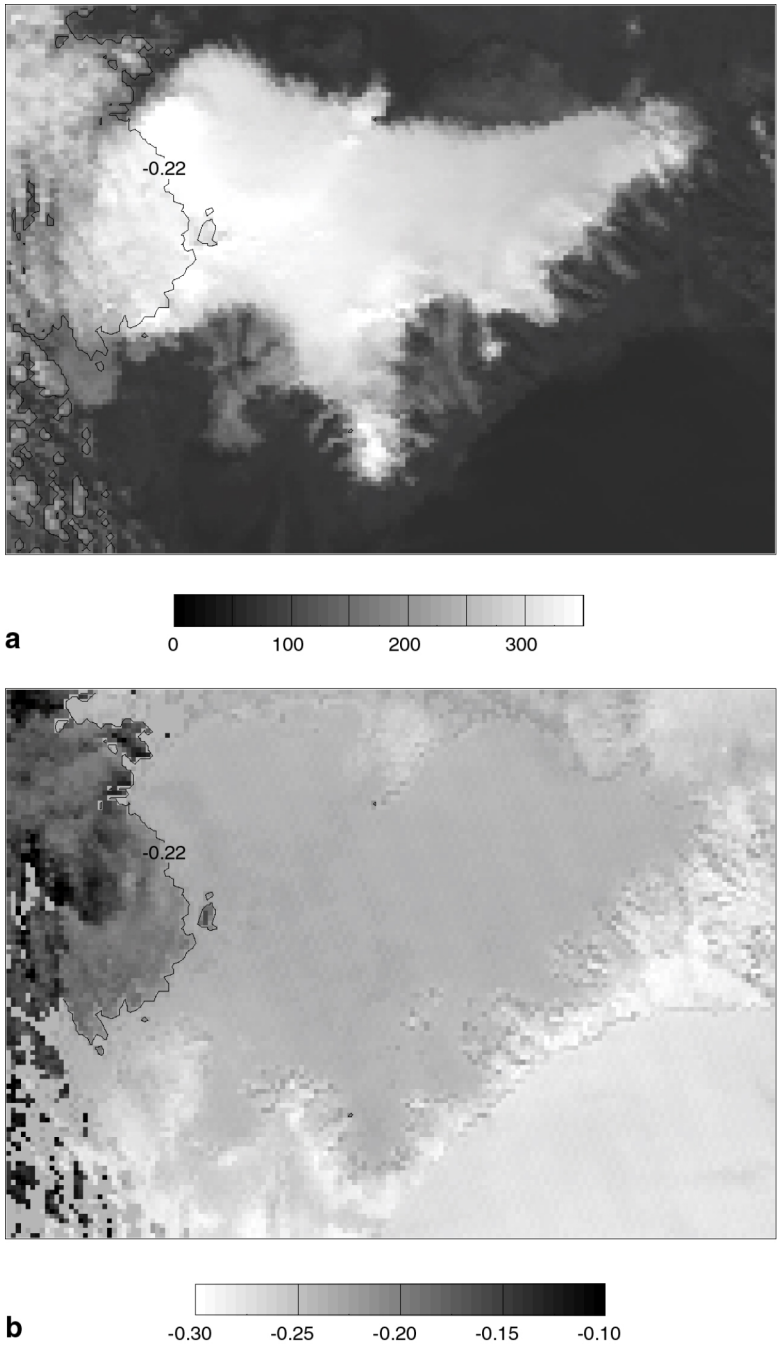


*Figure 4.4. Channel 1 count number (a) and normalized differential cloud index (b) for Vatnajökull on September 8th, 1996. In both plots the -0.22 contour of the normalized differential cloud index is shown.*

clouds (e.g. bands of low ice albedo, firn-ice transition). Some authors were able to mask clouds reasonably well (e.g. Gesell, 1989; Raschke et al., 1992; Baum and Trepte, 1999) using the reflective and thermal differences that often, but not always, exist between clouds and snow surfaces. Here we make use of the reflective and thermal differences in AVHRR channel 3 (3.55-3.93 μm) and the thermal differences in channel 4 (10.5-11.5 μm) that are often present. We empirically found that the following normalized differential index masks most clouds over Vatnajökull:

$$R_{34} = \frac{C_3 - C_4}{C_3 + C_4} \qquad 4.1$$

where $C_i$ is the raw count level in AVHRR channel i. Depending on the temperature difference with the surface, clouds are mostly discernible from the surface in one or in both of these channels. Therefore, $R_{34}$ often detects clouds in different thermal ranges, over snow and ice, and over bare land as well. For each individual image, we apply a threshold for $R_{34}$ to mask clouds. This method does not detect all clouds, so we had to check the images manually for errors. A convenient way of doing this is to compare subsequent images and look at textural characteristics. On some images, a difference between the detected cloud margin and the corresponding change in albedo is present, which is caused by shadow casting. However, this applies only to few images and to small areas. As an example we show channel 1 (operating in the visible part of the spectrum) count number and $R_{34}$ for one image (figure 4.4). In the west, bright clouds, obscuring the firn line and the ice cap margin, are visible over the otherwise dark land surface (figure 4.4a). These clouds are visible in a plot of $R_{34}$, even over snow and ice (figure 4.4b).

### *4.3.2 Geolocation*

We apply a geolocation to each image by comparing the images to the DEM. The horizontal resolution of the DEM is smaller than the AVHRR pixel size, namely 500 m. The DEM is given in rectangular co-ordinates while the AVHRR images are given in cylindrical stereographic co-ordinates. Because of this we have to rotate the images slightly around the centre of the ice cap in order to obtain a good fit. Then we fit the ice cap margin and several height contours from the DEM to the AVHRR channels 1 and 3. Channel 1 shows sharp mountain peaks and steep ridges (because of changes in surface albedo) and channel 3 clearly shows the margin of the ice cap (because melting snow and ice, unless heavily debris-covered, are colder than land). We were able to locate these features on most images with an accuracy of one pixel. The accuracy of the geolocation for a few images with a large satellite viewing angle is estimated to be two pixels.

### *4.3.3 Calibration*

The AVHRR instruments record radiation intensities, which must be converted into radi-

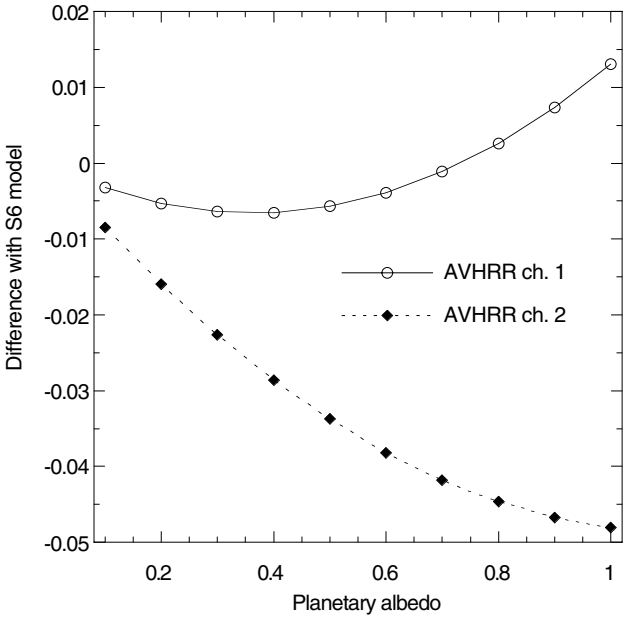


*Figure 4.5. Difference between the surface albedo from the 6S radiative transfer model and from the Slingo and Schrecker model as a function of planetary albedo. For both models, the same solar zenith angle (about 50°), surface elevation (250m), and atmospheric profile were used. The zenith angles are representative of the images used in this paper. Differences are shown for the AVHRR channel 1 and 2 narrowband albedos.*

ances. Rao and Chen (1995) and Rao and Chen (1999) give calibration coefficients for channels 1 and 2 of the AVHRR instruments aboard the NOAA-11 and NOAA-14 satellites, respectively. These coefficients take instrument drift into account. The radiances are simply converted into planetary albedos at the top of the atmosphere by taking the solar elevation and the distance between the sun and the earth into consideration.

### *4.3.4 Atmospheric correction*

The effect of the atmosphere on the albedo is generally linear:

$$\alpha_{srf,i} = a_i + b_i \ \alpha_{pla,i} \qquad 4.2$$

where $\alpha_{srf,i}$ is the surface albedo in channel i, $\alpha_{pla,i}$ is the planetary albedo in channel i, and $a_i$ and $b_i$ are constants for channel i that depend on the surface altitude, the solar zenith angle, the satellite zenith angle and the composition of the atmosphere. For a given image and assuming a horizontally homogenous atmosphere over the ice cap, the constants are

only a function of surface altitude (Reijmer, 1997). This means that we only have to calculate this dependence once for each entire image. The atmospheric correction can then simply be applied to all image pixels, because the DEM gives us the altitude of the surface in a pixel. The constants are calculated by means of a radiative transfer model (Koelemeijer et al., 1993), which is based on the model of Slingo and Schrecker (1982). It takes Rayleigh scattering and attenuation by ozone and water vapor into account but neglects the effect of aerosols. The model is physically less complex than models such as the 6S radiative transfer model (Tanre et al., 1992; Fily et al., 1997; Stroeve et al., 1997) but also less time-consuming. When we compare the two models for a representative solar zenith angle and with the same atmospheric profile, the resulting surface narrowband albedos appear to differ very little for AVHRR channel 1, but more for channel 2 (figure 4.5). However, the two differences partially counteract and moreover, $\alpha_{srf,1}$ has a much larger weight in the surface broadband albedo than $\alpha_{srf,2}$ (see below). Because of this, the surface broadband albedos of the two models do not differ more than 0.012 for the entire range of albedo values. This comparison is made for a surface altitude of 250 m, so the differences will probably be even smaller for most of Vatnajökull, where the altitude is higher and the atmospheric correction smaller. Therefore, we conclude that it is not necessary to use the more time-consuming 6S model. Because the results of both models are not very sensitive to the atmospheric profiles (Reijmer, 1997; Stroeve et al., 1997), we use the standard Sub Arctic Summer Profile of McClatchey et al. (1972) as input.

### *4.3.5 Narrow to broadband conversion*

The surface narrowband albedos that are measured in AVHRR channel 1 and 2 have to be converted into a broadband albedo over the solar spectrum. Here we use the empirical expression (W. Greuell, personal communication, 2001)

$$\alpha_{srf} = 0.508\,\alpha_{srf,1} + 0.065\,\alpha_{srf,1}^2 + 0.268\,\alpha_{srf,2} \qquad 4.3$$

where $\alpha_{srf}$ is the surface broadband albedo. This expression is based on many (8,000) point measurements that were made simultaneously in AVHRR channel 1 and 2 and over the entire solar spectrum. Incoming fluxes were measured on the ice cap surface and outgoing fluxes were measured from a helicopter that flew at low altitude over Vatnajökull. Methods and data from this experiment are described in Greuell et al. (2002). A broad range of surface types was observed, ranging from dirty glacier ice to melting snow and having broadband albedos between 0.05 and 0.80. Equation 4.3 corresponds very well to the data with a residual standard deviation of 0.008. Measurements over dry snow are not available, but during the melting season dry snow hardly occurs on Vatnajökull.

### *4.3.6 Anisotropic correction*

Snow and ice reflect solar radiation anisotropically, so the satellite-derived albedo depends

on the view geometry. The function that describes the reflection of solar radiation as a function of the view geometry is called a Bidirectional Reflectance Distribution Function (BRDF). It varies with wavelength, solar elevation and (sub)surface properties such as grain size and impurity content (e.g. Warren, 1982; Nolin and Stroeve, 1997). Liquid water has an indirect effect because it enlarges the effective grain size. Although existing theoretical models take these effects into account (e.g. Fily et al., 1997; Nolin and Stroeve, 1997; Leroux et al., 1999), it is not (yet) possible to extract independent information about grain size, water content and impurity content from satellite imagery. We use an empirical BRDF (Koks, 2001) that is based on measurements above melting snow of two or three weeks old, and is valid for a broad range of solar zenith angles (15.9° - 65.5°). The methods and derivation of this BRDF are nearly the same as in Greuell and De Ruyter de Wildt (1999). The measurements were made in Landsat Thematic Mapper bands 2 and 4, but following Greuell and De Ruyter de Wildt (1999) we can argue that they are also applicable to AVHRR bands 1 and 2, respectively. During the summer virtually all surface snow of Vatnajökull is melting and metamorphosed, so the parameterization is likely to be valid for the average summer conditions on Vatnajökull. The parameterization is given in appendix 4A.

Greuell and De Ruyter de Wildt (1999) present empirical BRDFs that were measured over ice on the Morteratsch glacier in Switzerland. It is, however, questionable whether these are applicable to Vatnajökull. Glacier ice may contain air bubbles, dust inclusions and cracks that influence anisotropy. Moreover, much of the glacier ice of northern Vatnajökull (Dyngjujökull and large parts of Brúarjökull and Köldukvíslarjökull, see figure 4.2) is partly or entirely covered by volcanic deposits, called tephra, which reflect solar radiation more isotropically than snow and ice. For these reasons we did not apply any corrections for anisotropy over glacier ice and tephra-covered glacier ice.

#### *4.3.7 Correction for surface inclination*

In the above, the fluxes are calculated with respect to a horizontal plane. This means that over a horizontal surface, the calculated albedo is the actual surface albedo. However, if the surface is inclined, the fluxes through a plane parallel to the surface differ from those through the horizontal plane and a correction needs to be applied to obtain the surface albedo. We calculate the surface albedo with the expression of Knap et al. (1999).

### 4.4 Satellite images: results

#### *4.4.1 Development of the surface albedo during the summer*

Figure 4.6 displays some images with few clouds of the summer of 1996. The images show a gradual decrease of the albedo in the accumulation area, from about 0.8 to about 0.6, and a gradual rise of the snow line. In August this rise comes to a standstill and the situa-

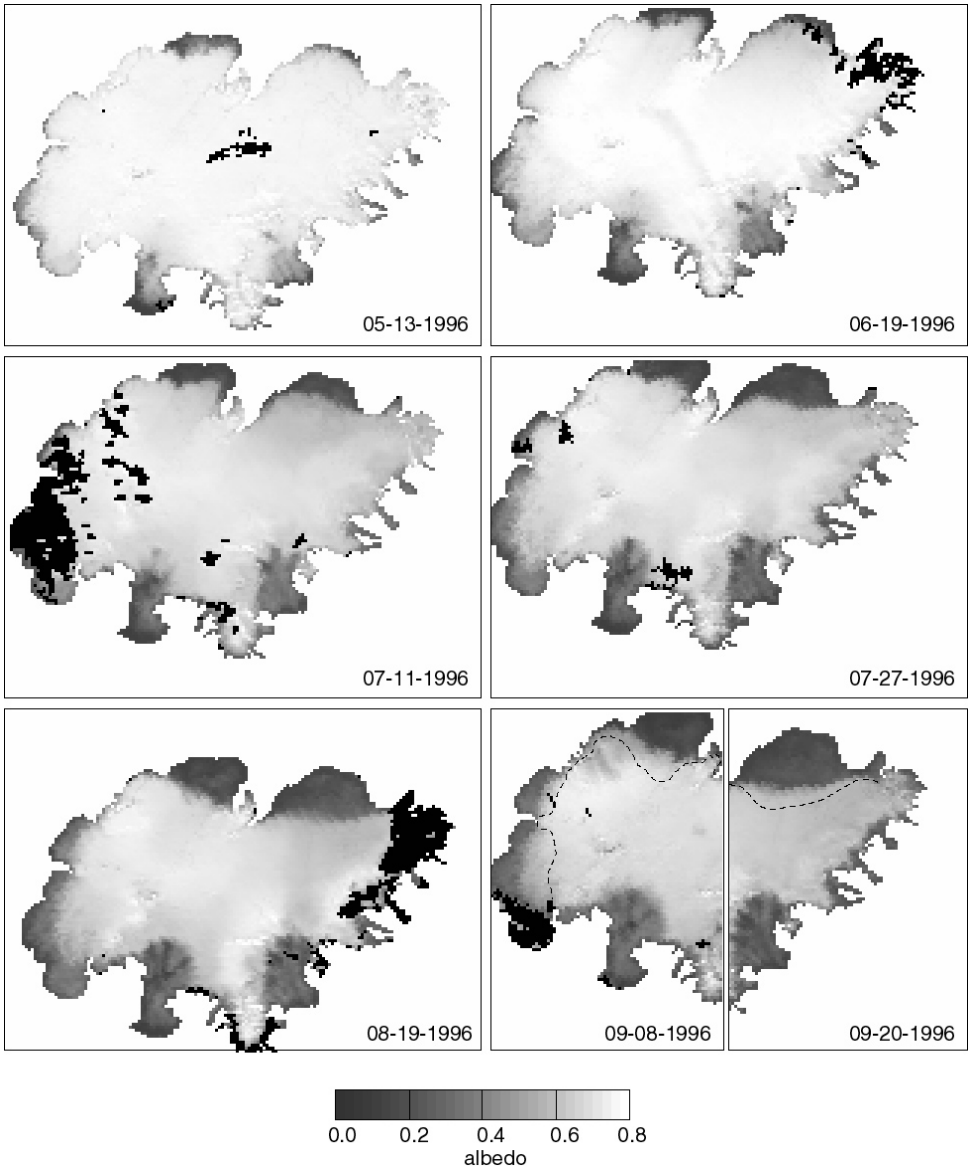


*Figure 4.6. Six selected NOAA AVHRR albedo images for the summer of 1996. Each image shows the margin of Vatnajökull (dashed line) and the 0.35 albedo contour (solid line). In the last image (September 20th), the equilibrium line is also plotted (inner dashed line). The equilibrium line is obtained by interpolating the mass balance measurements, as described in the text. Because the mass balance was only measured over the northwestern half of Vatnajökull, no equilibrium line is plotted in the south and southeast. Black pixels indicate clouds.*

tion remains stationary until the end of the melting season. This is probably a consequence of the albedo of firn being close to the albedo of relatively old snow. The albedo in the ablation area is more constant in time than in the accumulation area. In the northern and northwestern ablation areas, the albedo is very low (around 0.1) and quite homogenous. This is caused by the tephra covering the ice in this region. Zones with clean ice do occur (Larsen et al., 1998), but they are not resolved by the AVHRR images. In the south and southeast the albedo of the ablation area varies considerably on the satellite pixel scale and lies between 0.15 and 0.35 (figure 4.6). On a smaller scale there is even more variability in these regions (Reijmer, 1997).

### *4.4.2 Errors*

All processing steps introduce some uncertainty in the surface albedo. The uncertainties resulting from most processing steps are not very large: less than 0.05 (Reijmer, 1997). The uncertainty introduced by neglection of anisotropy over ice and by the correction for anisotropy over snow is hard to quantify. It will be largest for large satellite zenith angles and extreme surface types (extremely wet and metamorphosed snow on one hand and dry snow on the other hand). From the available information about BRDFs (e.g. Suttles et al., 1988; Stroeve et al., 1997; Greuell and De Ruyter de Wildt, 1999) we estimate the uncertainty to be 0.15 in extreme cases but considerably smaller for most images and locations.

## 4.5 Mass balance retrieval from satellite images

### *4.5.1 Detection of firn line and equilibrium line*

According to Østrem (1975) it may be possible to infer $B_m$ from satellite images if the equilibrium line can be detected. This idea is based on the linear relation between the ELA and $B_m$. We investigate this for two representative outlets of Vatnajökull, namely Brúarjökull in the northeast and Tungnaárjökull in the west. Figures 4.8 and 4.7 display albedo profiles of these two outlets at the end of several melting seasons. Note that there are no profiles for 1999, due to a lack of cloud-free images at the end of the summer. Over Brúarjökull the transition from ice to firn and snow is quite sharp in most years, but over Tungnaárjökull it is often too gradual to determine the transition accurately. The annual mass balance measurements on Tungnaárjökull display strong fluctuations superimposed upon a linear increase with altitude, probably caused by snowdrift. Synthetic Aperture Radar images from the European Space Agency ERS satellites with a horizontal resolution of 33 m (see chapter 0) show that there is no real firn line on Tungnaárjökull, but rather a transition that occurs in patches. This can partially be seen in the profile over Tungnaárjökull for 1993 (figure 4.7), but mostly the resolution of the AVHRR images is too low to resolve the patches.

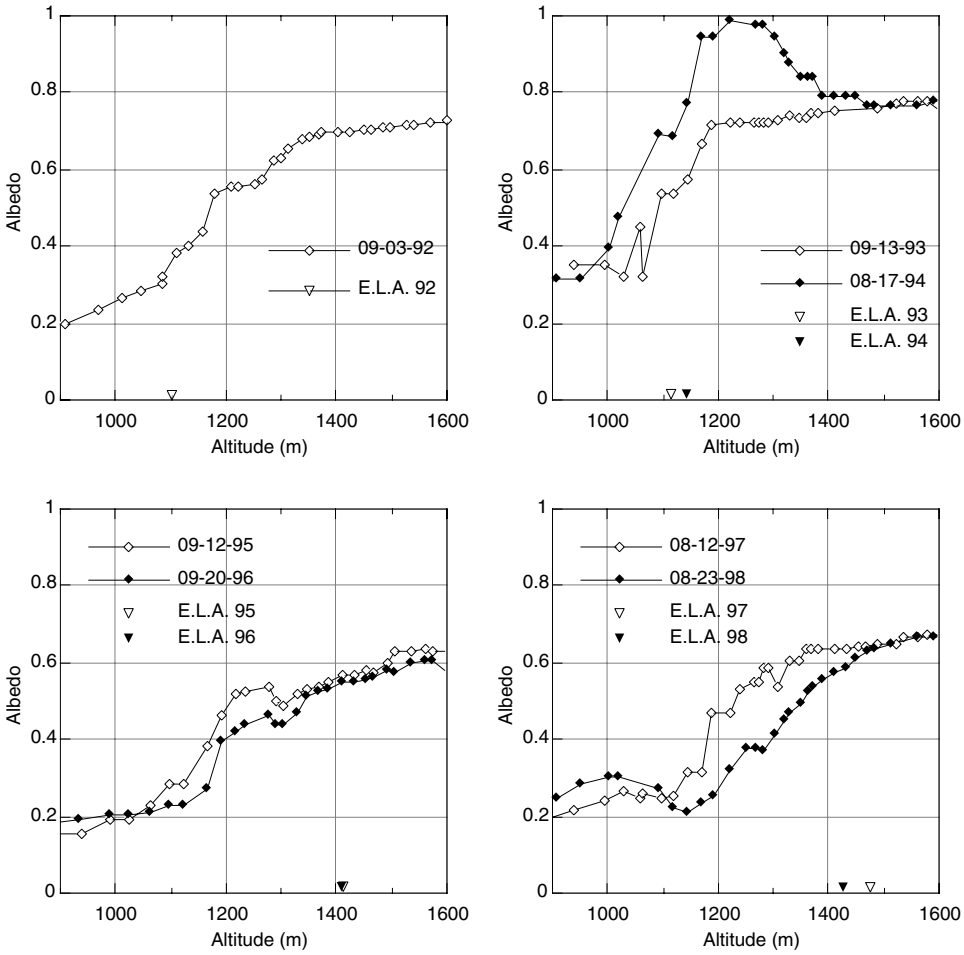


*Figure 4.7. Satellite-derived albedo profiles along a flow line of Tungnaárjökull at the end of the melting season, for several years. The mass balance measurements from which the ELAs are determined were made along the same flow lines. In 1995 and 1996, no measurements were made on Tungnaárjökull and no suitable image is available for the end of the melting season of 1999. For all years, the image that displays the highest firn line is used to obtain the profiles.*

Both on Brúarjökull and on Tungnaárjökull the transition coincides with the equilibrium line in 1993 and 1994, which were years with a positive $B_m$ (table 4.1). In 1995-1998, which were all years with a negative $B_m$, the equilibrium line lay significantly higher than the upper ice margin which means that firn had emerged at the surface (also see figure figure 4.6). It is furthermore interesting to see that on both outlets, the firn line was located at approximately the same altitude in these four years (figures 4.8 and 4.7). In consecutive years of negative $B_m$ the firn line will rise of course, but only very slowly. The firn line marks therefore a transition between nearly static glacier facies (the wet-snow zone and the ablation area), which is the result of meteorological processes during the last years or

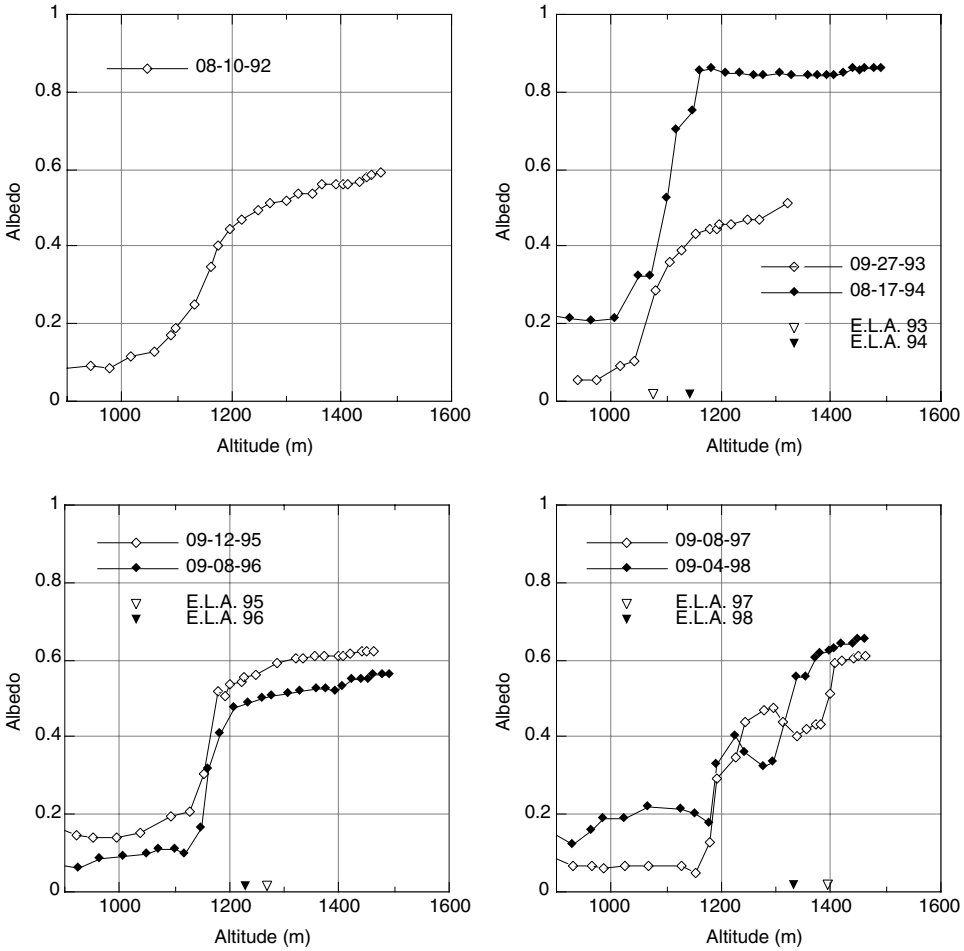


*Figure 4.8. Satellite-derived albedo profiles along a flow line of western Brúarjökull at the end of the melting season, for several years. The mass balance measurements from which the ELAs are determined were made along the same flow lines. In 1992, no measurements were made on Brúarjökull and no suitable image is available for the end of the melting season of 1999. For all years, the image that displays the highest firn line is used to obtain the profiles.*

decades. Hence, the firn line reflects the mean equilibrium line over several years. The same has been observed by Hall et al. (1995) and König et al. (2001b), who found that the firn line coincides with a radar backscatter boundary related to subsurface glacier facies. On Brúarjökull a second transition was present in 1997 and 1998, the years with the highest equilibrium line (figure 4.8). This second transition coincides with the equilibrium line and we assume that it is the boundary between the snow and firn. However, this higher transition did not occur in all years and not on Tungnaárjökull and can, therefore, not be used to determine the equilibrium line. Summarizing, the equilibrium line is detectable on

satellite albedo images when it is not located above its position of the previous year(s), i.e. the firn line. In years when the snow line retreats far enough to reveal firn, the use of albedo monitoring for determination of the equilibrium line is limited because of the small albedo difference between snow and firn.

### 4.5.2 Mass balance retrieval from the integrated surface albedo

The appearance of firn and/or slush with low albedos in warm years obscures the equilibrium line, but at the same time provides extra information that may be used to infer $B_m$. For example, the mean albedo of the entire accumulation area depends on the age of the snow and hence on the mass balance in the accumulation area. The mean surface albedo of the ice cap not only reflects the amount of accumulation and ablation in the preceding part of the mass balance year but also strongly affects net shortwave radiation and hence summer melt. To take this feedback into account we convert the satellite-derived surface albedo into the net potential global radiation:

$$Q_{pot,net} = Q_{pot}\left(1-\alpha_{srf}\right) \qquad 4.4$$

where $\alpha_{srf}$ is the satellite-derived surface albedo, $Q_{pot}$ is the potential global radiation, defined as the incoming solar radiation at the top of the atmosphere, and $Q_{pot,net}$ the net potential global radiation. $Q_{pot,net}$ is the potential absorption of solar energy per unit surface area. This differs from the actual absorption of solar energy ($Q_{net}$) which is lower due to atmospheric attenuation. However, the satellite images mostly display low cloudiness or no cloudiness at all and are in this respect not representative. Cloudiness strongly determines the amount of solar energy that reaches the surface, but the average cloudiness over a time interval is not known over remote and/or large ice caps and glaciers. Hence it is not possible to retrieve $Q_{net}$ over long time intervals from satellite images, which is why we compute $Q_{pot,net}$ instead. Note that it is necessary to take atmospheric effects upon the albedo into account, because several processing steps in the albedo retrieval process need to be applied upon the surface albedo, and not upon the planetary albedo (e.g. anisotropic correction, narrow to broad band conversion).

$Q_{pot}$ can be easily calculated from standard astronomical theory (e.g. Walraven, 1978). We propose that $Q_{pot,net}$, integrated over the ice cap and over the summer, is related to $B_m$:

$$B_m \propto \sum_{summer} < Q_{pot,net} > = \sum_{summer} \frac{1}{A} \sum_{glacier} Q_{pot,net} \qquad 4.5$$

where $<Q_{pot,net}>$ is the net potential global radiation, averaged over the surface with area A. Equation 4.5 can be evaluated by simple linear interpolation between the days for which images are available, but this may result in unrealistic curves when only few images are available. Also, all images from which $<Q_{pot,net}>$ is derived may show partial cloud cover and the visible part of a drainage basis may not be representative of the entire drainage

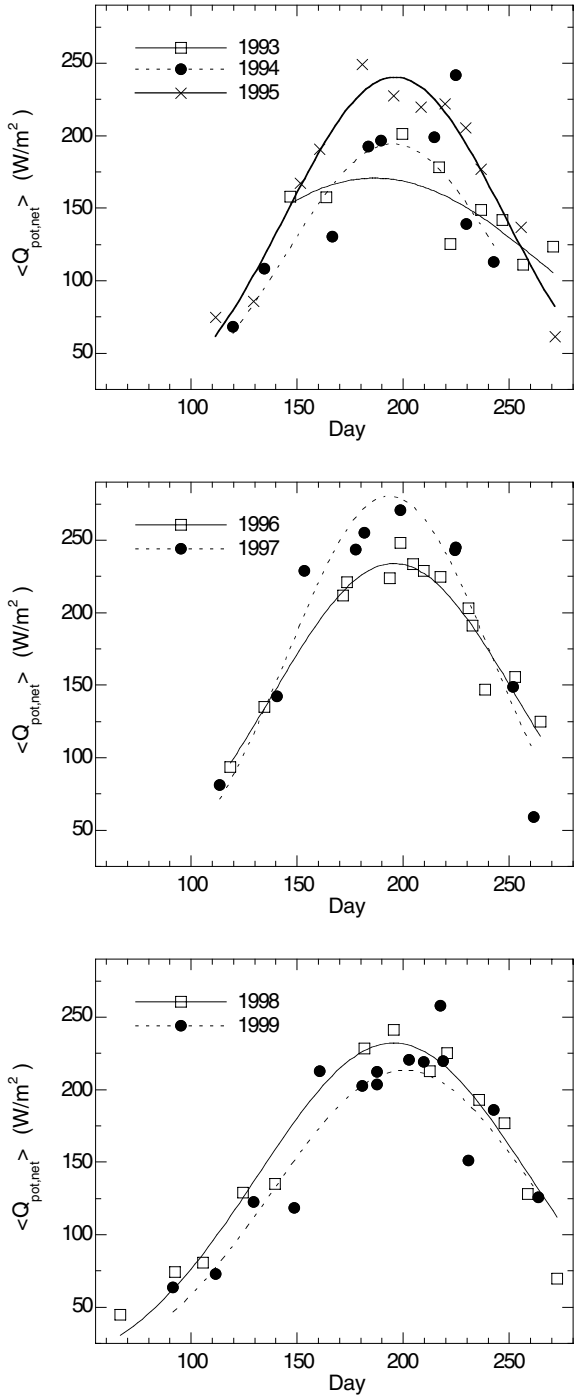


*Figure 4.9. Satellite-derived net potential global radiation (<$Q_{pot,net}$>), averaged over the northwestern part of Vatnajökull, as a function of the day of the year. Data for several years are shown. The curves are fits of equation 4.6 to the data points.*

basin. Therefore, we use an analytical expression for $<Q_{pot,net}>$ that incorporates a priori knowledge about the course of $<Q_{pot,net}>$ during the summer. We find that the following function fits well to the data (disregarding disturbances by clouds):

$$< Q_{pot,net} > = a \exp\left\{ -\left(day - b\right)^2 / c \right\} \qquad 4.6$$

where day is the day of the year, and a, b and c are constants. This function resembles a normal distribution and has a maximum of magnitude a at day b and approaches zero on either side of this maximum. The constant c indicates the width of the curve. We fit this expression to the satellite-derived values of $<Q_{pot,net}>$, which are weighted with the percentage of glacier area that is visible. This means that images with few clouds have large weights and images with many clouds have small weights. As an example we show fits of equation 4.6 to the satellite-derived values of $<Q_{pot,net}>$ for the entire northwest of Vatnajökull (figure 4.9). Deviations from the curve fits are mainly caused by clouds (these data points have small weights) and snowfalls. For example, the high value of $<Q_{pot,net}>$ on day 224 in 1994 is caused by clouds (84% of the satellite pixels are classified as clouds). The low value of $<Q_{pot,net}>$ on day 238 in 1996 is caused by high albedos due to recent snowfall. On the image taken at this day, the snow line lies well below the firn line during the weeks before and after this day.

When we use a time step of one day and integrate equation 4.6 over the longest period covered by the satellite images in all years (day 146 - day 242), we find that the integrated values of $<Q_{pot,net}>$ correlate linearly with $B_m$ (figure 4.10). Prescribing fewer degrees of freedom by setting b and/or c to some value or by using second- and third-order polynomials instead of equation 4.6 hardly affects this. When we consider only the albedo instead of $Q_{pot,net}$ the results do not improve either and even become slightly worse. This is probably due to the total amount of solar energy delivered to the surface being disregarded. For all drainage basins the correlation between $<Q_{pot,net}>$ and $B_m$ is high (table 4.2).

## 4.6 Discussion

The methods that lead to the data in figure 4.10 all introduce some uncertainty, which must be taken into account to assess the applicability of the $B_m$ - $<Q_{pot,net}>$ regression model. The uncertainty in the directly measured $B_m$ is difficult to assess and for all drainage basins we will use the same first-order estimate. From comparing different estimates of $B_m$ we estimate the uncertainty to be 0.25 m w.e., which is a conservative value. The uncertainty due to the regression model ranges from 0.24 m w.e. (the entire northwest of Vatnajökull) to 0.51 m w.e. (Tungnaárjökull). The largest uncertainty is introduced by $<Q_{pot,net}>$ (table 4.2). The source of this uncertainty is two-fold: the satellite retrieval method introduces an uncertainty, and there is an error associated with the analytical expression for $Q_{pot,net}$ (figure 4.9). The resulting error in the satellite-retrieved mean specific mass balance ($B_{m,Q}$) is computed from the regression coefficient $dB_m/d<Q_{pot,net}>$. This slope, and hence the result-

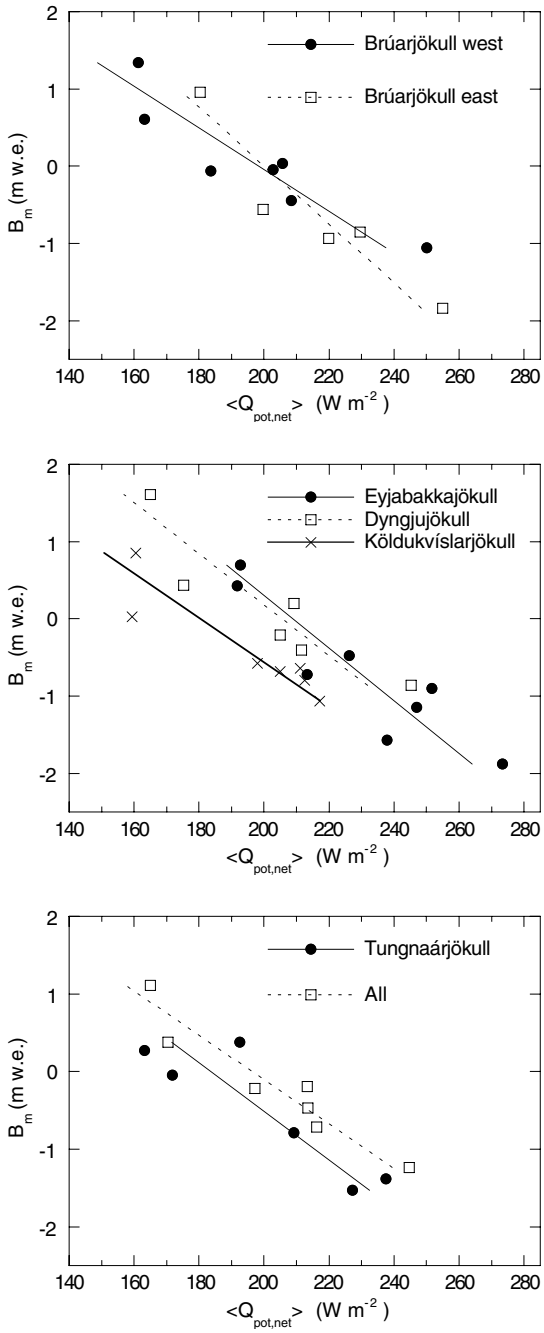


*Figure 4.10. <$Q_{pot,net}$>, integrated over part of the melting season (days 146- 242), as a function of the mean specific mass balance. The average <$Q_{pot,net}$> per day during the integration period is shown. All indicates the entire area where mass balance measurements were taken (i.e. all mentioned drainage basins).*

ting error in $B_{m,Q}$, tends to increase with precipitation. The total error in $B_{m,Q}$ ranges from 0.50 m w.e. (Köldukvíslarjökull) to 0.76 m w.e. (eastern Brúarjökull), which is two to three times as large as the error in the direct observations of $B_m$. It is interesting to note that, just like the error in $B_{m,Q}$, the overall range of annual mass balance tends to increase with mean annual precipitation. This range is 1.8 to 2.8 m w.e. for different parts of Vatnajökull (figure 4.10). The result is that for all drainage basins, the ratio between the error in $B_{m,Q}$ and the range of annual mass balance is nearly the same, namely 27 ± 3%. Hence, for all drainage basins of Vatnajökull, the satellite retrieval method can only positively detect annual changes in $B_m$ that are larger than 27 ± 3% of the range of annual mass balance.

The larger uncertainty in $B_{m,Q}$ also has implications for the possibility to estimate trends and averages. For example, the average $B_m$ (table 4.1) only differs significantly from zero (at the 95% confidence level) for Eyjabakkajökull. For all other drainage basins more annual measurements than presently available are required to make such a statement. The number of annual measurements that is needed for this statement ($n_y$) increases when the error in the mass balance measurement increases, as is the case when the satellite retrieval method is used. The observed variance in $B_m$ is partly due to natural variability and partly due to the measurement error in $B_m$. When we replace the measurement error in $B_m$ with the error in $B_{m,Q}$, we find that for all drainage basins $n_y$ becomes about 50% larger.

## 4.7 Conclusions

Remote sensing instruments are useful tools for observing glaciers and ice caps without the need to actually go there. The most obvious feature on the surface of glaciers and ice caps is the transition from ice to firn or snow, which can be successfully observed. However, this boundary is not always equal to the equilibrium line and hence not always related to the mass balance. This is often the case when the equilibrium line is located above its position of the previous year(s), because then firn is exposed, which obscures the equilib-

| Drainage basin | Correlation coefficient | Explained variance | Errors (in m w.e.) | | | | Annual precipitation (m) |
|---|---|---|---|---|---|---|---|
| | | | $B_m$ | Regression model | $\langle Q_{pot,net} \rangle$ | Total | |
| western Brúarjökull | 0.89 | 0.80 | 0.25 | 0.34 | 0.42 | 0.59 | 2.7 |
| eastern Brúarjökull | 0.94 | 0.87 | 0.25 | 0.34 | 0.63 | 0.76 | 2.9 |
| Eyjabakkajökull | 0.90 | 0.81 | 0.25 | 0.39 | 0.55 | 0.72 | 3.2 |
| Dyngjujökull | 0.90 | 0.81 | 0.25 | 0.37 | 0.51 | 0.68 | 2.4 |
| Köldukvíslarjökull | 0.92 | 0.85 | 0.25 | 0.25 | 0.35 | 0.50 | 2.1 |
| Tungnaárjökull | 0.87 | 0.76 | 0.25 | 0.51 | 0.46 | 0.73 | 2.3 |
| All | 0.95 | 0.91 | 0.25 | 0.24 | 0.47 | 0.59 | 2.7 |

*Table 4.2. Statistics for the linear $B_m$ - $\langle Q_{pot,net} \rangle$ regression model. The mean annual precipitation for each drainage basin is also shown. All indicates the entire area where mass balance measurements were taken (i.e. all mentioned drainage basins). The error in $\langle Q_{pot,net} \rangle$ is for each drainage basin averaged over the years, because the error associated with the analytical expression for $\langle Q_{pot,net} \rangle$ differs from year to year.*

rium line. Very small differences in albedo and texture between snow and firn make the equilibrium line hard, if not impossible, to detect in these years. This is especially true when no a priori information is available and one does not know where to expect the equilibrium line. Occasionally, the equilibrium line is visible as a secondary jump in albedo, but this is not the case in all years with a negative $B_m$ and not on all outlets. Apart from these problems the ice-snow transition is not always sharp and, depending upon glacier size and climatic setting, satellite and DEM resolution may limit the possibility to infer changes in ELA from satellite imagery (Demuth and Pietroniro; 1999). In one year there were too many clouds to find a suitable image of the end of the melting season.

These problems are not encountered when one studies the mean surface albedo of the entire drainage basin during the melting season, and not merely a boundary between two facies on a certain day. In years with a negative $B_m$ much relatively dark firn is present while little summer snowfall and high melt rates may also contribute to a darkening of the surface. In years with a positive $B_m$ no firn is exposed, more glacier ice is covered by snow, and summer snowfall may brighten the surface. The albedo feedback (which strengthens the correlation between $B_m$ and the albedo) is taken into account by weighting the mean surface albedo with the potential global radiation so that the mean net potential global radiation ($<Q_{pot,net}>$) is obtained. By using $Q_{pot,net}$, and not the global radiation at the surface, one does not need to know the average cloudiness. Consequently, the method can be applied easily to any ice cap and glacier in the world by using satellite data alone. $<Q_{pot,net}>$ is strongly related to surface melt and also depends on winter precipitation and melt earlier in the melting season. Because $<Q_{pot,net}>$ varies during the summer, the surface during the whole summer must be studied in order to extract all available information. An additional advantage of studying several images is that one does not need to find one cloud-free image of the end of the summer that is not disturbed by snowfall. We find that $<Q_{pot,net}>$, integrated over the melting season, is linearly related to $B_m$. Due to uncertainties in measurements and methods, this relation can only be used to detect changes in $B_m$ of at least 0.50 to 0.76 m w.e. (for different parts of Vatnajökull). This is two to three times larger than the uncertainty in the directly measured $B_m$, which implicates that more annual measurements are required to confidently estimate averages and trends when the satellite retrieval method is used.

The linear relations between $B_m$ and $Q_{pot,net}$ are based upon data from years with very positive and with very negative values of $B_m$. The drainage basins for which these relations are found have different hypsometries, climate settings (different amounts of precipitation) and states of mean balance. Therefore, we expect that yearly variations in $B_m$ of any ice cap or glacier can be estimated qualitatively with the method presented in this paper. The exact magnitude of yearly variations can only be deduced if the slope of the linear relation is known, and the value of $B_m$ only if both slope and offset are known. Therefore, the method can be used to estimate $B_m$ quantitatively for (parts of) Vatnajökull. Note, however, that there is no theoretical ground for the relation between the net potential global radiation and $B_m$ to be linear for all ice masses. It would be interesting to deduce this relationship for (part of) the Greenland ice sheet (with superimposed ice and slush zones) and for alpine glaciers (with steeper and more varying slopes). Unfortunately, NOAA images can only be used for ice sheets and ice caps of considerable size. For alpine glaciers images from satellites with a higher resolution (e.g. Landsat) must be used, but

these are much less frequently available and more expensive. This means that the method presented in this work is most suitable for fairly large ice caps and glaciers.

**Appendix 4A: BRDF over melting snow**

For a given surface type and solar zenith angle ($\theta_s$), the bidirectional reflectance (r) that is measured by the satellite sensor only depends upon satellite zenith angle ($\theta_v$) and satellite azimuth angle ($\varphi$) (relative to the solar azimuth angle). Bidirectional reflectance is related to surface albedo ($\alpha_{srf}$) through the anisotropic reflectance factor (f):

$$f(\theta_v, \varphi) = \frac{r(\theta_v, \varphi)}{\alpha_{srf}} \qquad 4.7$$

The parameterization that we use for f over melting snow and firn surfaces reads (Koks, 2001):

$$f(\theta_v, \varphi) = 1 + b_1\left(\cos\theta_v - 2/3\right) + b_2\theta_v^2\cos\varphi + b_3(\theta_v\cos^2\varphi - \pi/8) \qquad 4.8$$

The derivation of equation 4.8 is nearly the same as in Greuell and De Ruyter de Wildt (1999). The factors $b_1$, $b_2$ and $b_3$, which describe the dependence of f upon surface albedo and solar zenith angle, are given by

$$b_i = a_{i,0} + a_{i,1}\alpha + a_{i,2}\theta_s \qquad 4.9$$

where i is 1, 2 or 3 and $\theta_s$ must be given in degrees. Values of the coefficients $a_{i,0}$, $a_{i,1}$ and $a_{i,2}$ for Landsat Thematic Mapper band 2 and 4 are listed in table 4.3.

| i | TM2 | | | TM4 | | |
|---|---|---|---|---|---|---|
| | $a_{i,0}$ | $a_{i,1}$ | $a_{i,2}$ | $a_{i,0}$ | $a_{i,1}$ | $a_{i,2}$ |
| 1 | 0.920 | -0.735 | -0.00661 | 0.763 | -0.619 | -0.00776 |
| 2 | 0.100 | -0.159 | -0.00182 | 0.133 | -0.240 | -0.00243 |
| 3 | -0.157 | 0.236 | 0.000404 | -0.345 | 0.598 | -0.000388 |

*Table 4.3. Values of the coefficients $a_{i,0}$, $a_{i,1}$ and $a_{i,2}$ in equation 4.9. The coefficients are given for Landsat Thematic Mapper bands 2 and 4.*

# 5 Satellite-retrieval of mass balance: comparing SAR images with albedo images and *in situ* mass balance observations*

**Abstract**

We present an analysis of many ERS SAR images of Vatnajökull (Iceland) by comparing them with AVHRR images, mass balance observations and modeled firn stratigraphy. Summer SAR and AVHRR images both detect the surface firn line as a distinct boundary. Winter SAR images of Vatnajökull display sub-surface firn-ice transitions, but these do not correspond to the late summer surface firn line. We found no differences in backscatter between melting snow and firn and for most years no differences in reflectance either. Hence, the equilibrium line is mostly not visible when it lies above the firn line and we only identified it on SAR images for one out of nine years and on AVHRR images for only three years. For Vatnajökull, equilibrium line altitude is therefore not a particular good estimator of mean specific mass balance ($B_m$). However, for some drainage basins, mean firn line altitude during the melting season can be used to infer $B_m$. Unlike albedo images, SAR images do not display inter-annual variations of the signal within the accumulation area that are clearly related to $B_m$. Hence, for glaciers and ice caps like Vatnajökull that display no dry snow during the summer, the only advantage of SAR images over albedo images lies in the fact that they display the firn line irrespective of weather and illumination conditions.

## 5.1 Introduction

Glaciers and ice caps often lie in remote areas, are difficult to access and can have vast surface areas. Direct observation of the mean specific mass balance ($B_m$) and related quantities, such as the equilibrium line altitude (ELA) and accumulation area ratio, is therefore a time-consuming and often costly procedure. As a consequence, these quantities have been measured on relatively few glaciers worldwide. Larger parts of the cryosphere can be studied on a regular basis with satellite sensors. Østrem (1975) proposed that the often-found linear relation between $B_m$ and ELA can be used to infer $B_m$ by using satellite-derived ELA. In recent years much work has been devoted to inferring the snow line at the end of the melting season. Note that we define snow as being younger than one year and firn as being at least one year old, which implies that the equilibrium line equals the snow line at the end of the melting season (if there is no superimposed ice).

* Based on: De Ruyter de Wildt, M. S. and J. Oerlemans. Satellite-retrieval of mass balance: comparing SAR images with albedo images and *in situ* mass balance observations. *J. Glaciol.*, submitted.

Some authors successfully applied Østrem's method by using satellite albedo images (e.g. Rott and Markl, 1989) or Synthetic Aperture Radar (SAR) images (e.g. Demuth and Pietroniro, 1999), but the method often fails. This can occur for years when the equilibrium line lies above its position of the previous year(s). In such cases the snow line is sometimes visible (e.g. Rott and Markl, 1989), but often the difference in albedo ($\alpha$) between firn and snow of several months old is too small to be detectable (e.g. Rott and Markl, 1989; Hall et al., 1995; De Ruyter de Wildt et al., 2002b). De Ruyter de Wildt et al. (2002b) developed a method that does not suffer from this problem. The net potential shortwave radiation, defined as the net shortwave radiation at the top of the atmosphere, can be calculated from NOAA AVHRR albedo images. This quantity, integrated over the glacier surface and over the melting season, both depends on and influences summer melt. It also depends on winter mass balance and was found to be linearly related to $B_m$ for Vatnajökull (Iceland). Unfortunately, in some years high cloudiness limited the availability of albedo images and hence introduced uncertainty in this linear relationship.

Clouds do not pose a problem if SAR backscatter images are used. Backscatter ($\sigma_0$) images can display several boundaries, which correspond to surface or subsurface facies transitions. Microwaves penetrate through dry snow so the main signal over dry snow surfaces originates from subsurface material (e.g. Rott et al., 1985). The underlying material in the ablation area is ice, which produces less backscatter than the underlying firn in the accumulation area. Firn contains scattering elements such as ice structures and internal surfaces. SAR images acquired in winter or early spring can therefore be used to detect the approximate location of the firn line (e.g. Fahnestock et al., 1993; Hall et al., 1995; Partington, 1998; König et al., 2001b). When the surface is melting, the $\sigma_0$ signal is much lower and stems from the top few cm (e.g. Stiles and Ulaby, 1982) and only surface features can be observed. The boundary between dry and wet snow is detectable (e.g. Steffen et al., 1993), as well as the boundary between bare ice and wet snow or firn (e.g. Rott and Mätzler, 1987; Adam et al., 1997). Smith et al. (1997) also observed a fourth zone, marked by high backscatter over wet snow (phase 2 melt or P2), which is most likely caused by roughness due to suncups (Ramage et al., 2000). These four zones (dry snow, wet snow, metamorphosed wet snow and ice) were seen to move up-glacier and replace each other during the melting season. In spite of these observations, SAR images have been compared to *in situ* mass balance observations only a few times (e.g. Demuth and Pietroniro, 1999; Hall et al., 2000; König et al., 2001b), while a detailed comparison of radar images with albedo images and mass balance measurements from a number of years yet has to be made. From the latter two studies it appears that, just as is often the case for albedo images, the $\sigma_0$-signal cannot distinguish between snow and firn. Consequently, the snow line appears only to be visible on radar images when no firn is present at the surface.

For Vatnajökull (figure 5.1), one of the largest temperate ice caps in the world, a wealth of information is available with which SAR images can be analyzed and interpreted. Its mass balance has been regularly measured (e.g. Björnsson et al., 1998a) and recently a mass balance model was developed and calibrated to the conditions on the ice cap (De Ruyter de Wildt et al., 2002a). The mass balance measurements have been compared to NOAA AVHRR images (De Ruyter de Wildt et al., 2002b). *In situ* mass balance measurements, NOAA AVHRR images, and a long-term modeled mass balance series form a

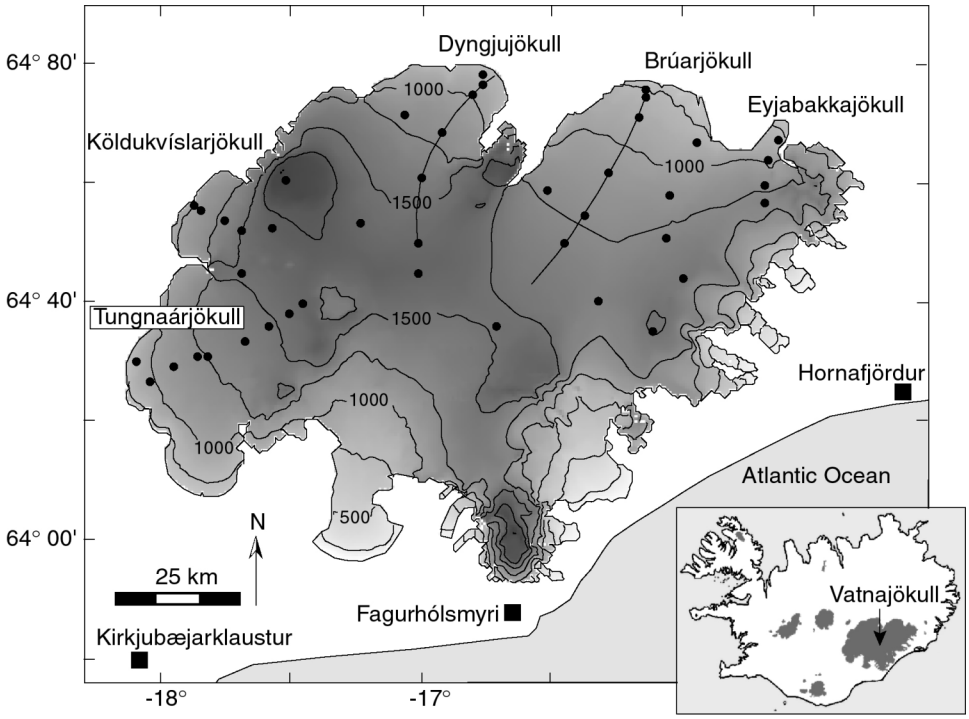


*Figure 5.1. Map of Vatnajökull, based on the Digital Elevation Model (DEM) used for image processing. The DEM has a horizontal resolution of 500 m. Height contours are shown for each 250-m interval. Indicated are the outlets where the mass balance has been regularly measured. The black circles represent sites where the mass balance has been measured. Over western Brúarjökull and over Dyngjujökull transects through measurement sites are shown.*

unique data set with which SAR images can be compared. In this paper, we compare these data sets with SAR images that were acquired during the same period as these data sets, i.e. the melting seasons of seven years in the 1990s. We also use a few images that were acquired in the winter during dry-snow situations. First we directly compare SAR images with AVHRR images to identify the glacier facies that are visible on SAR images. Then we reconstruct the stratigraphy of a part of Vatnajökull from measured and modeled mass balance values, in order to explain several boundaries and structures that are visible on the SAR images and on AVHRR images. On the basis of these investigations we discuss some possibilities of retrieving the mass balance from SAR images.

## 5.2 Data

### 5.2.1 ERS SAR images

The European Space Agency (ESA) launched the ERS-1 satellite in 1991 and the ERS-2 satellite in 1995. Both satellites carry a C-band (5.3 Ghz) SAR with vertical transmit and receive (VV) polarization. We use Precision Image ERS SAR data which are three-look (speckle-reduced) and which we calibrate and correct for the SAR antenna pattern and range-spreading loss (Laur et al., 1998). The $\sigma_0$ signal is dimensionless and given in dB (i.e. on a logarithmic scale). The horizontal resolution is 33 m in range and 30 m in azimuth while the pixel size is 12.5 m. The ERS scenes are very large (130 MB in binary format) and therefore unmanageable, so we scale up the pixel size with a factor of 10 (up to a pixel size of 125 m). In view of the fairly large size (8200 $km^2$) and low surface slopes (2.8° on average) of Vatnajökull, this has no consequences for the results. ESA provides the images' horizontal locations with an accuracy of 100 m in range and 200 m in azimuth. We purchased images that were acquired during the melting seasons of 1993, 1995, 1996, 1997 and 1998, which are years with positive, negative and near-neutral mean specific mass balances. Typically, the time interval between subsequent images is two to three weeks. Most images display only a part of Vatnajökull so the number of images varies per drainage basin. For each of these five years, we have six to ten images for the drainage basins Brúarjökull, Dyngjujökull, Köldukvíslarjökull and Tungnaárjökull (figure 5.1). Furthermore, for 1991 and 1994 we have one image acquired at the end of the melting season, and we have one additional image for each of the winters of 1992/1993, 1993/1994 and 1998/1999.

### 5.2.2 NOAA AVHRR images

We purchased NOAA AVHRR images from the Dundee Satellite Receiving Station in the U.K. The images were acquired during the melting seasons (April - September) of the years 1991-1999 inclusive. The horizontal resolution at nadir is 1.1 km. In the first four years, the NOAA-11 satellite provided the data. From 1995 onwards the images were acquired by the NOAA-14 satellite. Because Iceland lies in the north Atlantic Ocean, where storm activity is high, the skies are often overcast and most of the images display some clouds. It was therefore not always possible to find cloud-free images for the end of the melting season (e.g. in 1994 and 1999). We found nine to fifteen images for each melting season with a typical time interval of two weeks between images. Nearly all images were acquired near solar noon when irradiance was high. The process of retrieving the surface albedo from the images has been discussed in detail elsewhere (De Ruyter de Wildt et al., 2002b), which is why we restrict ourselves here to a short description of the successive processing steps:

- Clouds are discriminated from snow and ice by making use of the reflective and thermal differences in AVHRR channel 3 (3.5-3.9 μm) and the thermal differences in

channel 4 (10.5-11.5 μm) that often, but not always, exist. Not all clouds are detected in this way, so we had to check the images for errors manually. A convenient way of doing this is to compare subsequent images and look at textural characteristics.

- We apply a geolocation to each image by comparing the images to a Digital Elevation Model (DEM), depicted in figure 5.1. The horizontal resolution of the DEM is smaller than the AVHRR pixel size, namely 500 m. For most images we were able to locate the ice margin and features like mountain peaks and steep ridges with an accuracy of one pixel. The accuracy of the geolocation for a few images with a large satellite viewing angle is estimated to be two pixels.
- Measured radiation intensities are calibrated with the calibration formulas of Rao and Chen (1995) and Rao and Chen (1999) for the AVHRR instruments aboard the NOAA-11 and NOAA-14 satellites, respectively. These coefficients take instrument drift into account. The resulting radiances are converted into planetary albedos.
- We use a radiative transfer model (Koelemeijer et al., 1993) to convert the planetary albedos into surface albedos. This model takes Rayleigh scattering and attenuation by ozone and water vapor into account but neglects the effect of aerosols. Because the results are not very sensitive to the atmospheric profiles (Reijmer, 1997), we use the standard Sub Arctic Summer Profile of McClatchey et al. (1972) as input.
- We employ an empirical expression to convert the surface narrowband albedos in AVHRR channels 1 and 2 into broadband albedos. This expression (De Ruyter de Wildt et al., 2002b; W. Greuell, personal communication) is based on many (8,000) point measurements made simultaneously in AVHRR channels 1 and 2 and over the entire solar spectrum (Greuell et al., 2002). The measurements were made over a broad range of surface types, ranging from dirty glacier ice to melting snow and having broadband albedos between 0.05 and 0.80.
- To correct for the anisotropic nature of reflection at snow surfaces, we apply an empirical parameterization (Koks, 2001), which is based on measurements over melting snow of two to three weeks old, and is valid for a broad range of solar zenith angles (15.9° - 65.5°). During the summer, virtually all surface snow of Vatnajökull melts and becomes metamorphosed, so the parameterization is likely to be valid for the average summer conditions on Vatnajökull. For glacier ice no usable parameterization is available.
- In the above, the fluxes are calculated with respect to a horizontal plane. If the surface is inclined, the fluxes through a plane parallel to the surface differ from those through the horizontal plane and a correction needs to be applied to obtain the surface albedo. We calculate the surface albedo with the expression of Knap et al. (1999).

### *5.2.3 Mass balance observations*

The mass balance of Vatnajökull has been measured with good spatial resolution since 1992 (Björnsson et al., 1997, Sigurdsson, 1997; Björnsson et al., 1998a, b, c, 1999; O. Sigurdsson, personal communication). The data have mainly been obtained over the drainage basins of Eyjabakkajökull, Brúarjökull, Dyngjujökull, Köldukvíslarjökull and

Tungnaárjökull (figure 5.1). For Eyjabakkajökull, data from 1991 are also available. Most measurements were taken at the end of September or the beginning of October. On each outlet, the mass balance has been measured along one or two profiles that capture the altitudinal variation. Because most of Vatnajökull is quite flat, the profiles can be used together with a few additional measurement sites to describe the lateral variation. We obtain the mean specific balances of the drainage basins and the ELAs by interpolating between the measurement sites. For this interpolation, we developed an algorithm that takes vertical gradients in the mass balance into account, even when these are not resolved by the measurement sites. A DEM is needed for this feature to work. For each grid point of the DEM, the algorithm determines the n closest measurement sites within 500 m in altitude from the grid point. Then, because of the limited height differences, a linear relation between mass balance and altitude is found for the n measurement sites, with which the mass balance at the grid point can be calculated. To smooth discontinuities in the resulting mass balance field, the contribution of each measurement site is weighted with the inverse of its distance to the grid point. The resulting values of $B_m$ are not very sensitive to the value of n. We therefore use a value of 6, which is the lowest value that gives smooth mass balance fields. Table 5.1 displays the resulting values of $B_m$. The data clearly include years with a highly positive $B_m$ (1992, 1993) and years with a highly negative $B_m$ (1997, 1998). We estimate the uncertainty in $B_m$ to be 0.25 m w.e.

### 5.3 Interpretation of radar boundaries

A first and direct way to interpret the different $\sigma_0$ signatures observed on the SAR images of Vatnajökull, is to make a scatter plot of $\sigma_0$ against $\alpha$ (figure 5.2). In this plot we clearly see three clusters of data points, representing three kinds of surface facies. Dry snow has high $\alpha$ and high $\sigma_0$ signatures. The difference between dry snow lying directly on top of glacier ice and dry snow lying on firn is small (3 to 4 dB) and the two groups merge in figure 5.2

| year | western Brúarjökull | eastern Brúarjökull | Eyjabakka-jökull | Dyngju-jökull | Köldukvís-larjökull | Tungnaár-jökull | All |
|---|---|---|---|---|---|---|---|
| 1991 | | | -0.90 | | | | |
| 1992 | | | | | 0.81 | 0.35 | |
| 1993 | 1.32 | 0.89 | 0.69 | 1.58 | | 0.23 | 1.16 |
| 1994 | 0.55 | | 0.42 | 0.36 | 0.03 | -0.11 | 0.31 |
| 1995 | 0.22 | | -0.48 | 0.04 | -0.64 | | -0.31 |
| 1996 | -0.04 | -0.76 | -0.88 | -0.21 | -0.68 | | -0.54 |
| 1997 | -1.04 | -1.79 | -1.88 | -0.85 | -1.07 | -2.18 | -1.30 |
| 1998 | -0.46 | -0.94 | -1.57 | -0.53 | -0.80 | -1.53 | -0.77 |
| 1999 | -0.09 | -0.56 | -0.72 | | -0.58 | -0.99 | -0.26 |

*Table 5.1. Mean specific mass balance of various drainage basins of Vatnajökull (in m w.e.). The values were obtained by interpolation. The weighted mean for the whole northwestern part of Vatnajökull (all) is shown when the mass balance was measured over the largest part of this area.*

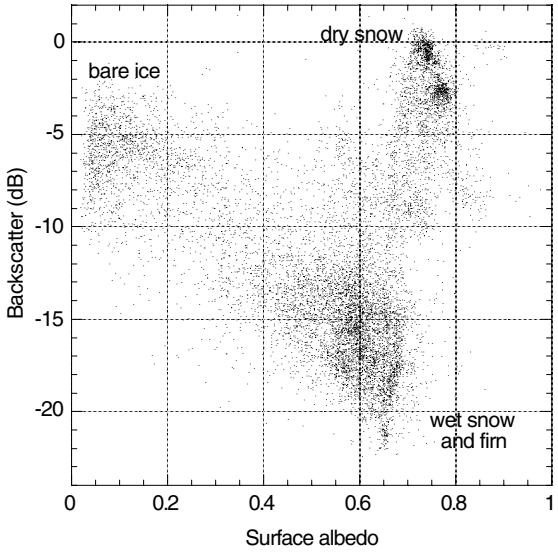


*Figure 5.2. Radar backscatter against satellite-derived surface albedo. Each point represents an AVHRR pixel; for this plot the backscatter images have been resampled up to the same resolution as the AVHRR images (1.1 km). The maximum time gap between radar and albedo images used to make this plot is three days. Sixteen of such pairs were found, distributed randomly over spring and summer of five years.*

(note that the two sub-clusters of dry snow in this figure represent two different days, not the difference between ice and firn). Melting snow and firn have somewhat lower $\alpha$ values, but drastically lower $\sigma_0$ values. A third cluster represents bare glacier ice with much lower $\alpha$ values and rather high $\sigma_0$ values. For melting surfaces, there is a tendency for higher $\sigma_0$ values at lower $\alpha$ values (i.e. when the snow is wetter and/or grows older and becomes more metamorphosed). This corresponds to earlier observations that increasing surface wetness and roughness produces higher backscatter (e.g. Jezek et al., 1993; Rott and Davis, 1993).

Figure 5.2 shows no cluster of P2 melt facies, consisting of roughened melting snow with high $\sigma_0$ (>12 dB) as Smith et al. (1997) and Ramage et al. (2000) observed. Only five out of 43 SAR images of Vatnajökull with melting surfaces display wet snow with high $\sigma_0$, but for these images no simultaneous AVHRR images are available. Figure 5.3 shows two of these five images. All zones in these images follow the height contours of the ice cap (figure 5.1). The lowermost zone is bare glacier ice, as confirmed by AVHRR images acquired at most one week later. The uppermost zone (only in figure 5.3a) lies in the highest part of Vatnajökull, approximately above the 1600 m contour. From the daily mean temperature in Kirkjubæjarklaustur and assuming a lapse rate of 6°C/km, we find the daily mean 0°C isotherm to be at 1700 m. The correspondence of these two heights and the high $\sigma_0$ values suggest that the uppermost zone represents dry snow. Zones I, II and III must consist of melting snow and/or melting firn. Zone I has low backscatter and corresponds to

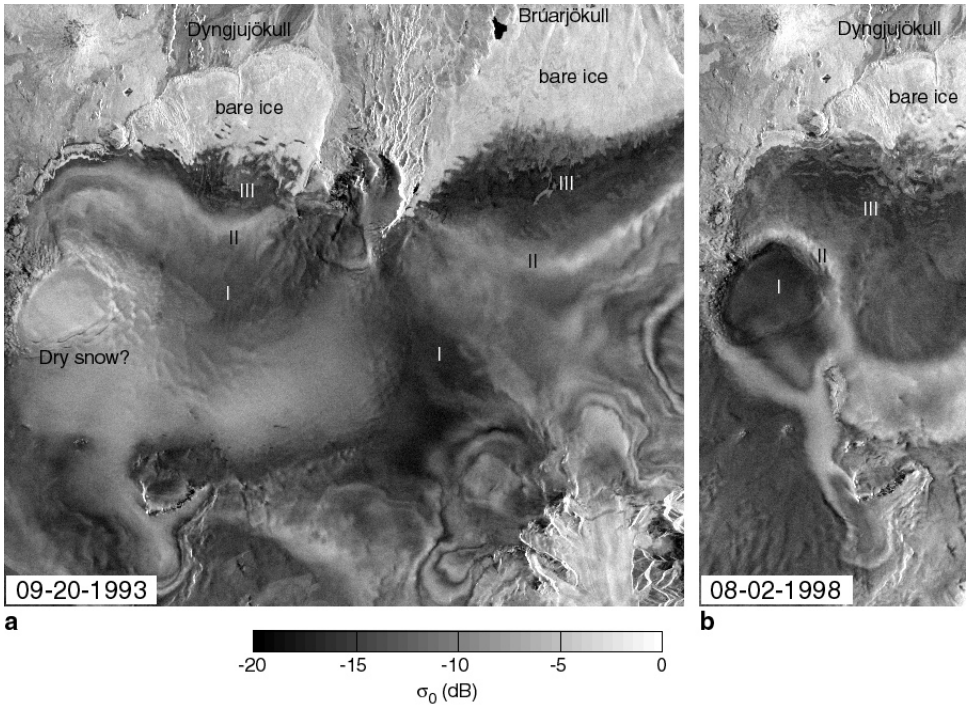


*Figure 5.3.ESA ERS $\sigma_0$ images of part of Vatnajökull, acquired on September 20th, 1993 (a), and acquired on August 2nd, 1998 (b). Latin numerals indicate different zones of surface facies.*

the initial-melt zone ("M") of Smith et al. (1997). Zone II has high $\sigma_0$ (-6 to -10 dB), but in both images it is bounded on both sides by zones of low $\sigma_0$. If the high backscatter in zone II is caused by roughening elements like suncups (Ramage et al., 2000), then these must be absent in zone III. In this respect zone II differs from the P2 zone found by Smith et al. (1997), which lies directly above the bare-ice zone. In any case, most images do not display zone II and Hall et al. (2000), who studied many SAR images of Hofsjökull (Iceland), do not mention such a zone either. The reason for this absence may be the regular occurrence of snowfall in the accumulation area during the summer, which prevents the formation of suncups.

For further interpretation of the different boundaries present in the SAR images of Vatnajökull, we compare $\sigma_0$ profiles with $\alpha$ profiles and, following König et al. (2001b), with modeled stratigraphy. We do so for the western part of Brúarjökull, one of the large northern outlets, because this outlet mostly displays a rather sharp firn line. On other outlets the situation is more complicated with a gradual and patchy firn-ice transition, which makes it difficult to compare SAR images with model results.

### 5.3.1 Stratigraphic modeling

To model the stratigraphy we used mass balance observations (since 1992) and mass balance values (from 1960 until 1992) obtained with the mass balance model of De Ruyter de Wildt et al. (2002a), which was especially constructed for Vatnajökull. It describes the energy fluxes between atmosphere and glacier, which are tuned with *in situ* measured data (Oerlemans et al., 1999), in a detailed way. The most important model specifications are:

- Temperature in the katabatic surface layer is related, but not equal, to the temperature in the free atmosphere just above the surface layer (in the surface layer temperature is mostly lower and temperature variations are smaller than in the free atmosphere).
- Incoming longwave radiation is a function of temperature in the free atmosphere, which is justified by the relatively thin katabatic layer over Vatnajökull.
- Sensible heat flux is a function of temperature in the katabatic layer.
- Snow albedo depends upon the number of days since the last snowfall
- Ice albedo depends upon location and varies from very low in the northwest (0.10 due to volcanic ash layers) to 0.30 at some locations in the south and southeast.
- Subsurface processes, such as refreezing of melt water, are neglected and whenever the surface energy flux is positive, the surface is assumed to be at the melting point ("zero-degree assumption"). For a temperate ice cap like Vatnajökull, this is a reasonable assumption.
- Free-air temperature and vapor pressure are assumed to be always horizontally (but not vertically) homogeneous over the ice cap. Meteorological data show that this is mostly the case. Cloudiness and relative variations in precipitation are also assumed to be horizontally homogeneous. This allows us to force the energy balance over the entire ice cap with data from one meteorological station.
- The mean spatial distribution of precipitation over Vatnajökull is not well known, which is why we use this variable to calibrate the model to observations of the mass balance (Björnsson et al., 1997, 1998a, b, c, 1999). These observations were mainly made over the central and northwestern parts of the ice cap (i.e. the drainage basins of Tungnaárjökull, Köldukvíslarjökull, Dyngjujökull and Brúarjökull). Precipitation data from coastal weather stations in the south and southeast are available to prescribe a spatial distribution.

Daily mean temperature, humidity and cloudiness measured at Kirkjubæjarklaustur (figure 5.1) are used to drive the model. It was found that the observed mass balance is best simulated when the model is driven with the precipitation from Fagurhólsmyri (figure 5.1).

We modeled the stratigraphy at many points along the transect over western Brúarjökull (figure 5.1) which enables us to plot the stratigraphy as a function of surface elevation. We do not take ice flow into account, because Brúarjökull is in the quiescent phase of its surging cycle; the last surge took place in 1963 (about 4 km; Sigurdsson, 1998). Furthermore, the surface slope of Brúarjökull in the vicinity of the equilibrium line is very low (0.5° to 1°), meaning that mass is transported to lower surface elevations only very slowly.

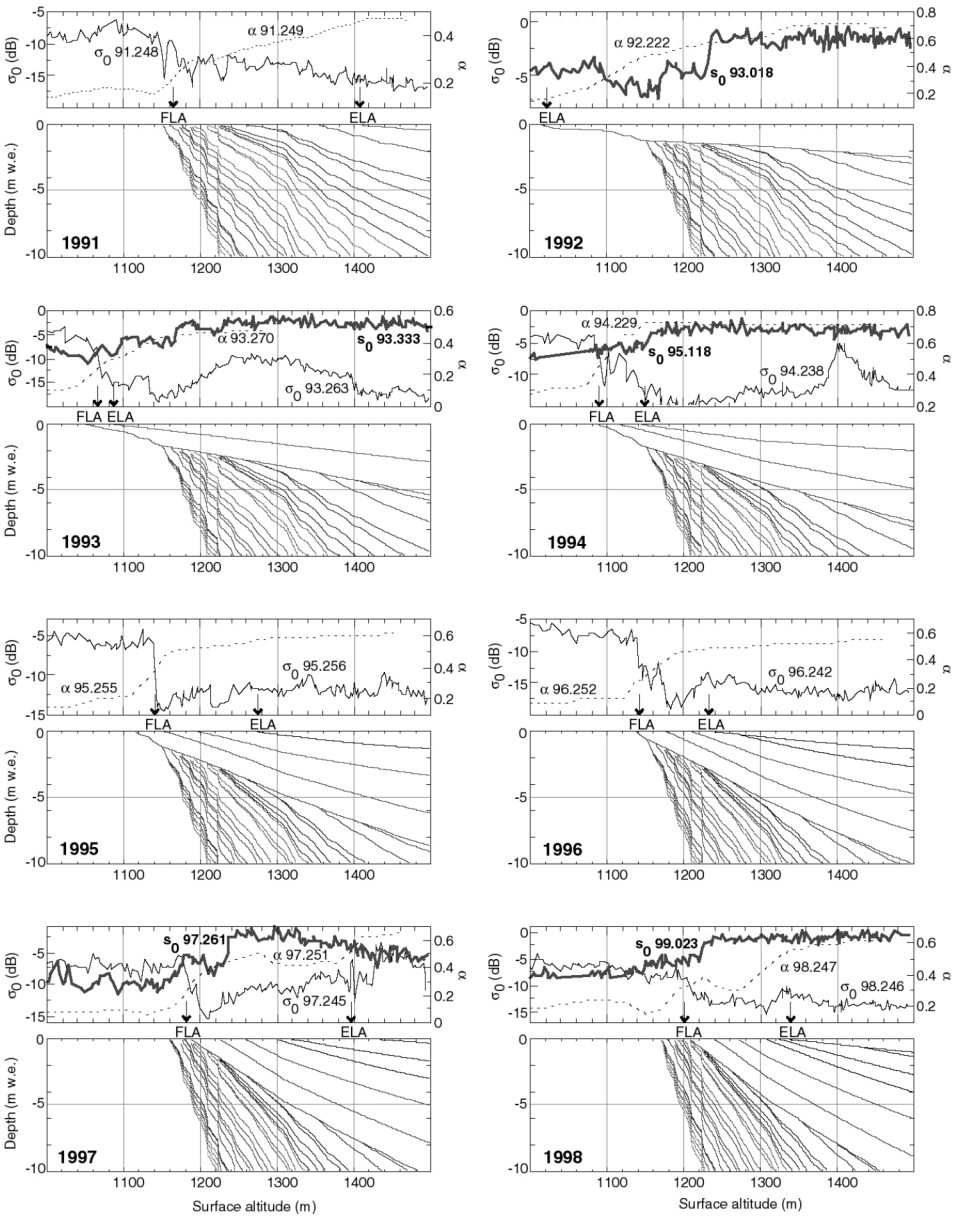


*Figure 5.4. Modeled stratigraphy, backscatter profiles ($\sigma_0$, solid lines) and albedo profiles ($\alpha$, dashed lines) along the transect shown in figure 5.1. For each of the years 1991-1998, annual layering at the end of the melting season (September 21$^{st}$) is shown. The $\sigma_0$ and $\alpha$ profiles are named by year and day of the year. For each year the profiles that display the highest firn line are shown. Some additional $\sigma_0$ profiles acquired during freezing conditions are shown as bold lines. 10 m in surface altitude approximately corresponds to 800 m in horizontal distance.*

### 5.3.2 Comparison of SAR data with AVHRR data and stratigraphy

Figure 5.4 compares backscatter profiles, albedo profiles, and modeled stratigraphy along a flow line of western Brúarjökull. Note that in each stratigraphy plot, the equilibrium line is given by the lower boundary of the most recent annual layer (the uppermost layer). First of all we notice that near the end of the melting season, $\sigma_0$ and $\alpha$ images display the same Firn Line Altitude (FLA). This is the case in all years (note that we have no $\sigma_0$ images for 1992), although in 1998 there is a small difference that may be due to a geolocation error. In all years except 1992, the equilibrium line lies above the firn line and cannot be seen on the $\sigma_0$ profiles. The $\alpha$ profiles only display it for the years 1992, 1997 and 1998. In 1993 and 1994, both years with a positive mean specific mass balance, the ELA is obscured by firn from 1992, although in 1993 the firn line and the snow line lie closely together. From 1992 till 1996 the late-summer firn line was formed by relatively young firn from 1992. In September 1991, 1997 and 1998 the firn line corresponded to annual layers of 15 to 20 years old (between 1150 and 1180 m). Note that annual layer thickness is given in m w.e. so the compaction of firn into ice is not taken into account. On a temperate ice cap like Vatnajökull the compaction process is complicated by melting and strong metamorphism of firn layers, which is very difficult to model. On other temperate glaciers, the firn-ice transition occurs in layers of 4 to 13 years old, at depths of 13 to 32 m (Paterson, 1994). In 1991, the firn line on Vatnajökull lay at a slightly lower elevation than in 1997 and 1998, which is caused by melting of the lowermost surface firn layers in these two years.

Only at the end of the melting season of 1992, all firn was covered by snow and for this year it should be possible to detect the snow line on satellite images. Unfortunately, we have no radar images for this year and we found no cloud-free AVHRR images for the end of the melting season either. Images from the winter and spring of 1993 might also display the equilibrium line from 1992, but this appears not to be the case (figure 5.4, panel for 1992). Near the end of August 1992, there was a considerable amount of snowfall, which contributed to the low ELA of 1992 (Björnsson et al., 1998). This snow may have undergone some melting in September and October, but the $\sigma_0$ signal can still penetrate several meters through refrozen stratified snow and firn (e.g. Mätzler, 1987). Therefore, just above the equilibrium line from 1992 the main signal seems to have come from the underlying ice and it seems unlikely that the late-summer snow can be distinguished from winter snow on the images from the winter and spring of 1993. The same appears to be the case for the two following years. Winter images from late November 1993 (day 333, see panel for 1993) and April 1995 (day 118, see panel for 1994) do not display the late summer firn line. In these winters, as in the winter of 1992/1993, the firn pack remained shallow below a surface altitude of about 1150-1180 m. Below this altitude the $\sigma_0$ signal was only partially influenced by the firn and thus reached the underlying ice. Therefore, near the late-summer firn line, the effect of the firn seems to have been very small. Images acquired during freezing conditions often display two boundaries on western Brúarjökull, for example, the SAR images from January 18$^{th}$, 1993 (figure 5.5a) and from January 23$^{rd}$, 1999 (figure 5.6a). Figure 5.4 shows in red all $\sigma_0$ profiles from images that were acquired during freezing conditions. These images display high backscatter values and correspond to low daily mean temperatures in Kirkjubæjarklaustur. The upper boundary lies between 1230 and

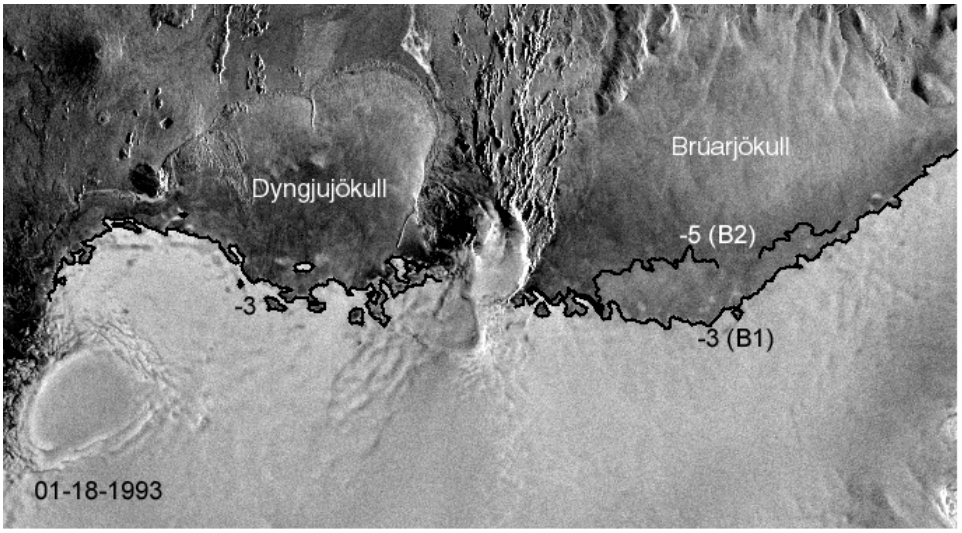


**a**


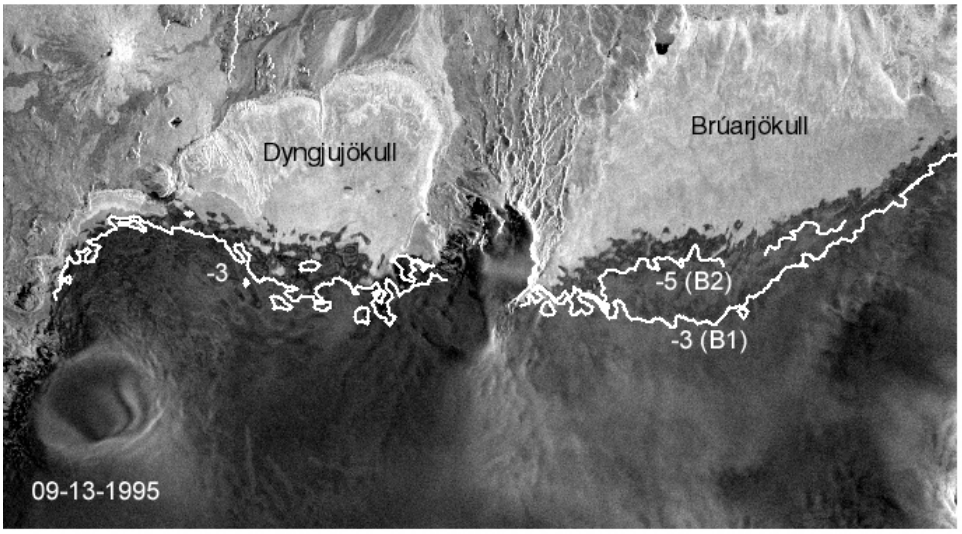


**b**


*Figure 5.5. ESA ERS $\sigma_0$ images of the northern part of Vatnajökull, acquired on January 18th, 1993 (a), and acquired on September 13th, 1995 (b). The latter image is compared with $\sigma_0$ boundaries from plot a (labeled B1 and B2).*

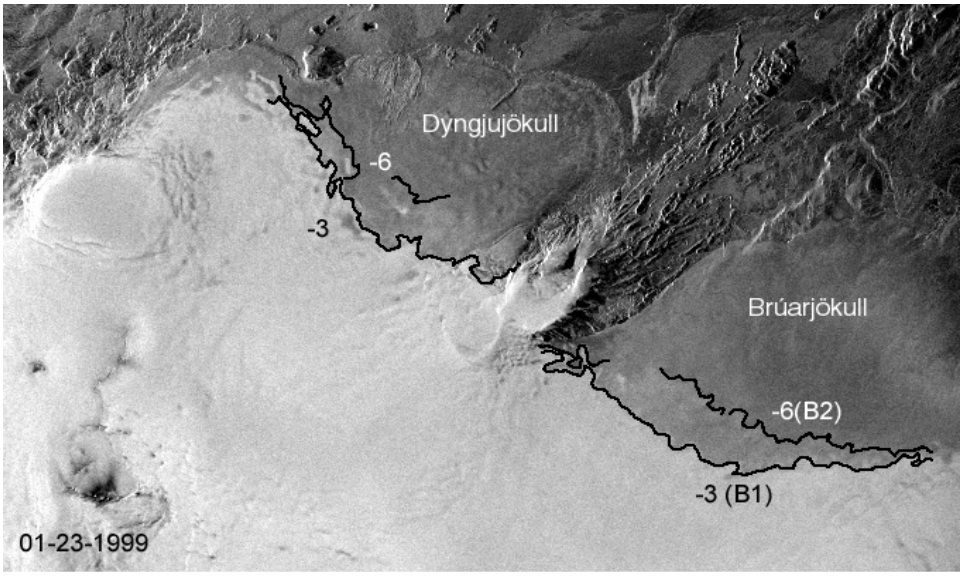


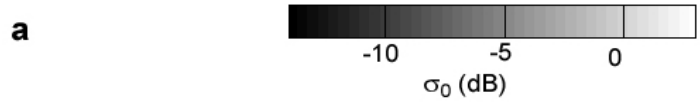


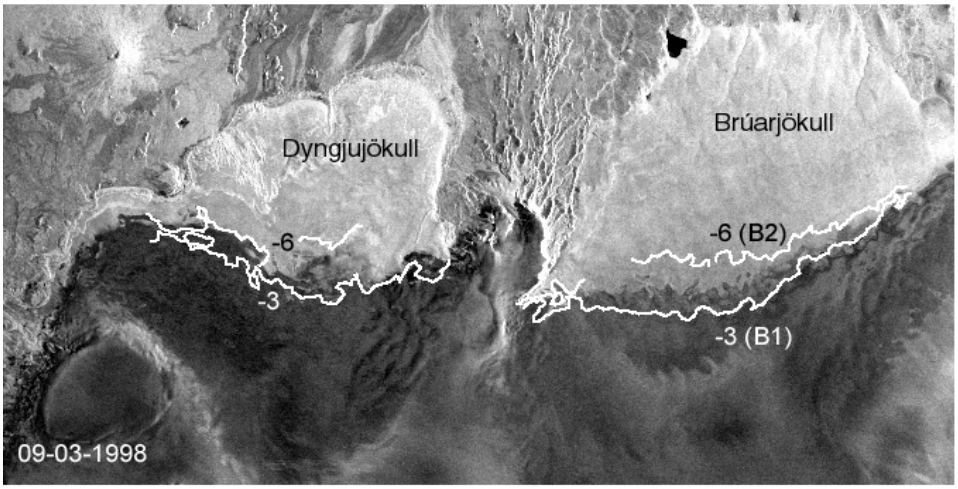



*Figure 5.6. ESA ERS $\sigma_0$ images of the northern part of Vatnajökull, acquired on January 23rd, 1999 (a), and acquired on September 3rd, 1998 (b). The latter image is compared with $\sigma_0$ boundaries from plot a (labeled B1 and B2).*

1240 m (hereafter called B1) and the lower boundary between 1160 and 1190 m (hereafter called B2). In some images, B1 is the most obvious boundary, but B2 is clearer in others. Both boundaries most likely correspond to subsurface transitions because they are not visible on late summer images (figures 5.5b and 5.6b), which only display the surface firn line. B1 did not noticeably change position between 1993 and 1999 (unlike the late summer firn line) and lay at a higher elevation than the late summer firn line. B2 also lay above the late summer firn line of 1995 but below the late summer firn line of 1998. Hence, both wintertime images (figures 5.5a and 5.6a) do not display the late-summer surface firn line. All stratigraphy plots in figure 5.4 show an increase in subsurface firn age close to the altitude of B1 (1225 m). This increase most likely corresponds to an increase in density and 1220-1240 m seems to be the lowest altitude where, during freezing conditions, the SAR sensor only 'sees' firn and no ice. Just below this altitude, the firn-ice transition lies closer to the surface and the $\sigma_0$ signal probably stems both from ice and from the overlying firn. The winter $\sigma_0$ profiles in figure 5.4, panels 1993 and 1995, do not show B1. On these images, it may be obscured by the thick pack of relatively recent snow and firn. Note that the stratigraphy plots do not display fresh winter snow, which overlies the displayed stratigraphy on wintertime images. Furthermore, the stratigraphy in figure 5.4 is displayed in m w.e. so the actual annual layers are thicker, especially the young layers.

Figures 5.5 and 5.6 show that the situation on Dyngjujökull is more complicated than on western Brúarjökull. On Dyngjujökull, there is a transition zone, rather than a line, between firn and ice. Only one wintertime $\sigma_0$ boundary is clearly present (corresponding to B1 on western Brúarjökull). When we compare this boundary to the late summer firn lines, the results resemble those of western Brúarjökull: in both years it lay above the late summer firn line.

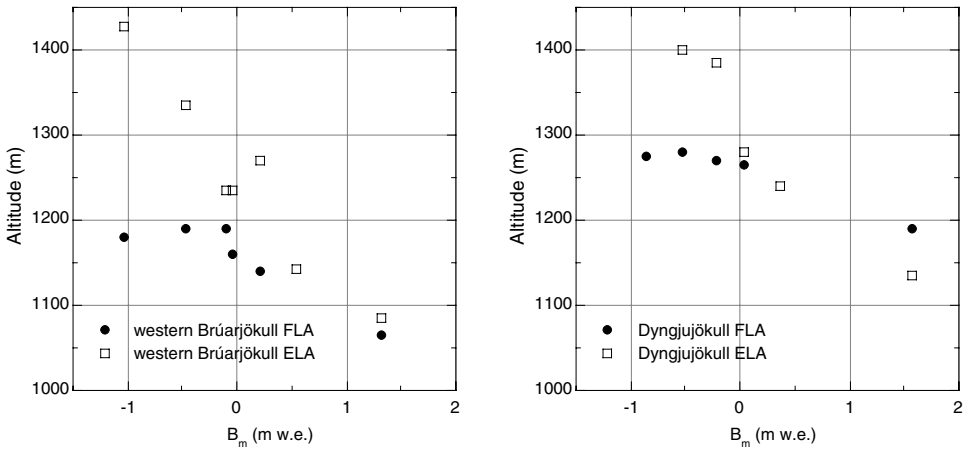


*Figure 5.7. Firn Line Altitude (FLA) at the end of the melting season and Equilibrium Line Altitude (ELA) as a function of the mean specific mass balance for western Brúarjökull and Dyngjujökull. Both radar and albedo images were used to derive FLAs. ELAs are derived from the mass balance measurements.*

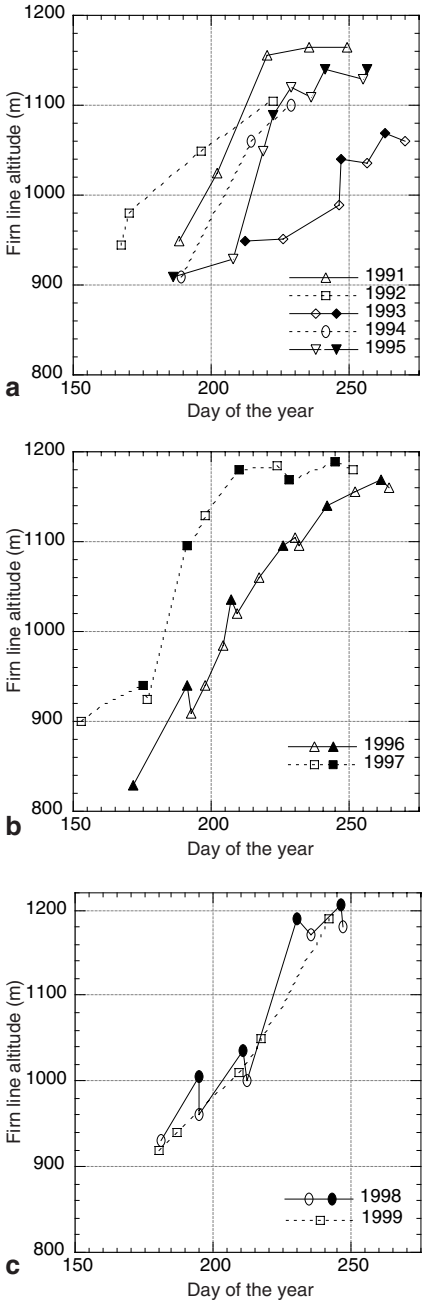


*Figure 5.8. FLA along the transect shown in figure 5.1 (western Brúarjökull) as a function of the day of the year. Both backscatter images (solid symbols) and albedo images (open symbols) were used to obtain FLAs. Each FLA was manually determined as the altitude at which the change in backscatter or albedo was largest. Low FLAs in the latter part of the summer, indicative of summer snowfalls, are not shown.*

### 5.4 Mass balance retrieval

SAR images can be used to trace changes in the long-term surface firn line, but are of limited use for annual detection of the equilibrium line. Figure 5.7 shows that, whereas the ELA is linearly related to $B_m$, the FLA is not related to $B_m$ for negative values of $B_m$. However, $B_m$ may be related to other quantities that can be detected on SAR images. Recent work (De Ruyter de Wildt et al., 2002b) has shown that the average surface albedo correlates well with $B_m$, whereas melting snow and firn tend to have higher $\sigma_0$ values when the albedo is lower (figure 5.2). In addition, figure 5.8 shows that in years with a positive mass balance (e.g. 1993), the firn line rises more slowly and later in the melting season than in years with a negative mass balance (e.g. 1997). The snow line position contains information about the accumulation and melt history, as long as the snow line is located below the equilibrium line in previous years. This is always the case during the first part of the melting season and for some years also at the end of the melting season. These observations suggest that during the melting season, the average $\sigma_0$ ($\langle\sigma_0\rangle$) over the glacier surface may be lower (more negative) in years with a positive mass balance than in years with a negative mass balance. This can of course only be the case when dry snow and firn, and the P2 facies are excluded from the analysis, as these facies disturb the linear relation between $\sigma_0$ and $\alpha$. Figure 5.9 shows that for western Brúarjökull, $\langle\sigma_0\rangle$ generally increases during the summer, corresponding to increasingly higher firn lines and/or snow and firn surfaces that are increasingly wet and rough. Only in 1993 there was no obvious increase and $\langle\sigma_0\rangle$ remains relatively low during the summer. In this year, the summer was cold with regular snowfalls. In general, the signal strength changes with surface wetness and

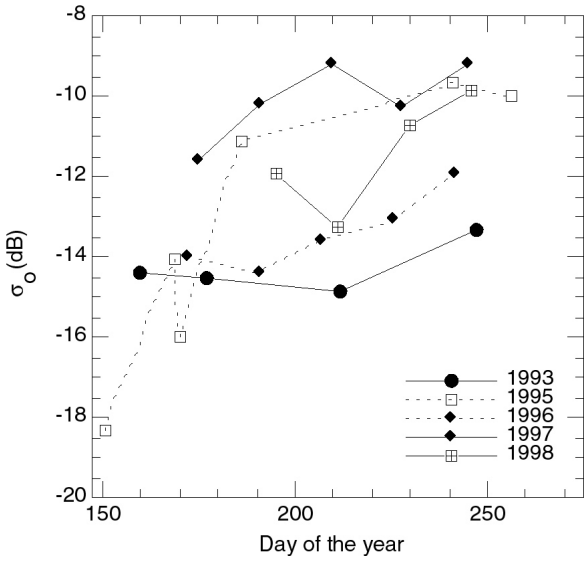


*Figure 5.9. Average $\sigma_0$ over western Brúarjökull as a function of day of the year, for each of the ERS SAR images. Only images that do not display dry snow and firn were used.*

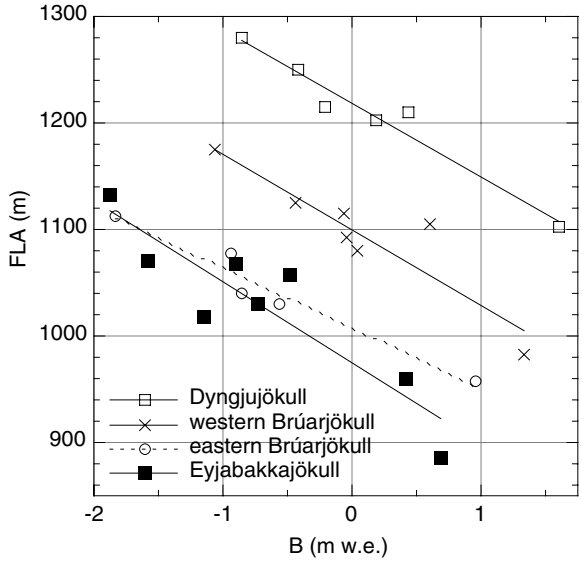


*Figure 5.10. Mean FLA during the second half of the melting season (day 200-264) as a function of the mean specific mass balance for western Brúarjökull, Dyngjujökull and Eyjabakkajökull. Both radar and albedo images were used to derive the FLA.*

roughness, which both are highly dependent on temporal circumstances. This is shown, for example, by the data from 1998. Also, in 1995 $\langle\sigma_0\rangle$ was quite high in the summer, while $B_m$ had an intermediate value (Table 5.1). For this year, no suitable images are available for a large part of the summer and the high $\langle\sigma_0\rangle$ values may not be representative. By interpolating $\langle\sigma_0\rangle$ between the successive images, we can compute the mean value of $\langle\sigma_0\rangle$ over the summer. We do so for the period from day 195 till day 245, which is the longest period for which $\langle\sigma_0\rangle$ values are available in our data set. We then find a correlation coefficient of 0.72 for $\langle\sigma_0\rangle$, averaged over the summer, and $B_m$. There is no significant correlation between $\langle\sigma_0\rangle$ and $B_m$ for Dyngjujökull and Köldukvíslarjökull.

Figure 5.8 shows that the course of the FLA during the summer varies per year. A simple way to quantify this is to compute the average FLA during the melting season. We do this for the second half of the melting season (days 200 – 264), because in the year with the lowest $B_m$ (1993), no ice was visible and hence no firn line existed before day 200. Dips in the FLA in the later part of the summer, indicative of summer snowfalls, are not used. These are often highly temporal events that are not representative of the previous and following weeks. When no images for the end of the melting season are available (e.g. 1992 and 1994), we linearly extrapolated the FLA from FLAs earlier in the melting season. In such cases the highest FLA from other years forms an upper limit to the extrapolated FLA. Figure 5.10 shows that the average FLA during the second half of the melting season correlates well with $B_m$ on several drainage basins. We have no ERS images for 1994 and, due to clouds, only a few AVHRR images from which the FLA can be derived. For this year, there is an outlyer for western Brúarjökull ($B_m$=0.55) and we expect that the correlation

would be better if we had more satellite-derived FLAs for this year. In view of the correlation between the mean albedo and $B_m$ (De Ruyter de Wildt et al., 2002b), the correlation between $B_m$ and the average FLA was to be expected. The mean albedo over the ice cap depends both on the albedo of the snow- and firn-covered area, and on the position of the firn line (because the firn line corresponds to a large change in albedo).

## 5.5 Discussion and conclusions

We have analyzed many ERS SAR images by comparing them with AVHRR images, mass balance observations, and modeled firn stratigraphy. Both SAR and AVHRR images detect the surface firn line as a distinctive boundary because the reflective and backscattering properties of melting snow and firn are different from those of bare glacier ice. However, we found no differences in backscatter and mostly no differences in reflectance between snow and firn. This implies that the equilibrium line can mostly not be detected when surface firn is present below the equilibrium line. As a consequence, the retrieval of the mass balance through detection of the equilibrium line is often not possible. During nine subsequent years, the equilibrium line of western Brúarjökull could be detected on SAR images for only one year and on AVHRR images for only three years.

Apart from the boundary between ice and melting snow and firn, SAR images can detect several boundaries that are not visible on albedo images. The intensity of the $\sigma_0$ signal is highly sensitive to the liquid water content of snow, which makes it possible to detect the extent of surface melt (e.g. Steffen et al., 1993). For Vatnajökull this is of little use because all snow quickly starts to melt in late spring. A boundary between newly melting snow and roughened melting snow has been found elsewhere (Smith et al., 1997; Ramage et al., 2000). Although it may be present on some SAR images of Vatnajökull, most images do not display such a boundary. All of the boundaries mentioned above are surface boundaries. Sub-surface boundaries can be detected when the surface is not melting, because then microwaves can penetrate several meters into the snow and scatter on subsurface structures. This is for example the case on images that display a dry winter snow pack. These images often display a distinctive boundary, and sometimes a second and less distinctive boundary, which lies in the vicinity of the late-summer surface firn line of warm years. However, it always lies at a somewhat higher elevation and seems to represent a vertical subsurface structure, possibly a subsurface firn-ice transition. The late-summer surface firn line cannot be detected on these winter images, probably because the firn-ice transition often slopes only little with respect to the surface. This allows the penetrating microwaves to reach the underlying ice in the area directly above the late-summer FLA. Hence, the late-summer situation is not visible in winter images and these images cannot be related to annual mass balance, but only to long-term changes in glacier zonation. On glaciers with steeper slopes than Brúarjökull, the surface firn line and the subsurface firn-ice transition are probably not separable from each other. Such glaciers will tend to have a firn-ice transition that dips more with respect to the surface.

The equilibrium line is often not visible on SAR images, but nevertheless SAR

images may be used in other ways to infer the mass balance. The intensity of the $\sigma_0$-signal is related to surface wetness (and roughness) and therefore to the amount of surface melt. For western Brúarjökull, we found a weak correlation between $B_m$ and the mean $\sigma_0$ over the surface area and during part of the melting season, but for two other drainage basins no such correlation was found. It seems that, due to variable surface roughness and/or wetness, $\sigma_0$ is too variable in time to be a good proxy for $B_m$, but to draw a firm conclusion data from more years are needed. Now we have three to five years with both mass balance data and SAR data for each drainage basin. The mean FLA during part of the melting season may be a better estimator of $B_m$. This is the case for western Brúarjökull, Eyjabakkajökull and Dyngjujökull. On Tungnaárjökull, the transition from ice to snow and/or firn is often extremely patchy and gradual, making it impossible to derive a FLA. For Köldukvíslarjökull, we found too few usable images to obtain a usable correlation with $B_m$. This is due to its hypsometry: the ice margin lies relatively high and bare ice appears relatively late in the summer. The period during which the transient snow line lies between the ice margin and the long-term firn line is therefore short; once the transient snow line lies above the firn line, the FLA is unrelated to the annual mass balance. On the other hand, in 1992 the transient snow line remained at a low altitude all summer and hardly reached the ice margin.

It can be concluded therefore that, for a temperate ice cap like Vatnajökull with no or little dry surface snow during the summer, SAR images contain less information about $B_m$ than albedo images. Variations in the albedo of snow and firn, which are visible on albedo images, can be related to $B_m$ (De Ruyter de Wildt et al., 2002b), but SAR images of melting surfaces do not seem to display usable variations of the signal within the accumulation area. The equilibrium line is often not visible, and the firn line is the only feature that can be unambiguously detected on summer SAR images of Vatnajökull. The average FLA during the melting season is for some drainage basins of Vatnajökull related to $B_m$, but for others this quantity cannot be derived. For glaciers and ice caps like Vatnajökull, the only advantage of SAR images over albedo images lies in the fact that they display the firn line irrespective of weather and illumination conditions, which for some glaciers can be used to infer $B_m$.

# 6 Using various methods to estimate the mean specific mass balance

**Abstract**

In this chapter we compare different estimates of the mean specific mass balance of Vatnajökull with each other. The estimates are obtained from *in situ* measurements, a mass balance model, satellite-derived net potential short-wave radiation and satellite-derived firn lines. For the north-western part of Vatnajökull the indirect observations correspond within the uncertainty limits with the direct (*in situ)* observations. Only for one year the different estimates strongly diverge, probably due to a lack of satellite images and an erroneously modeled distribution of precipitation. We compute the best estimate of the mass balance of north-western Vatnajökull as the weighted mean of the individual estimates. For the part of Vatnajökull where the mass balance has not been measured, we use the indirect methods to estimate relative variations in mass balance.

## 6.1 Comparing indirect estimates of the mass balance of north-western Vatnajökull with direct observations.

In the previous chapters we used observations of the mass balance to calibrate several methods for indirect estimation of the mean specific mass balance ($B_m$). We calibrated a mass balance model and related satellite-derived net potential global radiation ($Q_{pot,net}$) and Firn Line Altitude (FLA) to $B_m$. We obtained the following empirical relation with which the mean specific mass balance can be derived from AVHRR-derived $<Q_{pot,net}>$ (see figure 4.10):

$$B_{m,Q} = a - b < Q_{pot,net} > \qquad 6.1$$

Values of the coefficients a and b for the drainage basins of northern and western Vatnajökull and for the entire north-west of Vatnajökull are given in table 6.1. For the derivation of equation 6.1 *in situ* measurements of $B_m$ have been used, but once this relation is known for a glacier or ice cap it can be used to estimate $B_m$ without any additional *in situ* measurements at all. The same applies to the relation between $B_m$ and the satellite-derived mean Firn Line Altitude (<FLA>) during the second part of the melting season (figure 5.10):

$$B_{m,FLA} = a - b < FLA > \qquad 6.2$$

Again, values of the coefficients a and b are given in table 6.1. We derived the FLA both

| Source | model | $B_m$=a-b<$Q_{pot,net}$> | | | | $B_m$=a-b<FLA> | | | |
|---|---|---|---|---|---|---|---|---|---|
| | r | a | b | r | uncertainty in $B_{m,Q}$ | a | b | r | uncertainty in $B_{m,FLA}$ |
| western Brúarjökull | 0.97 | 4.53 | 0.0228 | 0.89 | 0.59 | 13.0 | 0.0118 | 0.91 | 0.56 |
| eastern Brúarjökull | 0.92 | 6.62 | 0.0335 | 0.94 | 0.76 | 17.2 | 0.0171 | 0.98 | 0.65 |
| Eyjabakkajökull | 0.92 | 5.79 | 0.0283 | 0.90 | 0.72 | 10.4 | 0.0108 | 0.91 | 0.56 |
| Dyngjujökull | 0.95 | 5.60 | 0.0271 | 0.90 | 0.68 | 16.9 | 0.0138 | 0.98 | 0.57 |
| Köldukvíslarjökull | 0.97 | 4.28 | 0.0241 | 0.92 | 0.50 | | | | |
| Tungnaárjökull | 0.86 | 4.51 | 0.0251 | 0.87 | 0.73 | | | | |
| NW Vatnajökull | 0.96 | 5.07 | 0.0260 | 0.95 | 0.59 | | | | |

*Table 6.1. Values of the coefficients a and b in the equations 6.1 and 6.2 and corresponding correlation coefficients and uncertainties in $B_m$ ( in m w.e.). Also shown are correlation coefficients between modeled (chapter 2) and observed mean specific mass balance (second column).*

from AVHRR images and from ERS SAR images. For Tungnaárjökull the transition from ice to snow or firn was nearly always very patchy and gradual (figure 1.3), making it practically impossible to derive a FLA. For Köldukvíslarjökull we could not establish a useful relation between $B_m$ and <FLA> due to a lack of usable data.

All the different estimates of $B_m$ are shown as a function of time in figure 6.1. The differences between the various estimates are largest for Eyjabakkajökull and for Tungnaárjökull and for the year 1992 in general. Eyjabakkajökull is the smallest of the drainage basins where the mass balance has been measured. Its mass balance has been measured at only four sites and the error in $B_{m,obs}$ may be somewhat larger for this drainage basin than for the others. Its relatively small size, compared to the AVHRR pixel size, may furthermore be responsible for the rather high uncertainty in $B_{m,Q}$ (table 6.1). Tungnaárjökull always displays a very irregular and patchy firn line and large fluctuations of the mass balance with respect to elevation, probably caused by snowdrift (Björnsson et al., 1998a). This can introduce errors in the values of $B_{m,obs}$, and consequently in the estimate $B_{m,Q}$ which is derived from the relation between $B_{m,obs}$ and <$Q_{pot,net}$>.

In 1997, the mass balance of most drainage basins shown in figure 6.1 was much lower than allowed by the meteorological conditions. This was due to tephra that lowered the albedo of large parts of the accumulation area and significantly enhanced melting in the summer. Both satellite methods take this effect adequately into account. The mass balance model also does a fairly good job in this respect, but it must be remembered that the tephra-induced albedo lowering is explicitly prescribed in the model. The meteorological conditions alone can not produce the exceptionally low mass balance for1997. This is shown by the results for Tungnaárjökull and Köldukvíslarjökull, which were hardly or not at all affected by tephra. For these two drainage basins, all methods give the same results for 1997 as for other years of comparable meteorological conditions (1995, 1996 and 1998).

All three indirect methods are calibrated with the same direct measurements of the mass balance, so a good test of the performance of the three indirect methods is a comparison of the results for the years in which the mass balance has not been measured. In 1991 the mass balance has not been measured at all and in 1992 only on Köldukvíslarjökull and on Tungnaárjökull. For 1991 the three indirect methods all give strongly negative

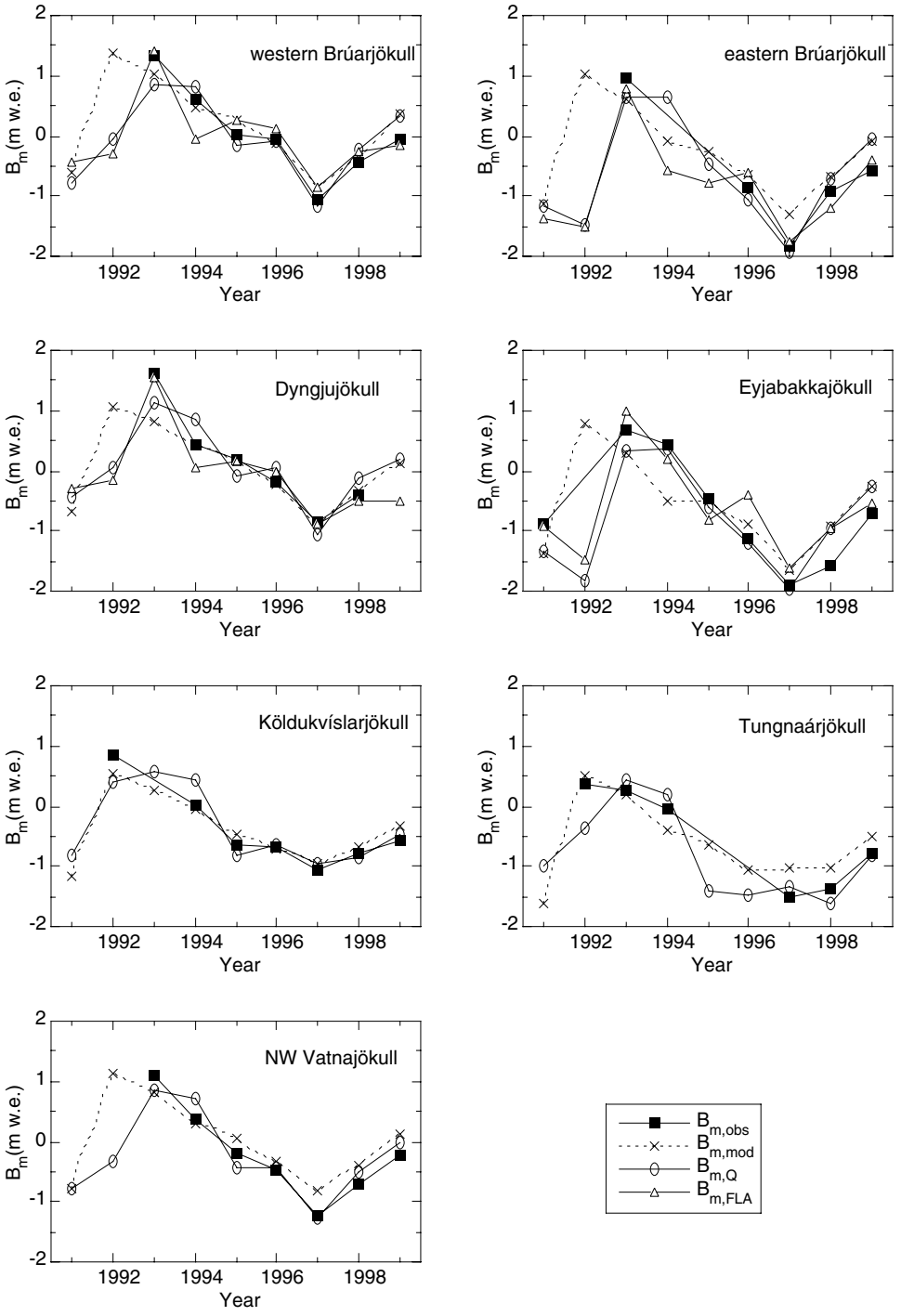


*Figure 6.1. Observed (obs), modeled (mod), $Q_{pot,net}$-derived (Q) and FLA-derived (FLA) mean specific mass balance of the north-western drainage basins of Vatnajökull.*

mass balance values (figure 3.5). However, for 1992 large differences occur. The model suggests that $B_m$ was strongly positive, which is confirmed by the observations on Köldukvíslarjökull and to a lesser extent by those on Tungnaárjökull. The summer was cold and cloudy due to cyclonic circulation with frequent southerly to westerly winds (Björnsson et al., 1998a). July and August were cold and in June and September high precipitation contributed to a positive mass balance (figure 3.5). Because of high cloudiness, we could find only one usable AVHRR image (on August 9$^{th}$) during the second half of the summer (after July 14$^{th}$), and this image still displayed clouds over 36% of the surface. A significant part of the summer is therefore not used to derive $<Q_{pot,net}>$ and especially this part of the summer gave a significant positive contribution to the mass balance (Björnsson et al., 1998a). This is confirmed by figure 6.2, which shows that a significant amount of snow accumulated after August 9$^{th}$ (day 222), but before the end of the mass balance year (September 21$^{st}$, day 265). Note that in other years a thick new snow pack does not begin to form before the end of the mass balance year. In 1994 there is a similar lack of images in August and September, which is probably the cause of the low values of $B_{m,FLA}$ on Brúarjökull for this year.

On the other hand, due to the frequent southerly and easterly winds, precipitation over the north-east was probably significantly lower than over the south and west. The precipitation from Fagurhólsmyri, which is not influenced by a topographic barrier to the south-west, may therefore not have been representative of the north-east of Vatnajökull and hence introduce an error in the modeled mass balance ($B_{m,mod}$). This idea is supported by the decrease in $B_{m,Q}$ and $B_{m,FLA}$ towards the east. For Köldukvíslarjökull $B_{m,Q}$ is positive

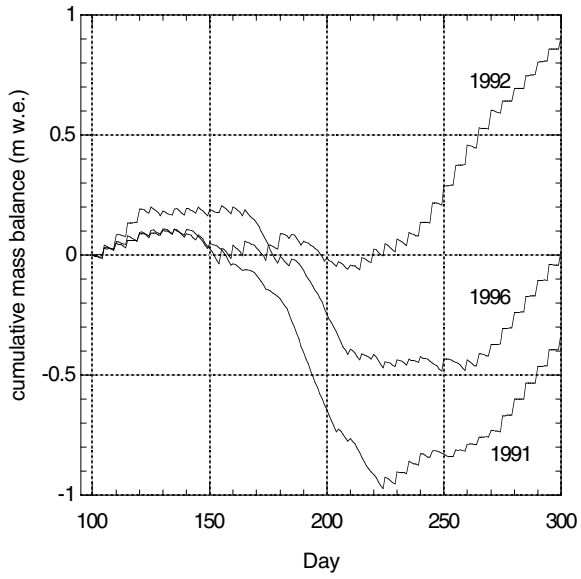


*Figure 6.2. Modeled cumulative mass balance near automatic weather station U7 in the central part of Vatnajökull (at 1520 m altitude). At day 100, a few weeks before the start of the melting season, the cumulative mass balance has been set to zero.*

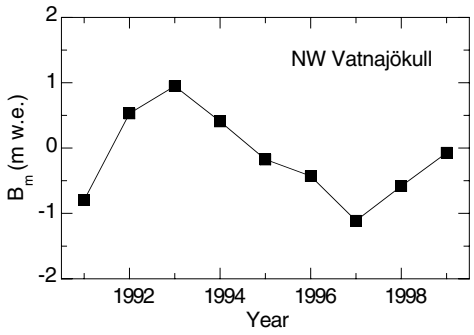


*Figure 6.3. Best estimate of the mean specific mass balance of the whole north-western part of Vatnajökull, calculated with equation 6.3.*

and corresponds reasonably well with $B_{m,obs}$ and $B_{m,mod}$. For Dyngjujökull and western Brúarjökull $B_{m,Q}$ and $B_{m,FLA}$ are slightly negative, and for eastern Brúarjökull and Eyjabakkajökull $B_{m,Q}$ and $B_{m,FLA}$ are strongly negative. It seems therefore that although $B_m$ was positive in the west, it was near-neutral or slightly negative in the north-east due to persistent atmospheric circulations during the summer of 1992. The mass balance model does not take such gradients into account and gives too positive mass balance values for this year.

All the mass balance estimates shown in figure 6.1 contain an error. One can therefore define a best estimate of $B_m$ by computing the weighted mean of all individual estimates (Oerlemans, 2001). In our case we have

$$B_{m,best} = \frac{B_{m,obs}/\sigma_{obs} + B_{m,mod}/\sigma_{mod} + B_{m,Q}/\sigma_Q + B_{m,FLA}/\sigma_{FLA}}{1/\sigma_{obs} + 1/\sigma_{mod} + 1/\sigma_Q + 1/\sigma_{FLA}} \qquad 6.3$$

where $\sigma$ is the uncertainty in each estimate. A rough estimate of $\sigma_{obs}$ is 0.25 m w.e., whereas the other uncertainties have three sources. When we estimate $B_m$ from a (linear) regression between $B_{m,obs}$ and a proxy, the uncertainty in the proxy-derived $B_m$ is:

$$\sigma = \sqrt{\sigma_{obs}^2 + \sigma_{regr}^2 + \sigma_{prox}^2} \qquad 6.4$$

where $\sigma_{prox}$ is the uncertainty in $B_m$ due to the error in the proxy and $\sigma_{regr}$ is the regression error. Values of $\sigma$ are given in table 6.1. The best estimate for the whole north-western part of Vatnajökull is shown in figure 6.3.

## 6.2 Indirect estimates of the mass balance of southern and south-eastern Vatnajökull

The mass balance of the southern and south-eastern drainage basins of Vatnajökull, comprising roughly half of Vatnajökull (see figure 2.1), has only sporadically been measured and no direct observations of $B_m$ of these areas are available. The only information we have comes from the mass balance model and from the satellite images. As a consequence, we cannot establish relations $B_m$ and satellite-derived quantities. However, we can apply a linear operation upon the satellite-derived values of $<Q_{pot,net}>$ and <FLA>, in such a way that $B_{m,mod}$ is matched. This will not produce absolute values of $B_m$ for southern and eastern Vatnajökull, but nevertheless provide independent estimates of the relative variations in mass balance. Figure 6.4 shows that $B_{m,FLA}$ and $B_{m,Q}$ correspond quite well with $B_{m,mod}$ for the large drainage basins in the south and south-east. Only for the year 1992 large differences exist, as was also the case for most other drainage basins of Vatnajökull (figure 6.1). For Breidamerkurjökull we did not obtain a useful relation between

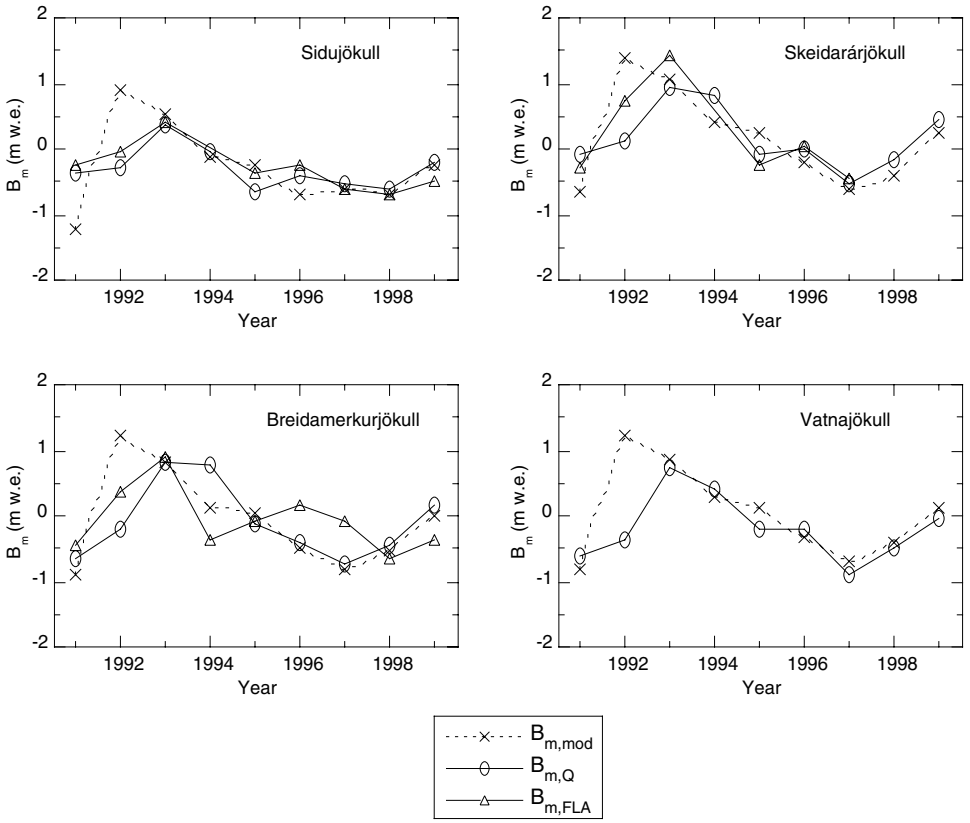


*Figure 6.4. Modeled (mod) and $Q_{pot,net}$-derived (Q) mean specific mass balance of the southern and eastern drainage basins of Vatnajökull and of Vatnajökull as a whole.*

<FLA> and $B_{m,obs}$, which is probably due to the relatively steep slopes near the late-summer firn line. This makes it difficult to estimate the FLA from the AVHRR images. $B_{m,Q}$ does not suffer from this problem because it is obtained from a surface integral.

### 6.3 Conclusions

Both the mass balance model and the satellite methods are able to reproduce $B_m$ reasonably well, but they both have their merits and demerits. A mass balance model can be used for sensitivity experiments, but needs to be calibrated with *in situ* measured data. For many glaciers these data are not available and for these glaciers satellite images may be used to estimate the mass balance. This can only be done in a quantitative way when the relation between $<Q_{pot,net}>$ and $B_m$ is known, but this relation is not the same for each glacier; and to establish such a relation *in situ* measurements are required. When these are not available, satellite-derived values of $<Q_{pot,net}>$ can still be used to estimate relative changes in $B_m$, which is useful information when nothing else about a glacier or ice cap is known.

# 7 The future of remote sensing of glacier mass balance

In the chapters 4 and 5 we used reflectance (NOAA AVHRR) and active microwave (ERS SAR) images to retrieve the mean specific mass balance ($B_m$) of Vatnajökull. However, many other satellites carry instruments that can be used for glaciological purposes, and moreover, remote sensing of the earth is a field of ongoing research and innovation. New platforms with new instruments have been launched in recent years and more will follow in the near future. In this chapter we will discuss the possibilities of existing and new instruments for mass balance retrieval. Some satellite instruments that have been often used in glaciology and some promising new instruments are listed in table 7.1. All of these instruments are on satellites with polar or near-polar orbits. This is necessary for good observation of polar and high-latitude regions, where many glaciers and ice caps are situated. Most instruments shown measure at visible and infrared wavelengths, allowing determination of surface albedo, glacial extent and Firn Line Altitude (FLA). New developments for this category are mainly towards better spectral resolution and towards measuring from different viewing angles, both allowing a more accurate determination of the surface albedo. In contrast to these sensors, which are all passive, Synthetic Aperture Radar (SAR) is an active instrument: it sends out a signal and records the echo from the earth's surface. SAR has been used for, amongst other things, detection of the firn line. Interesting new active instruments are altimeters that can measure surface height with an accuracy that is high enough for estimation of $B_m$.

In the chapters 4 and 5 it has been shown how satellite data can be used to estimate $B_m$. Previous ways of estimating $B_m$ from satellite images relied on identification of the equilibrium line, but this line is often not detectable. We therefore investigated alternative ways of estimating $B_m$, which required more information than the position of one boundary on one day. In chapter 4 we used reflectance images from the entire melting season to derive the net potential global radiation over the surface, which can be considered as a proxy for the surface energy balance and hence for $B_m$. Ten to fifteen images over the melting season (one or two images per fortnight) proved to be sufficient to obtain a good estimate of $B_m$. The reflectance method was applied to Vatnajökull using NOAA AVHRR images, which are available at least once a day and low-priced. In chapter 5 we used a related method to estimate $B_m$. We found that the mean FLA during the melting season is linearly related to $B_m$. However, this method is less widely applicable than the reflectance method from chapter 4, because the firn line is not always clearly present and/or detectable, even when radar images are used (which penetrate clouds).

NOAA AVHRR images have a resolution of 1.1 km at nadir, which is sufficient for Vatnajökull (8200 $km^2$) and other ice bodies of considerable size. A benefit from the reflectance method from chapter 4 lies in the fact that it uses the reflectance, averaged over the surface. This means that the satellite images must resolve the glacier itself, and not a single boundary within the glacier. This allowed us to apply the method to Eyjabakkajökull, using AVHRR images. Eyjabakkajökull is a medium size outlet glacier of Vatnajökull

| Satellite and instrument | Agency | Mission date | Horizontal resolution (m) | Temporal resolution (days) | nr. of bands | Spectral region | Wave-lengths or frequency |
|---|---|---|---|---|---|---|---|
| SELECTED RECENT MISSONS | | | | | | | |
| Landsat TM | NOAA | since 1982 | 30 | 14 | 7 | visible - infrared | 0.45 – 12.5 μm |
| NOAA AVHRR | NOAA | since 1978 | ≥ 1100 | 0.5 | 5 | visible - infrared | 0.58 – 12.5 μm |
| SPOT HRV | CNES | since 1986 | 20 | 3 | 3 or 4 | visible - infrared | 0.50 – 0.89 μm |
| ERS SAR | ESA | since 1991 | 30 | a few | | active microwave (radar) | 5.3 Ghz (C-band) |
| SELECTED NEW MISSIONS | | | | | | | |
| Envisat MERIS | ESA | 2001 | 300 | 3 | 15 | visible - infrared | 0.39 – 10.4 μm |
| EOS AM-1 (TERRA) MODIS | NASA | 1999 | 250 (1,2) 500 (3-7) 1000 (8-36) | 3 | 36 | visible - infrared | 0.40 – 14.4 μm |
| EOS-AM (TERRA) ASTER | NASA | 1999 | 15 (1-3) 30 (4-9) 90 (10-14) | 16 | 14 | visible - infrared | 0.52 – 12.4 μm |
| ICESat GLAS | NASA | 2002 | 70 | | | active visible – infrared (lidar) | 0.53 / 1.06 μm |
| CRYOSAT SA-altimeter | ESA | 2004 | | | | active microwave (radar) | Ku-band (10.7 - 14.5 Ghz) |
| ALOS PRISM | NASDA | 2004 | 2.5 | | | visible (stereoscopic altimeter) | |

*Table 7.1. Selection of recent and new satellite missions that are of importance for mass balance retrieval. CNES=Centre National d'Etudes Spatiales (France); ESA=European Space Agency; NASA=National Aeronautics and Space Administration (USA); NASDA=National Space Development Agency (Japan); NOAA=National Oceanic and Atmospheric Administration (USA). Data from König et al. (2001a) and from the respective space agencies.*

with a length of about 20 km and an area of 120 $km^2$. It seems also possible to use AVHRR images in the same way for glaciers that are somewhat smaller, but for much smaller glaciers satellite data with higher resolution must be used. Often-used satellites with high resolution (30 m) are the Landsat satellites. However, these satellites have a temporal resolution of about two weeks, which is too long for a cloudy place such as Iceland. Cloud-free days do not occur often over Iceland and the changes of capturing these days with Landsat Thematic Mapper (TM) images are not very high. Also for less cloudy places this can be a serious limitation. So in order to establish a usable time series of images taken on cloud-free days, a shorter temporal resolution is required. Several satellites that carry high resolution instruments meet this requirement. The SPOT satellites, which carry the High Resolution Visible (HRV) instrument, have a temporal resolution that is short enough (3 days) and a horizontal resolution of 20 m. The new instruments MERIS on board of Envisat and Modis on board of the EOS AM-1 satellite have an intermediate horizontal resolution of 300 and 250 m, respectively, and an acceptable temporal resolution of 3 days. ASTER, also on board of the EOS AM-1 satellite, has a high resolution but a rather long temporal resolution of 16 days. Summarizing, we can say that it is technically possible to apply the reflectance method to nearly all glaciers and ice caps in the world, so that the only possible limitation is financial.

A promising remote sensing tool is altimetry. Altimeters are active instruments that measure the height of the earth's surface and have therefore the potential to measure the surface mass balance: disregarding refreezing of meltwater and densification processes, the mass balance corresponds to the change in surface height. Current space-borne altimeters (the ERS altimeter and the Envisat altimeter) only measure the surface altitude accurate enough for mass balance estimates when the surface slope is lower than 0.5°. They can therefore be used to study the interiors of the Greenland and Antarctic ice sheets, but not of their margins. These ice sheets are the most dynamic and the most sensitive to climatic change at their margins, and hence existing altimeters cannot be used to measure their mean specific mass balance. The same applies to most ice caps and glaciers, which generally have surface slopes that are significantly higher than 0.5°. Two satellites that are to be launched in the near future (NASA's ICESat and ESA's CRYOSAT) carry altimeters that can measure surface elevation with high accuracy over (gently) sloping surfaces. The Geoscience Laser Altimeter System (GLAS) on board of IceSat is an active optical sensor (lidar) that measures surface height with a spatial resolution of 70 m. This is high enough for studying not only the ice sheets of Antarctica and Greenland and large ice caps (e.g. Vatnajökull), but also smaller ice caps and glaciers. The same applies to the Synthetic Aperture (SA) altimeter on board of CRYOSAT, which is an active microwave sensor (radar). It is to be expected that both instruments will lead to a significant reduction in the uncertainty of mass balance estimates Antarctica, Greenland and many ice caps and glaciers.

Altimeters can provide absolute estimates of $B_m$, whereas the reflectance method of chapter 4 only provides relative changes in $B_m$. On the other hand, usable altimeter data are not yet available, whereas reflectance has been measured from spacecraft for over twenty years now. With the reflectance method, it is therefore possible to estimate (relative changes in) $B_m$ of many ice caps and glaciers world wide for the past 20 years or so. When *in situ* measurements are available for some years, these can be used to calibrate the

reflectance method so that it can provide absolute estimates of $B_m$. Reflectance data, lidar and radar are three independent sources of data, and as stated in chapter 6, the best estimate of $B_m$ is the weighted average of several individual estimates.

# References


Abdalati, W. and K. Steffen. Accumulation and hoar effects on microwave emission in the Greenland ice-sheet dry-snow zones. *J. Glaciol.*, 44(148), 523-531, 1998.

Adam, S., A. Pietroniro and M. M. Brugman. Glacier snow line mapping using ERS-1 SAR imagery. *Remote Sens. Environ.*, 61(1), 46-54, 1997.

Ambach, W. and M. Kuhn. Accumulation gradients in Greenland and mass balance response to climatic changes. *Z. Gletscherk. Glazialgeol.*, 21, 311-317, 1985.

Ambach, W. Untersuchungen zum Energieumsatz in der Ablationszone des grönlandischen Inlandeises (Camp IV-EGIG, 69°40'05" N, 49°37'58" W). *Meddelelser om Grønland*, 174(4), 1963.

Andreas, E. A theory for the scalar roughness and the scalar transfer coefficients over snow and sea ice. *Boundary-Layer Meteorol.*, 38, 159-184, 1987.

Arnold, N. S., I. C. Willis, M. J. Sharp, K. S. Richards and W. J. Lawson. A distributed surface energy-balance model for a small valley glacier. I. Development and testing for Haut Glacier d'Arolla, Valais, Switzerland. *J. Glaciol.*, 42(140), 77-89, 1996.

Baum, A. A. and Q. Trepte. A grouped threshold approach for scene identification in AVHRR imagery. *J. Atmos. Ocea. Tech.*, 16, 793-800, 1999.

Bintanja, R. and M. R. van den Broeke. The influence of clouds on the radiation budget of ice and snow surfaces in Antarctica and Greenland in summer. *Int. J. Clim.*, 16, 1281-1296, 1996.

Björnsson, H., F. Pálsson, M. T. Gudmundsson, and H. H. Haraldsson. Afkoma, Hreyfing og afrennsli á vestan- og nordanverdum Vatnajökli jökulárid 1995-1996. *Rep. RH-24-97*, Science Institute, University of Iceland, 1997.

Björnsson, H., F. Pálsson, M. T. Gudmundsson, and H. H. Haraldsson. Mass balance of western and northern Vatnajökull, Iceland, 1991-1995. *Jökull*, *45*, 35-58, 1998a.

Björnsson, H., F. Pálsson, M. T. Gudmundsson, and H. H. Haraldsson. Mass balance and meteorological obserations on Vatnajökull 1997. *Rep. RH-03-98*, Science Institute, University of Iceland, 1998b.

Björnsson, H., F. Pálsson, M. T. Gudmundsson, and H. H. Haraldsson. Mass balance and meteorological observations on Vatnajökull 1998. *Rep. RH-14-98*, Science Institute, University of Iceland, 1998c.

Björnsson, H., F. Pálsson, M. T. Gudmundsson, and H. H. Haraldsson. Mass balance and meteorological observations on Vatnajökull 1999. *Rep. RH-24-99*, Science Institute, University of Iceland, 1999.

Bozhinskiy, A. N., M. S. Krass and V. V. Popovnin. Role of debris cover in the thermal physics of glaciers. *J. Glaciol.*, 32(111), 255-266, 1986.

Braithwaite, R. J. Calculation of degree-days for glacier-climate research. *Z. Gletscherkd. Glazialgeol.*, 20, 1-8, 1985.

Braithwaite, R. J. Aerodynamic stability and turbulent sensible-heat flux over a melting ice surface, the Greenland ice sheet. *J. Glaciol.*, 41(137), 153-160, 1995.

Braithwaite, R. J. and O. B. Olesen. A simple energy-balance model to calculate ice

ablation at the margin of the Greenland ice sheet. *J. Glaciol.*, 36(123), 222-288, 1990.

Brown, I. A., M. P. Kirkbride and R. A. Vaughan. Find the firn line! The suitability of ERS-1 and ERS-2 SAR data for the analysis of glacier facies on Icelandic icecaps. *Int. J. Remote Sensing*, 20(15&16), 3217-3230, 1999.

Colbeck, S. C. A theory for water flow through a layers snow pack. *Water Resour. Res.*, 11(2), 261-266, 1975.

Cressie, N. A. *Statistics for Spatial Data*, Wiley, New York, 1993.

De Ruyter de Wildt, M. S., J. Oerlemans and H. Björnsson. A calibrated mass balance model for Vatnajökull, Iceland. *Jökull*, submitted, 2002a.

De Ruyter de Wildt, M. S., J. Oerlemans and H. Björnsson. A method for monitoring glacier mass balance using satellite albedo measurements: application to Vatnajökull (Iceland). *J. Glaciol.*, in press, 2002b.

Demuth, M. and A. Pietroniro. Inferring glacier mass balance using radarsat: results from Peyto glacier, Canada. *Geografiska Annaler*, 81A(4), 521-540, 1999.

Denby, B. and W. Greuell. The use of bulk and profile methods for determining the surface heat fluxes in the presence of glacier winds. *J. Glaciol.*, 46(154), 445-452, 2000.

Ebert, E. A pattern recognition technique for distinguishing surface and cloud types in the polar regions. *J. Clim. Appl. Meteorol.*, 26(10), 1412-1427, 1987.

Einarsson, M. Temperature conditions in Iceland, 1901-1990. *Jökull*, 41, 1-20, 1991.

Fahnestock, M., R. Bindschadler, R. Kwok and K. Jezek. Greenland Ice Sheet Surface Properties and Ice Dynamics from ERS-1 SAR Imagery. *Science*, 262, 1530-1534, 1993.

Fily, M., B. Bourdelles, J. P. Dedieu, and C. Sergent. Comparison of in situ and Landsat Thematic Mapper derived snow grain characteristics in the Alps. *Remote Sens. Environ.*, 59, 452-460, 1997.

Gesell, G. An algorithm for snow and ice detection using AVHRR data. An extension to the APOLLO software package. *Int. J. Remote Sens.*, 10(4,5), 897-905, 1989.

Greuell, W. Hintereisferner, Austria: mass-balance reconstruction and numerical modelling of historical length variations. *J. Glaciol.,* 38(129), 233-244, 1992.

Greuell, W. and J. Oerlemans. Sensitivity studies with a mass balance model including temperature profile calculations inside the glacier. *Z. Gletscherk. Glazialgeol.*, 22, 101-124, 1986.

Greuell, W. and M. S. de Ruyter de Wildt. Anisotropic reflection of melting glacier ice: measurements and parameterizations. *Remote Sens. Environ.*, 70, 265-277, 1999.

Greuell, W. and R. Böhm. 2 m temperatures along melting mid-latitude glaciers, and implications for the sensitivity of the mass balance to variations in temperature. *J. Glaciol.*, 44(146), 9-20, 1998.

Greuell, W. and W. H. Knap. Remote sensing of the albedo and detection of the slush line on the Greenland ice sheet. *J. Geophys. Res.*, 105, 15,567-15,576, 2000.

Greuell, W., C. H. Reijmer and J. Oerlemans. Narrowband-to-broadband albedo conversion for glacier ice and snow based on aircraft and near-surface measurements. *Remote Sens. Environ.*, in press, 2002.

Greuell, W., W. H. Knap, and P. C. Smeets. Elevational changes in meteorological variables along a midlatitude glacier during summer. *J. Geophys. Res.*, 102, 25,941-25,954, 1997.

Grove, J. M. The little ice age, Methuen, London, 1988.

Gudmundsson, M. T. Mass balance and precipitation on the summit plateau of Öraefajökull, SE-Iceland. *Jökull*, 48, 49-54, 2000.

Gudmundsson, M. T., F. Sigmundsson and H. Björnsson. Ice-volcano interaction of the 1996 Gjálp subglacial eruption, Vatnajökull, Iceland. *Nature*, 389 (30), 954-957, 1997.

Gueymard, C. Critical analysis and performance assessment of clear sky solar irradiance models using theoretical and measured data. *Sol. Energ.*, 51(2), 121-138, 1993.

Günther, R. and D. Widlewski. Die Korrelation verschiedener Klimaelemente mit dem Massenhaushalt alpiner und skandinavischer Gletscher. *Z. Gletscherkd. Glazialgeol.,* 22, 125-147, 1986.

Hagen, J. O. and O. Liestøl. Long-term glacier mass-balance investigations in Svalbard, 1950-88. *Ann. Glaciol.*, 14, 102-106, 1990.

Hall, D. K., R. S. Williams Jr. and K. J. Bayr. Glacier recession in Iceland and Austria as observed from space. *EOS*, 73(12), 129, 135, 141, 1992.

Hall, D. K., R. S. Williams Jr., J. S. Barton, O. Sigurdsson, L. C. Smith and J. B. Garvin. Evaluation of remote-sensing techniques to measure decadal-scale changes of Hofsjökull ice cap, Iceland. *J. Glaciol.*, 46(154), 375-388, 2000.

Hall, D. K., R. S. Williams, Jr. and O. Sigurdsson. Glaciological observations of Brúarjökull, Iceland, using synthetic aperture radar and thematic mapper satellite data. *Ann. Glaciol.*, 21, 271-276, 1995.

Hastenrath, S. and L. Greischar. Glacier recession on Kilimanjaro, East Africa, 1912-89. *J. Glaciol.*, 43(145), 455-459, 1997.

Hay, J. E. and B. B. Fitzharris. A comparison of the energy-balance and bulk aerodynamic approaches for estimating glacier melt. *J. Glaciol.*, 34, 145-153, 1988.

Hoinkes, H. and R. Steinacker. Zur Parametrisierung der beziehung Klima - Gletscher. *Rivista Italiana di Geofysica e Scienze Affini*, 1, 97-104, 1975.

Holmlund, P., W. Karlen and H. Grudd. Fifty years of glacier mass balance and front observations at the Tarfala Research Station. *Geografiska Annaler*, 78A, 105-114, 1996.

Houghton, J. T., L. G. Meiro Filho, B. A. Callander, N. Harris, A. Kattenberg and K. Maskell, editors. Climate change 1995: the science of climate change. Cambridge, etc., Cambridge University Press., 1996.

Houghton, J. T., Y. Ding, D. J. Griggs, M. Noguer, P. J. van de Linden, X. Dai, K. Maskell and C. A. Johnson, editors. Climate change 2001: The scientific basis, chapter 11. *IPCC Report*, 2001.

Huybrechts, P., A. Letréguilly, and N. Reeh. The Greenland ice sheet and greenhouse warming. *Global Planet. Change*, 3(4), 399-412, 1991.

Jezek, K. C., M. R. Drinkwater, J. P. Crawford, R. Bindschadler and R. Kwok. 1993. Analysis of synthetic aperture radar data collected over the southwestern Greenland ice sheet. *J. Glaciol.*, 39(131), 119-132.

Jóhannesson, T. The response of two Icelandic glaciers to climate warming computed with a degree-day glacier mass balance model coupled to a dynamic glacier model. *J. Glaciol.*, 43(144), 321-327, 1997.

Jóhannesson, T. and O. Sigurdsson. Interpretation of glacier variations in Iceland 1930-1995. *Jökull*, 45, 27-33, 1998.

Kirkbride, M. P. Processes of transportation, in *Modern glacial environments: processes, dynamics and sediments. Vol. 1. Glacial environments*. Edited by J. Menzies, pp. 261-292, Butterworth-Heinemann, Oxford, 1995.

Klok , E. J. and J. Oerlemans. Deriving a climate history from a glacier length record by linear inverse modelling. *The Holocene*, in press, 2002.

Knap, W. H., B. W. Brock, J. Oerlemans and I. C. Willis. Comparison of Landsat-TM derived and ground-based albedo of Haut Glacier d'Arolla. *Int. J. Remote Sens.*, 20(17), 3293-3310, 1999.

Koelemeijer, R., Oerlemans, J. and Tjemkes, S. Surface reflectance of Hintereisferner, Austria, from Landsat 5 TM imagery. *Ann. Glaciol.*, 17, 17-22, 1993.

Koks, M. Anisotropic reflection of radiation by melting snow. Landsat TM bands 2 and 4, *M.S. thesis*, IMAU, Universiteit Utrecht, The Netherlands, 2001.

König, M., J.-G. Winther and E. Isaksson. Measuring snow and glacier ice properties from satellite. Rev. Geophys., 39(1), 1-27, 2001a.

König, M., J.-G. Winther, N. T. Knudsen and T. Guneriussen. Firn-line detection on Austre Okstindbreen, Norway, with airborne multipolarization SAR. *J. Glaciol.*, 47(157), 251-257, 2001b.

Konzelmann, T., R. S. W. van de Wal, W. Greuell, R. Bintanja, E. A. C. Henneken, and A. Abe-Ouchi. Parameterisation of global and longwave incoming radiation for the Greenland Ice Sheet. *Global and Planetary Change*, 9, 143-164, 1994.

Kuhn, M. On the computation of heat transfer coefficient from energy-balance gradients on a glacier. *J. Glaciol.*, 22(87), 263-272, 1989.

Kuhn, M., E. Schlosser and N. Span. Eastern Alpine glacier activity and climatic records since 1860. *Ann Glaciol.,* 24, 164-168, 1997.

Kulkanari, A. V. Mass balance of Himalayan glaciers using AAR. *J. Glaciol.*, 38(128), 101-103, 1992.

Lamb, H. H. Climate, history and the modern world. Routledge, Londen, pp. 260., 1995.

Larsen, G., M. T. Gudmundsson and H. Björnsson. Eight centuries of periodic volcanism at the center of the Iceland hotspot revealed by glacier tephrostratigraphy. *Geology*, 26(10), 943-946, 1998.

Laur, H., P. Bally, P. Meadows, J. Sanchez, B. Schaettler, E. Lopinto and D. Esteban. ERS SAR calibration. Derivation of the backscettering coefficient $\sigma 0$_in ESA ERS SAR PRI products. *ESA/ESRIN Technical note* ES-TN-RS-PM-HL09, Issue 2, Rev. 5b, 1998.

Lawler, D. M., H. Björnsson and M. Dolan. Impact of subglacial geothermal activity on meltwater quality in the Jökulsa a Sólheimasandi system, southern Iceland. *Hydrological Processes*, 10, 557-578, 1996.

Leroux, C., J. Lenoble, G. Brogniez, J. W. Hovenier, and J. F. de Haan. A model for the bidirectional polarized reflectance of snow. *J. Quant. Spectrosc. Radiat. Transfer*, 61(3), 273-285, 1999.

Lliboutry, L. Multivariate statistical analysis of glacier annual balance. *J. Glaciol.,* 13, 371-392, 1974.

Mackintosh, A. Glacier fluctuations and climatic change in Iceland. Ph.D. Thesis, Department of Geography, University of Edinburgh, Scotland, 2000.

Mätzler, C. Applications of the interaction of microwaves with the natural snow cover. *Rem. Sens. Rev.*, 2(2), 259-387, 1987.

McClatchey, R. A., R. W. Fenn, J. E. A. Selby and J. S. Garing. Optical properties of the atmosphere. *Environ. Res. Papers*, 411, AFCRL-72-0497, 1972.

Meesters, A. and M. R. van den Broeke. Response of the longwave radiation over melting snow and ice to atmospheric warming. *J. Glaciol.*, 43(143), 66-70, 1997.

Meier, M. F. Contribution of small glaciers to global sea level. *Science*, 226, 1418-1421, 1984.

Meyers, T. P. and R. F. Dale. Predicting Daily Insolation with Hourly Cloud Height and Coverage. *J. Clim. Appl. Meteor.*, 2, 343-348, 1983.

Morris, E. M. Turbulent transfer over snow and ice. *J. Hydrol.*, 105, 205-223, 1989.

Mote, T. L. and M. R. Anderson. Variations in snowpack melt on the Greenland ice sheet based on passive-microwave measurements. *J. Glaciol.*, 41(137), 51-60, 1995.

Munro, D. S. and J. A. Davies. On fitting the log-linear model to wind speed and temperature profiles over a melting glacier. *Boundary-Layer Meteorol.*, 15, 423-437, 1978.

Munro, D. S. Comparison of melt energy computations and ablatometer measurements on melting ice and snow. *Arctic and Alpine Res.*, 22(2), 153-162, 1990.

Nolin, A. W. and J. C. Stroeve. The changing albedo of the Greenland ice sheet: implications for climate change. *Ann. Glaciol.*, 25, 51-57, 1997.

Nye, J. F. A numerical method of inferring the budget history of a glacier from its advance and retreat. *J. Glaciol.,* 5(41), 589-607, 1965.

Oerlemans, J. Climate sensitivity of glaciers in southern Norway: application of an energy-balance model to Nigardsbreen, Hellstugubreeen and Alfotbreen. *J. Glaciol.*, 38(129), 223-232, 1992.

Oerlemans, J. Quantifying global warming from the retreat of glaciers. *Science*, 264, 243-245, 1994.

Oerlemans, J. Modelling the Response of Valley Glaciers to Climatic Change. In: *ERCA - Volume 2 - Physics and chemistry of the atmospheres of the Earth and other objects of the solar system*, edited by C. Boutron, pp. 91-123, Les Editions de Physique, Les Ulis, 1996.

Oerlemans, J. Climate sensitivity of Franz-Josef glacier, New Zealand, as revealed by numerical modelling. *Arctic and Alpine Research*, 29(2), 233-239, 1997.

Oerlemans, J. Glaciers and climate change. Bolkema, Lisse (The Netherlands), 2001.

Oerlemans, J. and J. P. F. Fortuin. Sensitivity of Glaciers and Small Ice Caps to Greenhouse Warming. *Science*, 258, 115-117, 1992.

Oerlemans, J. and W. H. Knap. A one-year record of short-wave radiation and albedo in the ablation zone of the Morteratschgletscher, Switzerland. *J. Glaciol.*, 44, 147, 231-238, 1998.

Oerlemans, J., H. Björnsson, M. Kuhn, F. Obleitner, F. Palsson, C. J. P. P. Smeets, H. F. Vugts, and J. de Wolde. Glacio-meteorological investigations on Vatnajökull, Iceland, summer 1996, an overview. *Boundary-Layer Meteorol.*, 92(1), 3-26, 1999.

Oerlemans, J. and B. K. Reichert. Relating glacier mass balance to meteorological data by using a seasonal sensitivity characteristic. *J. Glaciol.,* 46(152), 1-6, 2000.

Østrem, G. ERTS data in glaciology - an effort to monitor glacier mass balance from satellite imagery. *J. Glaciol.*, 15(73), 403-415, 1975.

Partington, K. C. Discrimination of glacier facies using multi-temporal SAR data. *J. Glaciol.*, 44(146), 42-53, 1998.

Paterson, W. S. B. The physics of glaciers. *Pergamon Press* (Elsevier Science), Oxford, 1994.

Pelto, M. S. Mass balance of south-east Alaska and nort-west Britisch Columbia glaciers from 1976 to 1984: methods and results. *Ann. Glac.*, 9, 189-194, 1987.

Ramage, J. M., B. L. Isacks and M. M. Miller. Radar glacier zones in southeast Alaska, U.S.A.: field and satellite observation. *J. Glaciol.*, 46(153), 287-296, 2000.

Rao, C. R. N. and J. Chen. Inter-satellite calibration linkages for the visible and near-infrared channels of the Advanced Very High Resolution Radiometer on the NOAA-7, -9, and -11 spacecraft. *Int. J. Remote Sensing*, 16(11), 1931-1942, 1995.

Rao, C. R. N. and J. Chen. Revised post-launch calibration of the visible and near-infrared channels of the Advanced Very High Resolution Radiometer (AVHRR) on the NOAA-14 spacecraft. *Int. J. Remote Sensing*, 20(18), 3485-3491, 1999.

Reeh, N. Parameterization of melt rate and surface temperature on the Greenland ice sheet. *Polarforschung*, 59(3), 113-128, 1991.

Raschke, E., P. Bauer and H. J. Lutz. Remote sensing of clouds and surface radiation budget over polar regions. *Int. J. Remote Sens.*, 13(1), 13-22, 1992.

Reijmer, C. H. The surface albedo of the Vatnajokull ice cap, Iceland, A comparison between satellite-derived and in situ measurements. *Internal report* V97-11, IMAU, Universiteit Utrecht, The Netherlands, 1997.

Reijmer, C. H., W. H. Knap and J. Oerlemans. The surface albedo of the Vatnajokull ice cap, Iceland: A comparison between satellite-derived and ground-based measurements. *Boundary-Layer Meteorol.*, 92(1), 125-144, 1999.

Rott, H. and C. Mätzler. Possibilities and limits of synthetic aperture radar for snow and glacier surveying. *Ann. Glaciol.*, 9, 195-199, 1987.

Rott, H. and G. Markl. Improved snow and glacier monitoring by the Landsat Thematic Mapper. *ESA Proceedings SP-1102*, 3-12, 1989.

Rott, H. and R. E. Davis. Multifrequency and polarimetric SAR observations on alpine glaciers. *Ann. Glaciol.*, 17, 98-104, 1993.

Rott, H., G. Domik, C. Mätzler, H. Miller and K. Lenhart. Study on the use and characteristics of SAR for land snow and ice applications. Mitteilung Nr. 1 (1985), Report to ESA, Contract 5441/83/D/IM(SC), Institut für Meteorologie und Geophysik, Universität Innsbruck, Austria, 1985.

Schmeits, M. J. and J. Oerlemans. Simulation of the historical variations in length of Unterer Grindelwaldgletscher, Switzerland. *J. Glaciol.,* 43(143), 152-164, 1997.

Sigurdsson, O. Glacier variations in Iceland 1930-1995. From the database of the Iceland Glaciological Society. *Jökull*, 45, 3-24, 1998.

Sigurdsson, O. Jöklabreytingar 1930-1960, 1960-1990 og 1995-1996. *Jökull*, 47, 101-107, 1999.

Sigurdsson, O. and T. Jónsson. Relation of glaciers variations to climate changes in Iceland. *Ann. Glaciol.,* 21, 263-270, 1995.

Slingo, A. and H. M. Schrecker. On the shortwave radiation properties of stratiform water clouds. *Quart. J. Roy. Meteorol. Soc.*, 108, 407-426, 1982.

Smeets, C. J. P. P., P. G. Duynkerke, and H. F. Vugts. Observed wind profiles and turbulence fluxes over an ice surface with changing surface roughness. *Boundary-Layer Meteorol.*, 92(1), 101-123, 1999.

Smith, L. C., R. R. Forster, B. L. Isacks and D. K. Hall. Seasonal climatic forcing of alpine glaciers revealed with orbital synthetic aperture radar. *J. Glaciol.*, 43(145), 480-488, 1997.

Smith, W. L. Note on the relationship between total precipitable water and surface dew point. *J. Appl. Meteor.*, 5, 726-727, 1966.

Smith, I. N. and W. F. Budd. The derivation of past climate change from observed changes of glaciers. In: Proc. of the symposium on sea level, ice and climatic change (Canberra, 1979), IAHS Publ. 131, 31-52, 1979.

Steffen, K., W. Abdalati and J. Stroeve. Climate sensitivity studies of the Greenland ice sheet using satellite AVHRR, SMMR, SMM/I and in situ data. *Meteorol. Atmos. Phys.*, 51, 239-258, 1993.

Stiles, W. and F. Ulaby. Dielectric properties of snow. *CRREL Special Report* 82-18, 91-103, 1982.

Stroeve, J., A. Nolin and K. Steffen. Comparison of AVHRR-derived and in situ surface albedo over the Greenland ice sheet. *Remote Sens. Environ.*, 62, 262-276, 1997.

Suttles, J. T., R. N. Green, P. Minnis, G. L. Smith, W. F. Staylor, B. A. Wielicki, I. J. Walker, D. F. Young, V. R. Tayler and L. L. Stowe. Angular Radiation models for earth-atmosphere system. *NASA reference publication*, 1184, 1988.

Tanre, D., D. N. Holben and Y. J. Kaufman. Atmospheric correction algorithm for NOAA-AVHRR products: theory and application. IEEE Trans. Geosci. *Remote Sens.*, 30, 231-250, 1992.

Thorarinsson, S. Oscillations of the Iceland glaciers in the last 250 years. *Geografiska Annaler*, 25(1-2), 1-54, 1943.

Van de Wal, R. S. W. and J. Oerlemans. An energy balance model for the Greenland ice sheet. *Global Plan. Change*, 9, 115-131, 1994.

Walraven, R. Calculating the position of the sun. *Solar energy*, 20, 393-397, 1978.

Warren, S. G. Optical properties of snow. *Rev. Geophys. and Space Phys.*, 20(2), 67-89, 1982.

Warrick, R. A., C. Le Provost, M. F. Meier, J. Oerlemans and P. L. Woodworth. Changes in sea level. In: Houghton, J. T., L. G. Meiro Filho, B. A. Callander, N. Harris, A. Kattenberg and K. Maskell, eds. *Climate change 1995: the science of climate change*. Cambridge, etc., Cambridge University Press., 1996.

Williams Jr., R. S. Satellite remote sensing of Vatnajokull, Iceland. *Ann. Glaciol.*, 9, 127-135, 1987.

Williams Jr., R. S., D. K. Hall, O. Sigurdsson and J. Y. L. Chien. Comparison of satellite-derived with ground-based measurements of the fluctuations of the margins of Vatnajökull, Iceland, 1973-92. *Ann. Glaciol.*, 24, 72-80, 1997.

Zwally, H. J. Microwave emissivity and accumulation rate of polar firn. *J. Glaciol.*, 18(79), 195-215, 1977.

# List of Publications

De Ruyter de Wildt, M.S., E.J. Klok and J. Oerlemans. Reconstruction of the mean specific mass balance of Vatnajökull (Iceland) with a Seasonal Sensitivity Characteristic. *Geografiska Annaler*, in press, 2002. **Chapter 3 of this thesis.**

De Ruyter de Wildt, M.S. and J. Oerlemans. Comparing satellite radar images with satellite albedo images and in situ mass balance observations: a case study of Vatnajökull (Iceland). *J. Glaciol.*, submitted, 2002. **Chapter 5 of this thesis.**

De Ruyter de Wildt, M.S., J. Oerlemans and H. Björnsson. A calibrated mass balance model for Vatnajökull, Iceland. *Jökull*, submitted, 2002a. **Chapter 2 of this thesis**.

De Ruyter de Wildt, M.S., J. Oerlemans and H. Björnsson. A method for monitoring glacier mass balance using satellite albedo measurements: application to Vatnajökull (Iceland). *J. Glaciol.*, in press, 2002b. **Chapter 4 of this thesis.**

Greuell, W. and M. S. de Ruyter de Wildt. Anisotropic reflection of melting glacier ice: measurements and parameterizations. *Remote Sens. Environ.*, 70, 265-277, 1999.

**Non-reviewed publications**

Kiefer, H., J. S. Kargel and many others. New eyes in the sky measure glaciers and ice sheets. *EOS*, *transactions*, *AGU*, 81(24), 260 and 270-271, 2000.

De Ruyter de Wildt, M.S. Methoden om de massabalans van gletsjers en ijskappen indirect te meten. *De Vakidioot*, 2001-2002(3), 9-13, 2002.

# Curriculum Vitae

Martijn Sybren de Ruyter de Wildt is geboren op 7 september 1971 in Leiderdorp als zoon van Hans de Ruyter de Wildt en Anja Edita den Blanken. Van 1983 tot 1989 was hij leerling aan het Chr. College Nassau-Veluwe te Harderwijk. Deze periode sloot hij af met het behalen van zijn VWO diploma. Vervolgens ging hij in Groningen farmacie studeren, om er na één jaar achter te komen dat dat zijn roeping niet was. Na de propaedeuse van deze studie behaald te hebben ging hij in 1991 naar Utrecht om geofysica te studeren. Hij slaagde voor het propaedeutisch examen van deze studie in 1993 waarna hij zich specialiseerde in de richtingen seismologie en exploratie-geofysica. Het doctoraal examen werd met goed gevolg afgelegd in 1996. In 1997 werkte hij voor een informatie-technologisch bedrijf in Delft en in 1998 begon hij, onder begeleiding van Hans Oerlemans, aan een promotieonderzoek aan het Instituut voor Marien en Atmosferisch onderzoek Utrecht. Uit dit onderzoek is het voor u liggende proefschrift voortgekomen.

Martijn Sybren de Ruyter de Wildt was born on September 7$^{th}$, 1971 in Leiderdorp as a son of Hans de Ruyter de Wildt and Anja Edita den Blanken. From 1983 till 1989 he attended secondary school in Harderwijk. Then he went to Groningen to study pharmacy, only to find out after a year that that was not his vocation. In 1991 he commenced with the study of geophysics at Utrecht University. He specialized in seismology and exploration-geophysics and graduated in 1996. In 1997 he worked for an information-technological company in Delft and in 1998 he began working on a phd.-research project under the supervision of Hans Oerlemans at the Institute for Marine and Atmospheric research Utrecht. This research project lead to the thesis in front of you.